A Spectral Approach to Noninvasive ICP Estimation: From Modeling to Clinical and Experimental Validation

by

Rohan Jaishankar

B.Tech., Electrical Engineering,
Indian Institute of Technology - Madras (2011)
S.M., Electrical Engineering and Computer Science,
Massachusetts Institute of Technology (2017)

Submitted to the Department of Electrical Engineering and Computer Science
in partial fulfillment of the requirements for the degree of

Doctor of Philosophy

at the

MASSACHUSETTS INSTITUTE OF TECHNOLOGY

June 2021

Author . . . .
Department of Electrical Engineering and Computer Science
May 19, 2021

Certified by . . . .
Thomas Heldt
Associate Professor of Electrical and Biomedical Engineering
Thesis Supervisor

Accepted by. . . . .
Leslie A. Kolodziejski
Professor of Electrical Engineering and Computer Science
Chair, Department Committee on Graduate Students

A Spectral Approach to Noninvasive ICP Estimation: From Modeling to Clinical and Experimental Validation

by

Rohan Jaishankar

Submitted to the Department of Electrical Engineering and Computer Science
on May 19, 2021, in partial fulfillment of the
requirements for the degree of
Doctor of Philosophy

Abstract

Intracranial pressure (ICP) is a cranial vital sign for monitoring patients with head injuries and to guide treatment decisions. Clinical ICP measurements are highly invasive and hence, ICP measurement is limited to critically ill patients. We present a spectral approach to model-based noninvasive ICP estimation, relying on a second-order circuit model of cerebrovascular physiology. We estimate ICP in the frequency domain, from arterial blood pressure and cerebral blood flow velocity waveforms. When validating our algorithm on two clinical patient cohorts of eight and a half hours, with measured ICP ranging from 1.3 mmHg to 24.8 mmHg, we achieved an accuracy and precision of 0.1 mmHg and 5.1 mmHg, respectively. Additionally, we designed an experimental porcine model to titrate the ICP in a predetermined manner over a wide range. This experimental model resulted in a rich dataset comprising 35 hours of data from eight pigs, with measured ICP ranging from 2.1 mmHg to 78.2 mmHg. We obtained an accuracy of 1.6 mmHg and a precision of 5.2 mmHg in estimating ICP on the porcine data. To evaluate our estimates' ability to correctly classify elevated ICP (defined as ICP>22 mmHg), we obtained an area under the receiver operating characteristic curve of 0.94. Additionally, the algorithm achieved a sensitivity of 0.88 and a specificity of 0.87 in this binary classification task at a noninvasive ICP threshold of 22 mmHg. Clinically, missing an episode of elevated ICP or under-treatment can have potentially fatal consequences, and we demonstrated that with appropriate margins on the classification thresholds, the probabilities of these events are less than 1%, using our noninvasive ICP estimates. Finally, we obtained a correlation coefficient of 0.89 between our estimates and the measured ICP, indicating a high degree of capturing underlying variations in measured ICP. Our algorithm's performance is well within the clinically acceptable range and comparable or superior to past attempts at estimating ICP noninvasively reported in literature. We believe that the work presented here takes a significant step towards realizing the clinical dream of implementing a real-time, noninvasive ICP measurement modality in a calibration-free and patient-specific manner at the bedside.

Thesis Supervisor: Thomas Heldt
Title: Associate Professor of Electrical and Biomedical Engineering

Acknowledgments

It is my immense pleasure to acknowledge the efforts of everyone who contributed to this thesis, as this thesis truly would not have been possible without the inputs, personal and professional, from several people in my life. First and foremost, I thank my thesis advisor, Professor Thomas Heldt. My PhD has been a long and winding six year journey and I am very grateful I found an amazing advisor in Thomas to pursue my research with. Thomas' work ethic, knowledge of physiology and biomedical signal processing, and passion for solving the open problems in healthcare have been a constant source of inspiration for me throughout my PhD. I am eternally grateful for the countless hours he spent steering me along the right path, teaching me valuable skills (and courses), and imparting advice selflessly. Thomas has also been a mentor and advisor to me in all matters of life for the past six years. He has helped me improve my communication and presentation skills, taught me the importance of asking the right questions without any fear and to constantly strive for perfection. He has also patiently stood by my side and been a great friend to help me overcome any adversities. Moreover, it has been very fulfilling to be a small part of Thomas being awarded a richly deserved tenured faculty position at MIT EECS. Thank you again, Thomas, for everything you have done for me and I look forward to seeing how all the exciting research you are supervising progresses.

Dr. James Holsapple is one of the most brilliant people I have ever had the pleasure of interacting with. Jim has been involved in all my clinical work at Boston Medical Center and was involved in all the animal experiments I conducted. None of the clinical data collection or the animal experiments would have been possible without Jim's involvement. Something that has always amazed me about Jim is his incomparable passion and enthusiasm to help with my work and investigate further to improve the quality of research. I have no idea how he has been able to find time for any of his research commitments, given his packed schedule as the Chair of Neurosurgery at Boston Medical Center, and since most of our animal experiments lasted for over 13 hours! Thank you very much, Jim, for always being available to answer my endless stream of questions, for your dedication to our work, for agreeing to be an integral member of my thesis committee, and for always inspiring me to work harder and aim higher. I hope to continue collaborating with you and seeking out your advice in the future.

I would like to thank Professor Roger Mark for being the chair of my thesis committee and for being an endless source of wisdom and advice. It is not an exaggeration to say that Roger's knowledge of physiology is second to none and I have greatly benefited from this in my research. But Roger's greatest influence on me has been through the course 6.022 - Quantitative Systems Physiology. Taking this course as a student and then serving as a teaching assistant for it have significantly contributed to my passion for biomedical engineering and helped me finalize my future career path. Teaching 6.022 with Roger for three years has been one of the fondest and unforgettable experiences of my MIT life. I will never forget the many hours I spent in Roger's office listening to his fascinating life stories and experiences, while procrastinating the grading process. Thank you, Roger, for all your invaluable life and professional advice, and for being the best teacher I have had in my life.

I would also like to thank Dr. Alison Hayward for her integral role in all the animal experiments. Alison was one of the driving forces responsible for the animal experimental model that forms a major part of this thesis. She taught me the value of planning ahead and the challenges involved with complex surgical procedures. I am very grateful to her for her role as a veterinary surgeon, for her constant feedback, and for her patience with the extremely long hours of each experiment.

I am indebted to all the members, past and present, on the ICP research project. Professor George Verghese has been a source of encouragement throughout my work and his feedback has helped mold the project to be successful. His initial work with Dr. Faisal Kashif and James Noraky helped motivate a large part of my work. Ever since I joined Thomas' group, Dr. Andrea Fanelli has been an amazing mentor, leader and friend. Andrea was single-handedly running the ICP project when I joined, and he patiently helped bring me up to speed. He provided honest feedback and helped with the algorithm development, preprocessing, and most importantly, with the data collection at Boston Children's Hospital and Boston Medical Center. Syed Imaduddin is one of the hardest-working, dedicated, and brilliant graduate students I have met at MIT. He has helped me at numerous junctures with his insightful suggestions and he has listened to me complain about my often trivial issues patiently. I look forward to him completing his PhD shortly and going on to be successful in life. Dr. Daniel Teichmann was in our lab for a short time but played a pivotal role in helping develop the porcine model and organizing every experiment. I hope he has a successful career in Denmark.

All the work described in this thesis needed the support and assistance of several people along the way. The clinical data collection would not have been possible without the endless support of Dr. Aristotelis Filippidis, Dr. Thai Vu, Richard Carozza at Boston Medical Center, and Dr. Robert Tasker, Dr. Kerri LaRovere, Dr. Frederick Vonberg, and Dr. Brian Walsh at Boston Children's Hospital. All the data collectionwas supported constantly by a team of brilliant researchers at Philips Research North America including Dr. Raju Balasunder, Dr. Jonathan Sutton, Dr. Jon Fincke, and Dr. Joseph Frassica. I would also like to thank Morgan Jamiel, Dr. Robert Marini and Dr. Jennifer Haupt from the Division of Comparative Medicine at MIT, for all their assistance with the animal experiments.

I was very lucky to be part of a fantastic group of people in Thomas' lab – the Integrative Neuromonitoring and Critical Care Informatics (INCCI) lab. Some of my best experiences at MIT have been spending time with my INCCI lab-mates. They have been extremely supportive and helped make the lab environment extremely fun and welcoming. Outside the lab, we indulged in a number of activities including annual soccer games at Killian Court or Kresge, pot-lucks, delicious dessert nights organized by Andrea, annual barbecues, Halloween parties, countless visits to Meadhall and Cambridge Brewing Company, a cruise as part of a conference organized by Thomas, and so on. I have unforgettable memories from each of these activities and am thankful to everyone involved – James, Andrea, Varesh, Jonathan, Imad, Jeff, Tiffany, Freddie, Daniel, Elena, Rajib, Nalini, Jono, and Minoru. I am also thankful to Caitlin and Allison for being the glue that held our lab together with their tireless effort.

A PhD is not always smooth sailing, and I was fortunate to be surrounded by a great group of friends, who were there to share the many highs of PhD life with me, and also help me through the lows of the last six years. I cannot put into words how grateful I am to Dheeraj Nagaraj, Karthik Murugadoss, James Lynch, and Ranjan Anantharaman for being my closest allies and friends. Karthik has put up with me at all times, from being my roommate in the first couple of years to remaining a close friend who has always helped me and got my back. Dheeraj, with his infinite wisdom and endless sarcastic quips, has played an immense role in supporting me, helping me grow, and being an amazing friend, all while being a selfless and brilliant researcher. James has been a great lab-mate and friend throughout my time at MIT, and we have visited what feels like every restaurant in Boston/Cambridge during these last six years. Ranjan has been a constant source of support in the last couple of years with many conversations devoted to our common interests in sports and video games (one of my greatest achievements is getting him interested in the NFL!). I am very thankful to Prashanth Prakash and Darsh Shah, part of the "Tang Boys" with Dheeraj and Ranjan, for keeping me sane during this last crazy pandemic-ridden year with our frequent meetups, endless discussions on any and every topic, cooking and baking sessions, and trips to Honest. Prahlad Krishna and Varun Suresh have been my close friends since my high school days and I am grateful for their continued support. There have been several other friends who have played a pivotal role in my journey at MIT, including Srinivasan Raghuraman, Suhas Kowshik (thanks for the amazing cross-country road trip), Prateesh Goyal, Arundhati Ramesh, Shreya Girish, Nishita Parnandi, Krishna Shrinivas, Shloka Narayanan, Visweswaran Ravikumar, Anjali Ramesh, Sooraj Narayan, Nikhilesh Ghanta, Sharan Raja, Anup Atre, just to name a few. I would be remiss not to mention my fantastic experiences as part of the MIT Sangam board. Organizing events as part of Sangam was an amazing experience, especially organizing the grand Diwali night, and helped me meet several Indian students on campus, while also not letting any of us feel disconnected from our culture.

Most importantly, I would like to thank my family. My parents have been my rock since my childhood and have supported me in every endeavor. I would not have gotten anywhere near my PhD if not for their sacrifices, advice, blessings, and unconditional love. I am grateful to my uncle and aunt, Prakash and Vaishali, for never letting me feel homesick, for always begin there for me, and for serving as second parents to me here in USA. My cousins here in USA, Vedant and Ragini, and my cousins back home, Vignesh and Nandini, have supported me throughout and it has been exciting to watch them grow and succeed. My uncle and aunt, Sreenath and Jyothi, have been by my side throughout my childhood and have always looked out for me, even though I have been thousands of miles away. Finally, I would like to thank my grandparents – Nana and Nani for their unconditional love and for being the primary inspiration for me to pursue scientific research, and Ammamma and Thatha for your love, support and blessings (I miss you dearly).

This work was made possible through support of a Grass Instruments Graduate Fellowship from the Department of Electrical Engineering & Computer Science, MIT, and funding from Philips Healthcare to MIT's Medical Electronic Device Realization Center and the Psychological Health and Traumatic Brain Injury, through the Combat Casualty Care Research Program under Award No. W81XWH-18-1-0332.

Contents

List of Figures

List of Tables

Chapter 1

Introduction

Neurological injuries and disorders of the brain are responsible for a significant fraction of the worldwide hospitalizations annually [14, 15]. Traumatic brain injuries (TBI) are primarily caused by contact injuries, and account for almost 2 million hospitalizations annually [16, 17]. Hemorrhagic strokes result in accumulation of blood in an intracranial space and shifting of cerebral structures, and need to be managed expeditiously [18, 19]. Hydrocephalus is another neurological condition, common in children and patients recovering from previous neurological damage. It results in accumulation of fluid in the region surrounding the brain. Brain tumors, cerebral malaria, tuberculous meningitis are all responsible for further increasing the clinical neurological burden worldwide [20, 21].

Most of these neurological conditions can be acutely life threatening in nature and require immediate pharmacological or surgical intervention, and continuous monitoring of the patient to ensure favourable outcomes. Moreover, these disorders are also usually characterized by an increase in the compartmental pressure within the skull, referred to as the intracranial pressure (ICP). Hence, the diagnosis, treatment, and monitoring of patients with such conditions heavily rely on accurate measurement of this cranial vital sign, ICP. ICP is defined as the hydrostatic pressure of the cerebrospinal fluid (CSF) that bathes the brain tissue, and normally ranges from 5 mmHg to 15 mmHg in healthy, supine adults.

While ICP is routinely monitored in neuro-ICUs and neurocritical care units around the world, the clinically accepted modalities for measuring ICP are highly invasive. These approaches require drilling a hole in the skull and inserting a catheter or transducer into the intracranial space, thus leading to a risk of cerebral damage, infections and inducing new hemorrhages. Due to its invasive nature and need for neurosurgical expertise, ICP measurement is limited to a small subset of critically ill patients, thus potentially depriving a larger patient pool who could benefit from this cranial vital sign. Hence, significant research efforts worldwide have been dedicated to the development of an accurate and robust noninvasive ICP measurement scheme, that could replace or complement the existing invasive methods. While several attempts have been made to solve this clinically important problem, achieving accurate, continuous noninvasive ICP estimates in a calibration-free and patient-specific manner has remained elusive. While several data-driven approaches have been attempted in the past, the use of model-based approach is extremely attractive due to its tractable nature and the physiological basis of the model parameters. In this thesis, we aim to build upon some of these past attempts [6, 7] to develop and implement a spectral model-based approach to noninvasive ICP estimation, and validate our results on two clinical patient cohorts and in an experimental porcine model, all independently recorded by us.

1.1 Specific Aims

Motivated by past attempts at model-based attempts and their limitations, we propose the following specific aims for our estimation framework:

1. Develop a model-based, calibration-free, patient-specific approach to noninvasive ICP estimation by implementing a spectral algorithm on a simple, tractable, lumped-parameter circuit model of the cerebrovascular physiology.
2. Design and deploy a custom data acquisition system for archiving high-resolution physiological waveforms from multiple devices and important ancillary-data from the bedside, on a common time axis
3. Design a reproducible experimental porcine model for altering the cerebrospinal state of the animal over a wide range of ICP values, in a predetermined manner, and to observe the physiological and hemodynamic response of the animal

4. Validate the accuracy and robustness of our spectral noninvasive ICP estimation algorithm in a comprehensive manner on clinical data recorded from neurologically injured patients at local hospitals, and on the rich porcine model cohort, while quantifying the estimation performance at varying levels of clinical accuracy

1.2 Thesis Structure

In Chapter 2, we review the relevant cerebrovascular and CSF physiology, to understand the clinical significance of ICP as a key cranial vital sign. We then review the currently accepted clinical standards for ICP measurement, and discuss the inherent risks associated with their invasiveness. Thus, we motivate the pressing need for a noninvasive ICP measurement modality, and review past attempts at solving this problem, while focusing on two model-based approaches that motivated our work.

In Chapter 3, we detail our proposed model-based spectral algorithm of noninvasive ICP estimation. We describe our model of craniospinal physiology, capturing the interplay between blood flow through a major cerebrovascular territory and ICP. We then detail the steps involved in our spectral algorithm to estimate ICP noninvasively in a patient-specific manner. This chapter was published in [22].

In Chapter 4, we describe the motivation, design and deployment of a custom data acquisition system at Boston Medical Center, for archiving multiple high-resolution physiological data streams on a common time axis. We describe the data acquisition protocol at the bedside, along with the multiple data streams and meta-data recorded. We then detail the clinical datasets recorded from two independent patient cohorts, that served as validation datasets for our spectral algorithm. Finally, we present the estimation performance of our algorithm on these patient datasets, and briefly discuss the clinical significance of these results.

In Chapter 5, we describe the inherent limitations of using patient data for neurological validation studies, and motivate the development of a novel large animal model to overcome these challenges. We then describe the choice of a porcine model and the extensive preparatory work undertaken to understand and overcome some of the anatomical challenges posed by a porcine model. Finally, we describe the experimental protocol for altering the ICP in a predetermined manner, over a wide range of cerebrospinal states, and monitoring the physiological response of the animal.

In Chapter 6, we present the experimental census and statistics obtained from the porcine model, and demonstrate its success in overcoming the challenges posed by human neurological data. We then describe the framework of quantifying our algorithm's estimation performance in a comprehensive manner on this rich dataset, at varying degrees of clinical accuracy. Finally, we present the estimation results at these different levels of accuracy and prove the robustness of the algorithm's performance.

In Chapter 7, we analyze the algorithm's estimation performance on the porcine model dataset, by comparing the results to those of the currently accepted invasive ICP probes, as reported in literature. We also compare our algorithm's performance to past attempts at noninvasive ICP estimation and to our estimation performance on the patient cohorts, to assess the robustness of our approach. We then discuss some of the limitations and sources of error identified in our current work, and suggest potential avenues to further improve on these results. Finally, we summarize our contributions, and detail the future work left to be undertaken, both short-term and long-term, to gain a better understanding of the cerebrovascular dynamics and to clinically realize the goal of taking these model-based noninvasive ICP measurement modalities to the bedside.

Chapter 2

Background

ICP is defined as the hydrostatic pressure of CSF that bathes the brain tissue, and typically ranges from 5 mmHg to 15 mmHg. ICP is a cranial vital sign for diagnosing, monitoring, and guiding treatment decisions in patients with a variety of neurological injuries, some of which were described in the previous chapter. In this chapter, we begin by reviewing the cerebrovascular physiology and the dynamics of CSF circulation, to formalize the definition of ICP. We then explore the reason why ICP is an important neurological indicator, and how ICP is routinely monitored in patients by invasive means. We discuss the risks and limitations of the clinically accepted invasive ICP measurement modalities, thus motivating the pressing need for an accurate noninvasive ICP measurement modality. Finally, we briefly review the diverse attempts at noninvasive ICP estimation in literature, and focus on the two model-based approaches by Kashif *et al.* [6] and Noraky *et al.* [7]) that serve as the foundation for our spectral model-based approach at noninvasive ICP estimation.

2.1 Physiological Background of ICP

2.1.1 Cerebrovascular physiology

The brain is a soft tissue located within the rigid cranium or skull, and surrounded by meningeal layers. The brain is bathed by CSF, which provides mechanical support, buoyancy and a suitable chemical environment for the brain tissue [23, 24]. CSF is produced by a specialized capillary network , the choroid plexus, mostly in the CSF-filled lateral ventricles of the brain by passive and active filtration of the blood plasma. From the lateral ventricles, CSF flows through the foramen of Monro into the third ventricle, before reaching the fourth ventricle through the cerebral aqueduct. Finally, the CSF empties into the subarachnoid space through the foramina of Magendie and Luschka, where it circulates before getting reabsorbed into the venous system through projections, called arachnoid villi. At steady-state, the volume of CSF circulating in the body is maintained constant by balancing the rates of formation and reabsorption. Moreover, the composition of CSF is kept independent of the blood by regulation of the blood-brain and blood-CSF barriers. The ventricular system and pathway of CSF flow is shown in Figure 2-1.

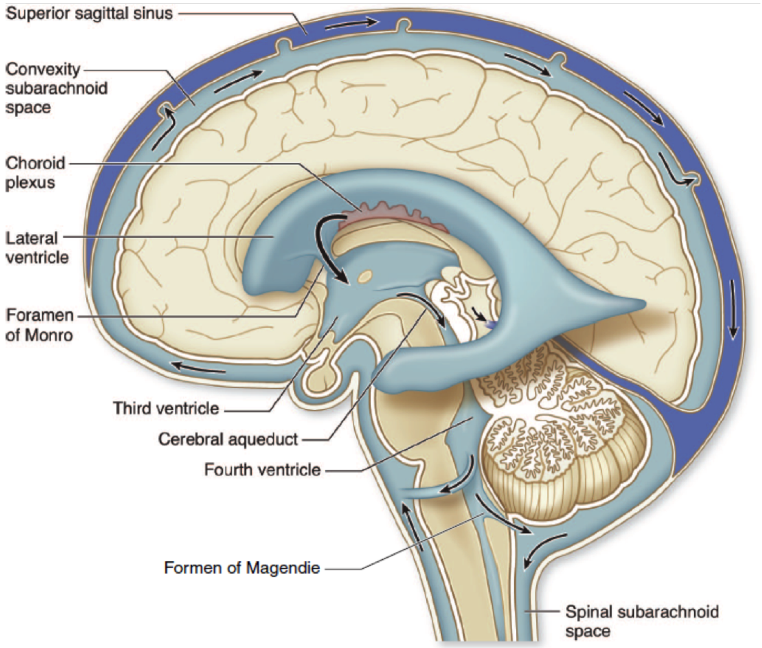

Figure 2-1: Sagittal slice of the brain depicting the ventricular system and pathway of CSF flow from formation at the choroid plexus to reabsorption by the arachnoid villi. Image adapted from [1].

The metabolic demands of the brain are met by a dense network of arteries, veins and capillaries. A pair of internal carotid arteries, arising from the common carotid arteries are responsible for a major portion of the oxygenated blood supplied to the brain tissue. The rest of the oxygenated blood is supplied by a pair of vertebral arteries. Upon entering the skull through the foramen magnum, these arteries anastomose at the base of the brain to

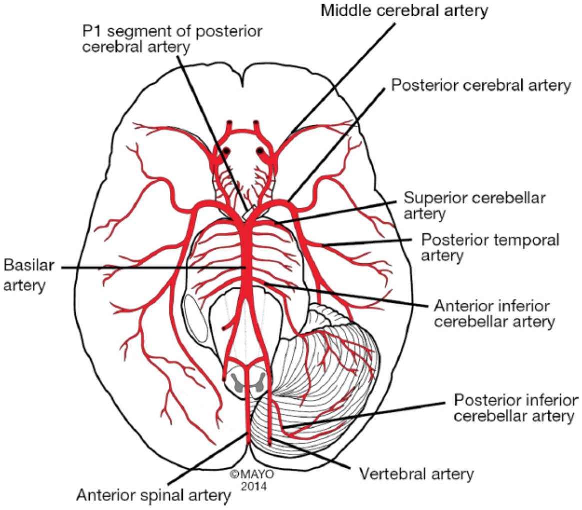

Figure 2-2: Illustration of the cerebrovascular arterial network including the Circle of Willis at the base of the brain. Image adapted from [2].

form a vascular ring-like structure, called the Circle of Willis. Three main pairs of arteries arise from the Circle of Willis, each supplying blood to a different region of the brain. These arteries are the Middle Cerebral Arteries (MCAs), Anterior Cerebral Arteries (ACAs), and the Posterior Cerebral Arteries (PCAs). The arterial network of the brain is depicted in Figure 2-2. These arteries branch into an extensive network of capillaries to perfuse all of brain tissue and facilitate uptake of oxygen and excretion of carbon dioxide and metabolic waste. The de-oxygenated blood drains into several venous sinuses, most notable of which is the superior sagittal sinus, before they empty into the systemic jugular veins.

2.1.2 Significance of ICP

The rigid skull and relatively inelastic dura mater surrounding the brain tissue results in a fairly constant volume of the intracranial space. Typically, the intracranial compartment is composed of three main components – brain tissue or parenchyma (80%), CSF (10%) and blood (10%). While the dura mater is relatively inelastic in the cranial space, the dura covering the spinal canal can accommodate small increases in fluid volume. Hence, small shifts in the intracranial volume are compensated by venous outflow into the jugular veins and by shunting small amounts of CSF into the dural sac surrounding the spinal canal. It is important to note here that these compensatory capacities are highly limited (on the order of 30 cc), while the circulating CSF volume in an adult is usually around 150 cc [4, 25, 26]. Once these limited compensatory capacities are exhausted, any further uncompensated shift or expansion in intracranial volume leads to an increase in the compartment pressure. This manifests as an elevation in the ICP, defined as the hydrostatic pressure of the CSF. The resulting pressure-volume relationship in the intracranial space is non-linear with two regimes - compensated and decompensated [27]. Langfitt *et al.* [3] demonstrated this by placing an intraventricular balloon in monkeys and progressively inflating it, thus simulating a space-filling lesion in the intracranial space. At smaller balloon volumes, the intracranial system was found to be well-buffered by the aforementioned mechanisms, meaning that ICP did not increase appreciably. However, once these compensatory reserves were exhausted, the system entered a highly non-linear unbuffered or decompensated regime, where a slight increase in the intracranial volume led to a drastic elevation in ICP, as shown in Figure 2-3. This nonlinear pressure-volume relationship, based on the relatively fixed volume composition of the intracranial space is referred to as the Montro-Kellie doctrine [28–30].

Perfusion to the brain tissue is maintained by regulating the volumetric cerebral blood flow (CBF) in the vasculature. The primary driving force for CBF through the blood vessels is the cerebral perfusion pressure (CPP), defined as the difference of the arterial blood pressure (ABP) and the ICP [31, 32]. Under normal conditions, the CBF is maintained constant over a wide range of CPP values by various complex control mechanisms, referred to as cerebrovascular autoregulatory mechanisms. These mechanisms affect the vascular tone by responding to changes in transmural pressure or blood gas concentrations, resulting in constant CBF. As CPP decreases, the vascular smooth muscle dilates to increase flow back to baseline and vice versa for an increase in CPP. However, these autoregulatory mechanisms have limited thresholds of CPP over which they function. Beyond these CPP thresholds, the vascular tone cannot be altered further, resulting in an approximately linear relationship between the CPP and CBF. This results in a Lassen curve of cerebrovascular autoregulation, shown in Figure 2-4.

Elevated ICP, known as intracranial hypertension, is associated with poor outcome in

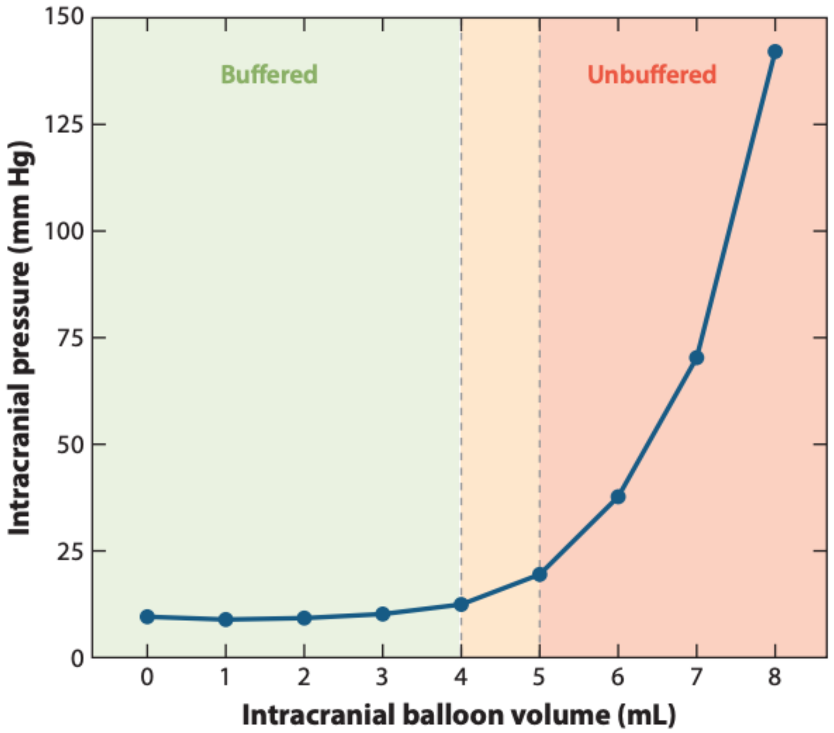

Figure 2-3: Illustration of Monro-Kellie doctrine depicting the nonlinear pressure-volume realtionship in the intracranial space, based on experiments conducted by Langfitt *et al.* [3]. Image adapted from [4]

.

brain-injured patients [33, 34]. Substantial elevation in ICP, leads to a decrease in CPP below the lower threshold of cerebrovascular autoregulation and hence leads to lower CBF, poor perfusion and cerebral ischemia [27, 31]. Extreme elevations in ICP can lead to herniation of cerebral structures and potentially fatal outcomes [34]. These elevations in ICP are caused by shifts in the volume of the intracranial compartments, and if not treated carefully, could lead to the patient entering the unbuffered regime shown in Figure 2-3. Once in this regime, ICP elevations are very dangerous owing to the steep pressure-volume relationship, and thus the ICP needs to carefully monitored. Hence, ICP is an important cranial vital sign that needs to be carefully monitored and titrated to remain within the normal range in patients with neurological injuries, to ensure they do not transition into the decompensated regime, and to prevent significant elevations in ICP and poor clinical outcomes.

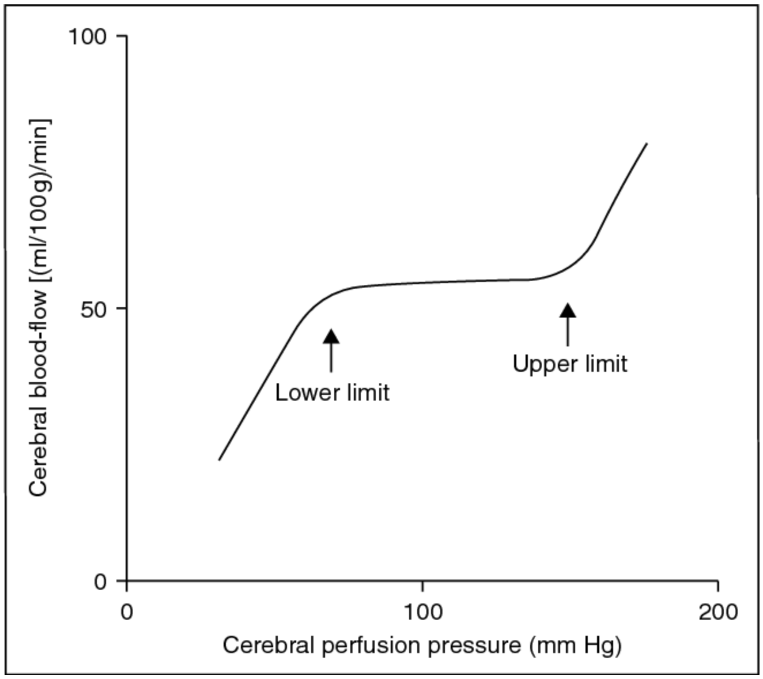

Figure 2-4: Representative image of the Lassen curve for cerebrovascular autoregulation. The volumetric CBF is maintained constant over a wide range of CPP values, which drives the blood flow through the vasculature.

2.2 Current ICP Measurement Modalities

ICP is an important clinical indicator of neurological injury and is routinely monitored in neurologically compromised patients, owing to the reasons outlined in the previous section. The currently accepted gold-standards for clinical ICP measurement are highly invasive, involving the drilling of a burr hole in the skull and carefully threading a catheter or pressure transducer into one of the lateral ventricles or into the brain tissue (also called the parenchyma) [31,35,36]. The former intraventricular approach is often implemented as an external ventricular drainage (EVD) system to allow for measurement of ICP, while also providing the option of draining out CSF to relieve episodes of elevated ICP. These EVD systems are referenced at the level of the tragus, and are often re-calibrated to ensure accurate readings over longer periods of time. The other gold-standard approach commonly used for ICP monitoring involves the placement of a solid-state pressure transducer into the brain parenchyma, and is hence referred to as an intraparenchymal ICP probe. While both the intraparenchymal and EVD ICP measurements record the ICP waveform, clinical

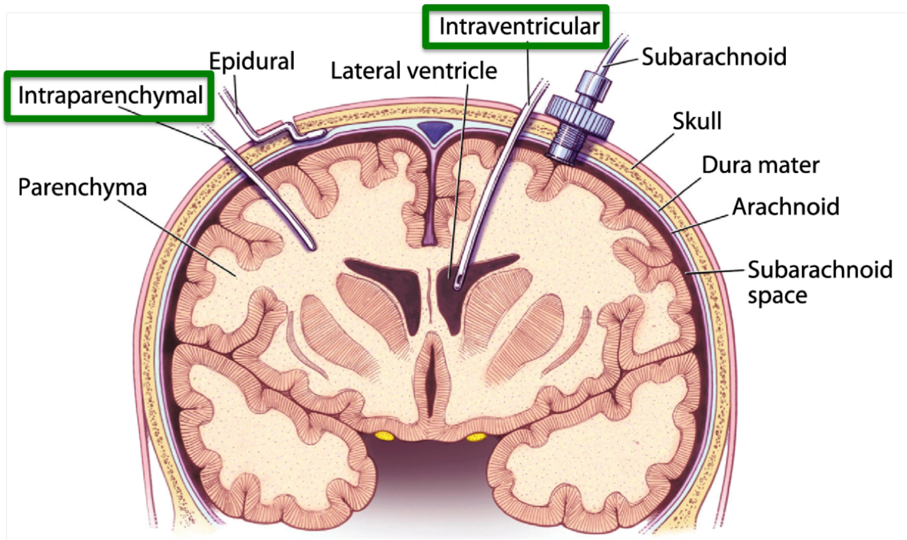

Figure 2-5: Image depicting the various invasive ICP measurement modalities. The two clinically accepted gold-standards are the intraventricular (EVD) and intraparenchymal probes, marked in green. Image adapted from [5].

decisions are primarily based on the the mean ICP, with the intra-beat dynamics largely ignored for clinical purposes. The intraparenchymal ICP measurements are less invasive than the EVDs, and are very useful when CSF drainage is not required or if EVD placement is not recommended due to complications arising from cerebral edema and TBIs. The intraparenchymal ICP probes cannot be re-calibrated once implanted and hence carry the risk of drift in the measured ICP values. While EVDs and intraparenchymal ICP probes are the clinical gold-standards, ICP can also be measured by placing pressure transducer in one of several other intracranial spaces. However, these devices have largely been restricted to research purposes as they can be inaccurate and suffer from significant drift [37–39]. A schematic of the different possible ICP measurement modalities is shown in Figure 2-5.

2.2.1 Limitations of invasive ICP measurement

While the EVDs and intraparenchymal modalities are commonly used in neurocritical care, they are highly invasive and require neurosurgical expertise to precisely place the device in the correct intracranial location. The invasiveness also renders these modalities unsuitable for long-term monitoring of ICP and severely limits the patient population that could potentially benefit from this vital sign. These invasive approaches also carry several additional risks of further damaging the brain tissue or inducing intracerebral hemorrhages that exacerbate the patient's neurological injury. Kakarla *et al.* reported that out of 346 EVD placements, around 23% were sub-optimally placed, and required re-positioning or removal and re-attempting the EVD placement [40]. Each of these attempts is associated with a risk of damaging the parenchyma [41] and causing a hemorrhage, with neurosurgeons often attempting two or more times to accurately place the EVD in the correct location. Ortolano *et al.* reported around 20% of EVD placements resulted in a small hemorrhage or ischemic region [42]. Additionally, since these modalities require the drilling of a hole in the skull, they carry a risk of infection by exposing the brain to harmful pathogens. Champey *et al.* conducted a multi-center study in Europe and observed EVD-induced infection rates as high as 7.2 % and 9.2% in two of the centers [43]. Another multi-center study by Jamjoom *et al.* rreported EVD-induced infection rates of 9.3% among 452 patients [44]. Such infections are extremely dangerous and much higher than the reported infection rates of 0.7% and 0.9% for placement of the commonly used venous and peripheral arterial catheters. There are several other papers reporting the substantial risks of cerebral damage and EVD-induced infections [41, 45–48]

The invasive ICP measurement approaches can also have inconsistencies in the reported ICP values. Lescot *et al.* measured ICP using the Pressio intraparenchymal and the Codman intraparenchymal devices, and independently compared the measurements from each of these to the ICP measured simultaneously by an EVD [49]. They reported a bias of −0.6 mmHg and 0.33 mmHg with 95% limits of agreement of (−8.1 mmHg, 6.9 mmHg) and (−6.7 mmHg, 7.1 mmHg) across 30 patients, for the Pressio and Codman intraparenchymal devices, respectively. Brean *et al.* reported an accuracy of 0.7 mmHg and a precision of 6.8 mmHg in over 218,000 simultaneous comparisons of ICP measured by an EVD and intraparenchymal device [50]. While some of these discrepancies could be explained by naturally occurring pressure gradients in the intracranial space [51], the residual errors between the invasive ICP probes provide a reference against which to compare the accuracy and precision error metrics of the noninvasive approaches.

2.2.2 Potential benefits of noninvasive ICP monitoring

Since the clinically accepted ICP measurement modalities carry the risks previously described of further cerebral damage and introducing cranial infections, ICP monitoring is only indicated in a small subset of critically ill patients. However, the patient population that could benefit from ICP monitoring is vast and hence there is a pressing need to develop a robust and accurate noninvasive ICP measurement modality. A noninvasive ICP modality would allow for screening of patients with mild symptoms, where drilling a burr hole is not warranted, but where the symptoms could be indicative of underlying neurological damage. Additionally, it would allow for early screening of patients at the site of injury, at home or en route to the hospital, enabling early triage without the need for neurosurgical expertise. This is crucial since neurological injuries and intracranial hypertension are often acute and can be life-threatening in nature, with the the probability of favorable outcomes increasing significantly with early detection [13, 34]. Another challenge with invasive ICP measurement is that of patients with altered mental states. Identifying patients who require an invasive ICP probe usually requires knowledge of the source of injury or interrogating the patient, which is not feasible in patients with altered mental states or in inebriated states. A concrete example is an inebriated patient arriving at a hospital's Emergency Department with a traumatic brain injury. Even though acute intracranial bleeds can be ruled out with an initial head Computed Tomography (CT) scan, slowly developing bleeds can alter the mental state of the patient. Hence, it is difficult to assess whether the altered mental state is due to the source of the original inebriation or a developing intracranial hypertension, which needs to be managed expeditiously. These cases would be greatly benefited by a noninvasive ICP measurement, in order to guide treatment decisions. Finally, noninvasive ICP measurements could guide future research into the pathophysiology underlying other disorders such as unexplained headaches and migraines [52, 53], as well as shed light on poorly understood and hotly debated conditions, such as craniosynostosis, for example [54]. These measurement modalities could also enable wider studies to better understand the dynamics of cerebrovascular autoregulation. Hence, there is an immediate need for the development of an accurate noninvasive ICP measurement modality to benefit a larger patient population, improve clinical outcomes by early diagnoses, and overcome the substantial risks of the clinically accepted invasive modalities.

2.3 Noninvasive ICP Estimation

The development of a noninvasive ICP measurement modality has been an active area of research for decades and several approaches have been proposed in the clinical and engineering literature. Some of these approaches involve supplying a physical input to the brain in a variety of ways, and recording the response. Ragauskas *et al.* proposed a novel method of applying an external pressure on the eyeball to balance the retro-orbital pressure with the ICP [55]. Similarly, ultrasonic approaches of detecting optic nerve distension have been proposed, motivated by previously reported correlations between elevations in ICP and increase in optic nerve sheath diameter [56–58]. Levinsky *et al.* proposed an approach of estimating ICP by using transcranial acoustic signals [59]. Other approaches involve measuring the deformation of the skull precisely and calibrating to estimate ICP changes [60]. These approaches have been validated on patient cohorts over limited ranges of measured ICP and importantly, require calibration for each patient. Moreover, these approaches might not be widely usable as additional stimulation of neurologically injured patients is not recommended.

Most of the current research focuses on leveraging the intrinsic relationship between the ABP, CBF and ICP to estimate the ICP noninvasively in a data-driven or model-based manner [4, 35, 36, 48, 61, 62]. Since volumetric CBF is not routinely measured, most of these approaches adopt a measurable, linearly scaled parameter, the cerebral blood flow velocity (CBFV). Some of these approaches correlate indices computed from the ABP and CBFV waveforms with the ICP, using metrics such as pulsatility index (PI), resistivity index (RI) and pressure reactivity index (PRx) [63]. Several other reports utilize data-mining and machine learning approaches to estimate the absolute ICP or predict variations in ICP, based on features extracted from ABP, CBFV and potentially other vital signs [64–69]. These algorithms are trained on a subset of clinically recorded patient data or simulated data, and the parameter values are generalized to estimate ICP on a wider validation dataset. These approaches can estimate ICP continuously over long periods, but do not give any pertinent information on the underlying physiology or sources of performance error, due to their physiology-independent black-box approach. The model-based approaches rely on representing the cerebrovascular hemodynamics using models of varying complexities, and developing algorithms to estimate the ICP in a physiologically tractable manner – meaning the models are grounded in cerebrovascular physiology with each parameter potentially representing a meaningful physiological analogue. These approaches have an inherent trade-off between the higher complexity of models and the independence of parameter estimation. The higher order models capture complex cerebrovascular dynamics more efficiently, but require the specification of several model parameters rendering it impossible to estimate ICP in a simple and calibration-free manner [6, 7, 9, 22, 70–78]. Here we focus on two such model-based approaches, both relying on simple lumped-parameter models of cerebrovascular physiology, developed by Kashif *et al.* [6] and Noraky *et al.* [7].

2.3.1 Model-based noninvasive ICP estimation

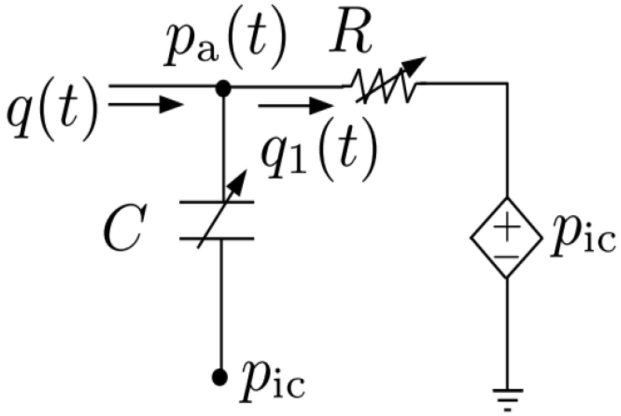

Figure 2-6: First-order circuit model of cerebral vasculature, as proposed by Kashif *et al.* [6].

Figure 2-6 depicts a first-order circuit model of the a major cerebrovascular territory proposed by Kashif *et al.* [6], and also further explored by Fanelli [9, 79] and Imaduddin [78]. This model is inspired by the canonical Windkessel model of peripheral circulation, routinely used in cardiovascular literature. In the Kashif model, R represents the viscous resistance to blood flow through the vasculature, while C models the lumped compliance of the arterial walls and brain tissue. Hence, the transmural pressure across the lumped compliance is the difference of the ABP at the inlet of the artery, $p_a(t)$, and the external ICP, $p_{ic}(t)$. The flow of blood through the resistance, R, is also driven by the pressure gradient between the upstream ABP and effective downstream ICP, due to the Starling resistor effect (further explained in the next chapter). Since volumetric CBF is not easily measurable, Kashif exploited the linear invariance of the model to replace CBF by the CBFV, $q(t)$, in the model. Kashif implemented a time-domain algorithm to estimate the ICP on a window-by-window basis from simultaneously recorded ABP and CBFV waveforms, in a three-step procedure. He first estimated the compliance, $\hat{C}$, then the resistance, $\hat{R}$, and finally the noninvasive ICP, nICP. He assumed ICP was constant at its mean level within each window, resulting in a single nICP estimate every estimation window,as clinical decision making relies on mean ICP measurements only. The Kashif time-domain algorithm performed accurately on a clinical dataset comprising 35 hours of data from 37 TBI patients, resulting in a bias of 1.6 mmHg and a SDE of 7.6 mmHg [6, 77]. While these results were extremely encouraging, the Kashif model had a fundamental drawback. The Kashif algorithm required the approximation of an unquantifiable phase lag/time delay between the ABP waveform, measured peripherally from the radial artery, and the CBFV waveform recorded cerebrally from the MCA. This phase lag arises due to path length variations and inherent physiological mechanisms, and the estimation performance was shown to be very sensitive to this phase lag [9, 22] and required significant consideration to estimate an optimal phase lag [9]. However, the proven validation performance of a simple, tractable model in a patient-specific manner was encouraging and motivated Noraky *et al.* to develop a similar model-based approach using a second-order model of the cerebral vasculature [7, 80]. Noraky attempted to overcome the fundamental limitations of the time-domain approach by implementing a frequency-domain based algorithm, and achieved encouraging results on a simulated dataset [80]. However, due to a few algorithmic approximations that could not be physiologically justified [81], the Noraky algorithm achieved clinically unacceptably large errors on a clinical dataset, with a bias of 13.7 mmHg and a SDE of 15 mmHg.

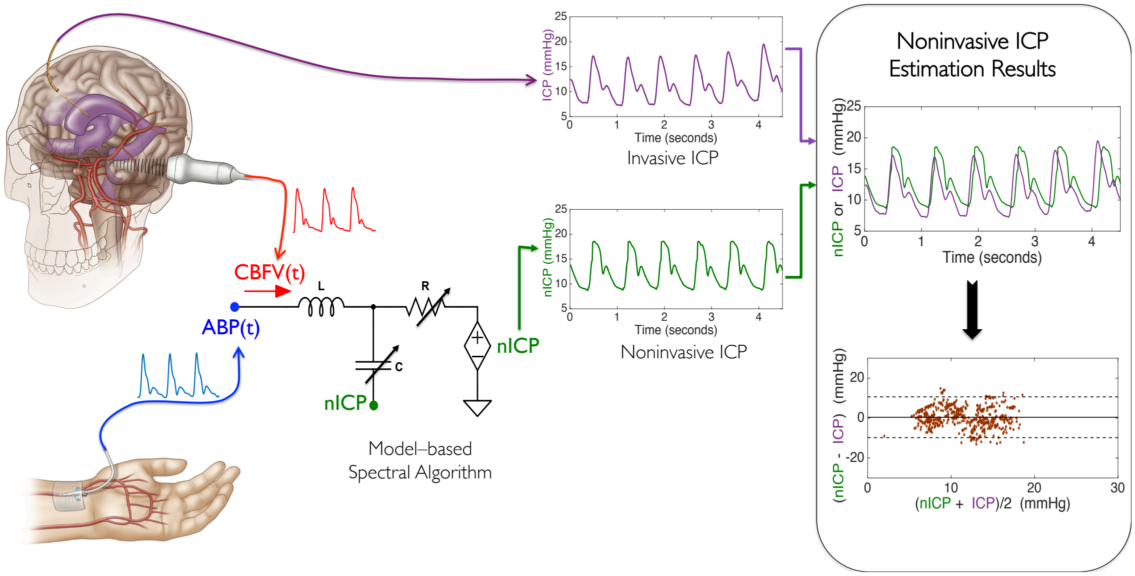

Figure 2-7: An overview of our model-based spectral approach to noninvasive ICP estimation. The model formulation, algorithm and validation results will be described in detail in the next chapters.

While both the Kashif and Noraky approaches had some limitations, they both motivated our work to a large extent. Noraky's idea of using a second-order circuit model and a spectral approach to overcome the fundamental limitation of a time-domain approach motivated our spectral approach, which is described in the next chapters.Kashif's impressive validation performance with a model-based approach provided a standard to compare our model-based nonivasive ICP estimation performance against. Additionally, both Kashif and Noraky emphasized the need to record high-resolution, annotated, time-aligned waveform data from the bedside to quantify any algorithm's estimation performance, as a major source of errors can be attributed to data-related issues. This also motivated us to design and deploy a custom data acquisition system in the ICU, to record waveforms in a controlled and efficient manner, while ensuring the high fidelity of all recorded waveforms. Hence, building upon the Kashif and Noraky approaches, we developed a model-based spectral approach to estimate ICP noninvasively in a patient-specific manner and validated the approach on two patient cohorts and a porcine model dataset. Our work is detailed in the remainder of this thesis, but an overview of our model-based approach is shown in Figure 2-7.

Chapter 3

Model-based Spectral Noninvasive ICP Estimation

Due to the importance of monitoring ICP in patients with neurological conditions and injuries and due to the inherent invasiveness of the currently used gold-standard ICP measurement modalities, there is a pressing need for an accurate, robust and clinically convenient noninvasive ICP measurement modality, as outlined in the previous chapter. In this chapter we propose a novel model-based spectral algorithm to estimate ICP noninvasively from ABP and CBFV waveforms. We first describe our proposed second-order, lumped parameter circuit model of the cerebral vasculature. We then describe our spectral algorithm in detail as well as the signal processing steps and important meta-data required for accurate computation of noninvasive ICP estimates. The contents of this chapter formed the basis of our publication in the IEEE Journal of Biomedical and Health Informatics [22].

3.1 Model of craniospinal physiology

Building on prior work by Kashif *et al.* [6,77,82], Noraky [7,80] proposed the second-order circuit model depicted in Figure 3-1 to represent a major cerebrovascular territory and its interplay with ICP. This model is based on a simplified mechanistic compartmental view of blood flow through the brain, in which $p_a(t)$ represents the ABP waveform at the inlet of a major cerebral vascular territory such as the middle cerebral artery (MCA), $q(t)$ represents the volumetric cerebral blood flow (CBF) into the vascular territory, and $p_{ic}(t)$ represents the ICP waveform. The inductor L models the inertia of blood, and the capacitance C represents the lumped compliance of the arterial vessel walls and surrounding brain tissue. The terminal pressure in the capacitive branch of the circuit is ICP, as the pressure external to the vessel and brain tissue is ICP. The resistor R models the viscous resistance to blood flow through the vascular territory, between the upstream arteries and downstream veins. However, ICP is typically larger than the cerebral venous pressure and since veins typically cannot sustain a negative transmural pressure, ICP is established as the effective downstream pressure [6]. This phenomenon is known as flow limitation in collapsible tubes and has been described in other physiological systems in which the pressure outside a collapsible structure exceeds the inside pressure. It is also commonly referred to as the Starling resistor effect [83]. Hence the blood flow through the cerebrovascular system is driven by the difference of the upstream ABP and effective downstream ICP, denoted as the cerebral perfusion pressure (CPP), which we will also denote as $x(t)$.

$$\text{CPP} \equiv \text{ABP} - \text{ICP} = p_a(t) - p_{ic}(t) \equiv x(t) \tag{3.1}$$

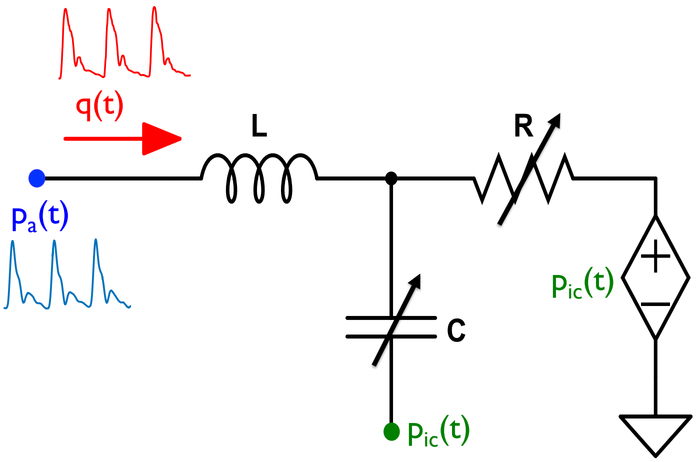

Figure 3-1: Schematic representation of the second-order circuit model [7].

3.1.1 Model formulation

The Kashif approach [6] implemented a time-domain model-based algorithm to noninvasively estimate ICP, using a peripherally measured ABP waveform, rather than the cerebral ABP, and a CBFV waveform, instead of the volumetric CBF waveform, as inputs. The primary limitation of this time-domain algorithm was the need to accurately estimate the inherent and unknown time - and corresponding phase - lag that exists between the cerebral ABP and CBFV waveforms, and to adjust the timing of the peripherally measured ABP waveform to compensate for this phase lag. Kashif *et al.* accounted for this by adjusting the timing of the ABP recording post-hoc based on physiological considerations. However, the resultant ICP estimates were very sensitive to this this adjustment, which motivated our approach of estimating ICP in the frequency domain. This is evident since a Fourier transform of the time-series physiological signals results in a transformation of all time-delays (int eh time-domain) to phase lags (in the frequency-domain), by fundamental properties of Fourier transforms [84]. Hence, by computing the power spectrum or square of the magnitude of these Fourier transformed signals, the phase lag is completely eliminated from the formulation, thus overcoming the limitation of the time-domain approach.

We used the model of the cerebral vasculature shown in Figure 3-1, described by the second-order equation

$$q(t) + \frac{L}{R}\frac{dq(t)}{dt} + LC\frac{d^2q(t)}{dt^2} = \frac{x(t)}{R} + C\frac{dx(t)}{dt} \tag{3.2}$$

which is obtained by applying Kirchhoff's current law and using the constitutive relationships for the inductor L, capacitor C, and resistor R.

A major advantage of using this lumped parameter circuit model is the invariance of the resulting ICP estimates to constant scaling (or linear transformation) of the CBF waveform, as also described by Kashif. To the extent that the CBFV waveform is linearly related to the volumetric blood flow (through scaling by the vessel's cross-sectional area), this invariance allows for the substitution of CBF by CBFV as one of the input waveforms [6]. As with the first-order Kashif model, Eqn. 3.2 is also invariant under linear transformations of $q(t)$, as can be verified by dividing Eqn. 3.2 by a non-zero scaling parameter β, to obtain

$$\frac{q(t)}{\beta} + \frac{L}{R\beta}\frac{dq(t)}{dt} + \frac{LC}{\beta}\frac{d^2q(t)}{dt^2} = \frac{x(t)}{R\beta} + \frac{C}{\beta}\frac{dx(t)}{dt} \tag{3.3}$$

which can be re-written, by replacing $\frac{q(t)}{\beta}$ with $\tilde{q}(t)$, as

$$\tilde{q}(t) + \frac{\tilde{L}}{\tilde{R}}\frac{d\tilde{q}(t)}{dt} + \tilde{L}\tilde{C}\frac{d^2\tilde{q}(t)}{dt^2} = \frac{x(t)}{\tilde{R}} + \tilde{C}\frac{dx(t)}{dt} \tag{3.4}$$

The linear scaling of Eqn. 3.2 results in an equation retaining its form with $q(t)$, R, C and L being replaced by $\tilde{q}(t) = \frac{q(t)}{\beta}$, $\tilde{R} = \beta R$, $\tilde{C} = \frac{C}{\beta}$ and $\tilde{L} = \beta L$, respectively. To the extent that the model is a realistic representation of the relevant cerebrospinal physiology, this scaling invariance has a major advantage as it allows for the replacement of the volumetric CBF, which is a parameter that cannot be measured continuously in real-time at the bedside with a scaled version without requiring a re-scaling of the pressure variables, including the ICP. Hence, CBF can be replaced by CBFV, if the two are related by a scaling factor, constant over some suitably chosen time window, accounting for the effective cross-sectional area of the vessel and possibly the Doppler angle. CBFV is routinely measured in patients by trans-cranial Doppler (TCD) ultrasonography and hence can serve as an easily measured input to our algorithm.

For notational simplicity, henceforth $q(t)$ will be used to denote CBFV, while R, C and L will denote the scaled versions of the original parameters. Hence, Eqn. 3.5 now represents the relationship between ABP ($p_a(t)$), CBFV ($q(t)$) and CPP ($x(t)$). To address the need for careful time alignment, we transform Eqn. 3.2 in its frequency-domain form and square the magnitude to eliminate the phase lag, resulting in

$$|Q(j\omega)|^2[(1-\omega^2LC)^2 + (\frac{\omega L}{R})^2] = |X(j\omega)|^2[\frac{1}{R^2} + (\omega C)^2] \tag{3.5}$$

where $Q(j\omega)$ and $X(j\omega)$ are the Fourier transforms of $q(t)$ and $x(t)$, respectively, and $j\omega$ is the complex frequency. The Fourier transforms can be computed over any suitably chosen time window, after accounting for the quasi-stationarity of the signals and to avoid aliasing [84].

The use of power spectra illustrates the advantage of estimation in the frequency domain, as it eliminates the need for careful estimation of the phase offset between the ABP and CBFV waveforms. Eqn. 3.5 can be solved using a constrained least-squares optimization at appropriately chosen frequencies ω_0, ω_1, ... ω_k, to obtain parameter estimates for R, L, and C, and ultimately an estimate of ICP. However any such least-squares formulation would require the prior knowledge of the unknown CPP spectrum, as $|X(j\omega)|^2$ depends on knowledge of the unknown ICP waveform, and Eqn. 3.5 relates the CBFV power spectrum, $|Q(j\omega)|^2$, to the CPP power spectrum . Hence, a valid algorithmic approximation of the CPP spectrum must be made in order to solve the least-squares optimization and ultimately estimate mean ICP.

3.1.2 CPP spectrum approximation

An approximation to $|X(j\omega)|^2$ can be obtained by observing the relationship between the measured ABP and ICP waveforms. This approximation is motivated by the recognition that the systolic upstroke of the ICP wavelet is driven by the ABP wavelet impinging on the intracranial tissue compartments [85, 86] and hence is often referred to as the percussion wave of the ICP waveform.

The relationship between the mean-subtracted ABP and ICP waveforms largely conforms to a characteristic shape over each beat, as shown in Figure 3-2, where the ABP-ICP dynamics were obtained from one patient over one 60-beat data window. The relationship exhibits two clear phases: one representing the systolic upstroke (from the onset of a beat to the systolic peak) and the other corresponding to the diastolic decay. We leverage this relationship to reconstruct the mean-subtracted ICP waveform from the mean-subtracted ABP waveform.

We define the mean-subtracted pressure waveforms over each beat as

$$\mathcal{P}_{ic}(t) = p_{ic}(t) - \overline{p_{ic}(t)} \tag{3.6}$$

$$\mathcal{P}_{a}(t) = p_{a}(t) - \overline{p_{a}(t)} \tag{3.7}$$

where $\mathcal{P}_{ic}(t)$ and $\mathcal{P}_{a}(t)$ are computed over each beat, and $\overline{p_{ic}(t)}$ and $\overline{p_{a}(t)}$ represent the mean

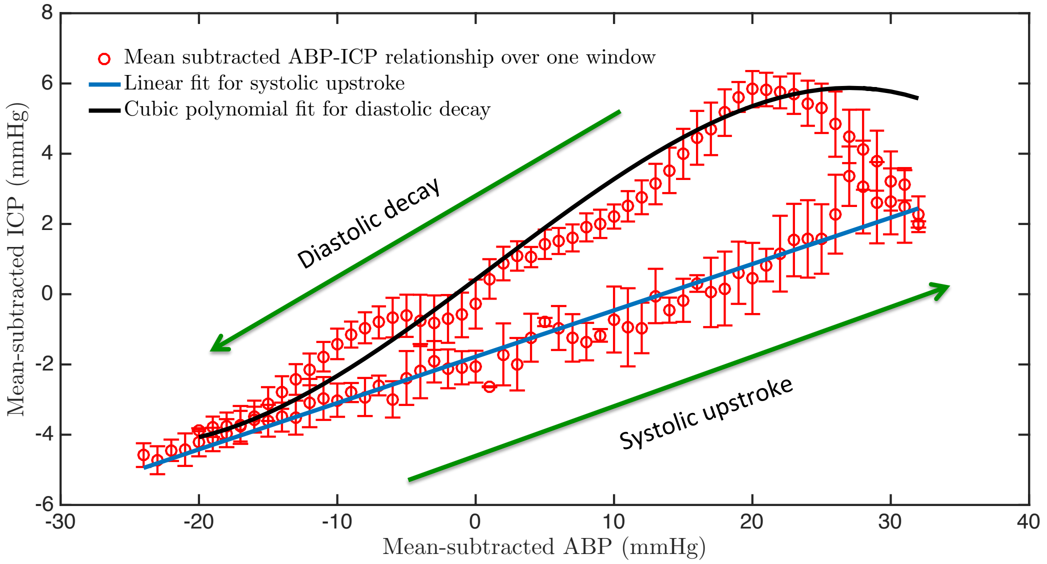

Figure 3-2: Representative example of the relationship between mean-subtracted ABP and mean-subtracted ICP over the duration of a 60-beat estimation window. There are two clear phases: a systolic upstroke (blue line) and a diastolic decay (black cubic polynomial). The error bars represent the standard deviation of error at each mean-subtracted ABP sample.

of the respective w‘aveforms over a beat. The systolic upstrokes and diastolic decays are fitted for these mean-subtracted waveforms.

The upstroke of the reconstructed mean-subtracted ICP waveform, $\mathcal{P}^u_{ic}(t)$, is modeled as a linear function of the mean-subtracted ABP waveform, $\mathcal{P}^u_a(t)$,

$$\mathcal{P}^u_{ic}(t) = \mathcal{P}^u_a(t) \cdot \alpha^u + \beta^u \tag{3.8}$$

with associated fitting parameters α^u and β^u. The diastolic portion of the reconstructed mean-subtracted ICP waveform, $\mathcal{P}^d_{ic}(t)$, is modeled as a cubic polynomial according to

$$\mathcal{P}^d_{ic}(t) = [\mathcal{P}^d_a(t)]^3 \cdot \alpha^d_3 + [\mathcal{P}^d_a(t)]^2 \cdot \alpha^d_2 + \mathcal{P}^d_a(t) \cdot \alpha^d_1 + \beta^d \tag{3.9}$$

with fitting parameters α^d_1, α^d_2, α^d_3 and β^d. The fitting parameters of these relationships can be determined in a training step, as described in the next chapter. Henceforth, $\mathcal{P}(t)$ will denote the mean-subtracted pressure waveforms, while $p(t)$ will represent the entire pressure waveform including the DC component.

The reconstructed mean-subtracted ICP wavelet, $\mathcal{P}^r_{ic}(t)$, is obtained for each beat by linking $\mathcal{P}^u_{ic}(t)$ and $\mathcal{P}^d_{ic}(t)$. Thus, the reconstructed mean-subtracted CPP, $\mathcal{X}^r(t)$, is obtained over each window by subtracting the mean-subtracted ABP and reconstructed mean-subtracted ICP

$$\mathcal{X}^r(t) = \mathcal{P}_a(t) - \mathcal{P}^r_{ic}(t) \tag{3.10}$$

It is important to emphasize that the relationship seen in Figure 3-2 and the reconstruction of CPP are with respect to the *mean-subtracted* waveforms and the ultimate aim is two-fold, namely to estimate the mean ICP over an appropriately chosen data window duration, and to estimate the ICP pulse pressure on a beat-by-beat basis.

3.2 Model-based ICP estimation

The ICP estimation procedure is performed on a windowed basis. An appropriate duration of data window is chosen, such that the assumptions of constant parameter values are valid, while also ensuring the presence of sufficient data variability and spectral richness. Once a window duration is chosen for implementation, the reconstructed ICP and CPP waveforms are computed from the ABP waveforms over each data window, as outlined above. We then identify, in a fully automated manner, the first n dominant peaks (ω_1, $\omega_2 \ldots \omega_n$) in the CBFV and reconstructed CPP spectra in each window, by estimating the heart rate from the ABP as the fundamental frequency ω_0, and scanning around integral multiples of ω_0 for spectral peaks. Thus, the frequency of each dominant peak is determined as

$$\omega_k = k \cdot \omega_0 + \epsilon_k;\ \ k = 1, 2, \ldots n \tag{3.11}$$

where ω_0 is the fundamental frequency and ϵ_k is a correction over the scanning range to locate the spectral peak. The motivation for only choosing the dominant peaks around the harmonics is due to the sparse nature of the power spectra of these physiological waveforms, with a sharp drop on either side of the dominant peak to the noise floor.

This process gives a total of $(n+1)$ spectral peaks for power spectral densities of $|X^r(j\omega)|^2$ and $|Q(j\omega)|^2$ in each window. A constrained least-squares optimization is formulated using the harmonic frequencies and their corresponding peak amplitudes. Note that the DC component has not been used in the least squares formulation. The choice of n must be such that the optimization problem is sufficiently well-conditioned, while also ensuring none of the dominant peaks are in the noise floor of the power spectrum. The resulting optimization problem is implemented as formulated in Eqn. 3.12,

$$min|| \begin{bmatrix} |Q(j\omega_0)|^2 \\ \vdots \\ |Q(j\omega_n)|^2 \end{bmatrix} - \begin{bmatrix} |X^r(j\omega_0)|^2 & \omega_0^2|X^r(j\omega_0)|^2 & -\omega_0^2|Q(j\omega_0)|^2 & -\omega_0^4|Q(j\omega_0)|^2 \\ \vdots & \vdots & \vdots & \vdots \\ |X^r(j\omega_n)|^2 & \omega_n^2|X^r(j\omega_n)|^2 & -\omega_n^2|Q(j\omega_n)|^2 & -\omega_n^4|Q(j\omega_n)|^2 \end{bmatrix} \vec{v}||_2^2 \tag{3.12}$$

where the auxiliary variables are related to the model parameters by the auxiliary equations

$$\begin{aligned} v_1 &= \frac{1}{R^2} \\ v_2 &= C^2 \\ v_3 &= \frac{L^2}{R^2} - 2LC \\ v_4 &= L^2C^2 \end{aligned}$$

and are subject to the constraints

$$\begin{aligned} v_1 &> 0 \\ v_2 &> 0 \\ v_4 &> 0 \\ v_3 &= \frac{v_1 v_4}{v_2} - 2\sqrt{v_4} \end{aligned}$$

The parameter estimates $\widehat{R}$, $\widehat{L}$ and $\widehat{C}$ for each window can be obtained from the solutions of the least-squares optimized parameters $\widehat{v_1}$, $\widehat{v_2}$ and $\widehat{v_4}$ according to

$$\widehat{R} = \frac{1}{\sqrt{\widehat{v_1}}} \tag{3.13}$$

$$\widehat{C} = \sqrt{\widehat{v_2}} \tag{3.14}$$

$$\widehat{L} = \sqrt{\frac{\widehat{v_4}}{\widehat{v_2}}} \tag{3.15}$$

Finally, the noninvasive estimate of mean ICP is computed for each estimation window as

$$\widehat{nICP} = \overline{p_w} - \widehat{R}\,\overline{q_w} \tag{3.16}$$

where $\overline{p_w}$ and $\overline{q_w}$ denote the window-averaged ABP and CBFV, respectively.

The reconstructed ICP waveform can be obtained over each window by adding the estimated mean ICP to the previously reconstructed mean-subtracted ICP.

$$nICP_{recon}(t) = \widehat{nICP} + \mathcal{P}^r_{ic}(t) \tag{3.17}$$

In addition to the window-by-window mean ICP estimates, we also compute the pulse pressure of the reconstructed ICP waveform, $PP^r_{ic}[n]$, as the difference between the maximum and minimum values of $\mathcal{P}^r_{ic}(t)$ over each beat. Since the peak of $\mathcal{P}^r_{ic}(t)$ also corresponds to the point where $\mathcal{P}^u_{ic}(t)$ and $\mathcal{P}^d_{ic}(t)$ are concatenated, there is a potential for artifacts at this point. Hence, the peak and trough of $\mathcal{P}^r_{ic}(t)$ are selected as the mean of three neighboring samples, after excluding spike-like artifacts. Another method to avoid these artifacts at the peak was to instead have a single constitutive fitting relationship between the mean-subtracted ABP and ICP wavelets, which was found to have similar performance, and is detailed in Chapter 6.

3.3 Data pre-processing

3.3.1 Signal Processing Pipeline

The estimation algorithm described above requires high-quality ABP and CBFV waveform recordings to generate estimates of ICP, since quantification of the algorithm's performance is meaningless if the inputs are noisy, contain artifacts or of low resolution. The peripheral ABP signal measured at the bedside was found to be comparatively free of noise, but was still subject to occasional corruption due to clogging or flushing of the catheter, and intermittent movement artifact. The CBFV waveform was far more prone to noise and artifacts, due to its high sensitivity to relative motion of the TCD transducer and the patient. Unlike the ABP waveform which is measured continuously in an automated manner once the artery is cannulated, measurement of a CBFV signal requires manual insonation of a blood vessel by a trained ultrasonographer. Hence, the CBFV signal also consisted of stretches of unusable data during periods in which the ultrasonographer searched for an acoustic window to obtain a continuous, strong acoustic signal from the MCA. Since our algorithm relies on the spectral information of the waveform recordings, the ICP estimates can be severely affected by poor signal quality and intermittent artifacts.

To guard against inclusion of stretches of data with unphysiological signatures or excessive noise, we have previously developed an automated signal waveform pre-processing pipeline, consisting of ABP and CBFV signal quality assessment, waveform synchronization, and beat-onset alignment [9]. The signal quality assessment pipeline rejects stretches of unusable waveform data due to a variety of metrics relying on the spectral content of the two waveforms and grounded in physiology. Once "good" data segments of ABP and CBFV, of a specified minimum duration, are identified, they are time-aligned based on the correlation of instantaneous heart rates computed from each of the waveforms.

3.3.2 Hydrostatic Correction

Another important data pre-processing step is to account for the hydrostatic correction between pressure measurements at bedside. Although our model assumes input ABP and

CBFV measurements referenced to a major cerebrovascular territory, such as the MCA, clinical ABP measurements are routinely obtained from a peripheral arterial site such as the radial artery, and referenced to the level of the left atrium. Therefore, we performed a hydrostatic pressure correction to account for the difference between the desired reference level (MCA) and the actual reference level (heart) of the ABP (Figure 3-3). This was done by measuring the height at which the ABP transducer was levelled at the bedside, denoted as h_{ABP}, and the height of the ICP transducer, denoted as h_{ICP}. These heights are significantly different, as patients in neurocritical care are routinely placed in the head-up position, to alleviate some of the intracranial trauma. Assuming the vertical height of the ICP transducer to be a good approximation for the vertical height of the MCA or major cerebral vessel, the mean pressure correction factor is computed from the height difference of a theoretical column of blood between the two transducer locations as

$$\begin{aligned} \Delta P_a &= \rho g \Delta h && (3.18) \\ \Delta h &= h_{ICP} - h_{ABP} && (3.19) \end{aligned}$$

where ρ denotes the density of blood and g denotes the acceleration due to gravity, taken as 9.8 m/s^2.

The density of blood can be computed from a recent hematocrit measurement from the bedside, as described by Hinghofer-Szalkay *et al.* [87], or by using an assumed blood density value of 1060 kg/m^3. As shown by Fanelli *et al.*, the difference in ΔP_a between the two choices of density has a negligible effect on the ICP estimation algorithm [9]. The heights of the transducers, h_{ABP} and h_{ICP}, are recorded for each measurement at the bedside, as described in the next chapter. Finally, ΔP_a is subtracted from the measured ABP waveform for each data segment to obtain the approximate MCA ABP waveform, and this corrected ABP serves as the true input to the spectral noninvasive ICP estimation algorithm described earlier. It is important to note the implicit assumption here that the difference between the ABP waveforms recorded at the radial and cerebral arteries is purely due to the hydrostatic column of blood, owing to a difference in the vertical height. There could also be morphological differences between the two waveforms, which are neglected

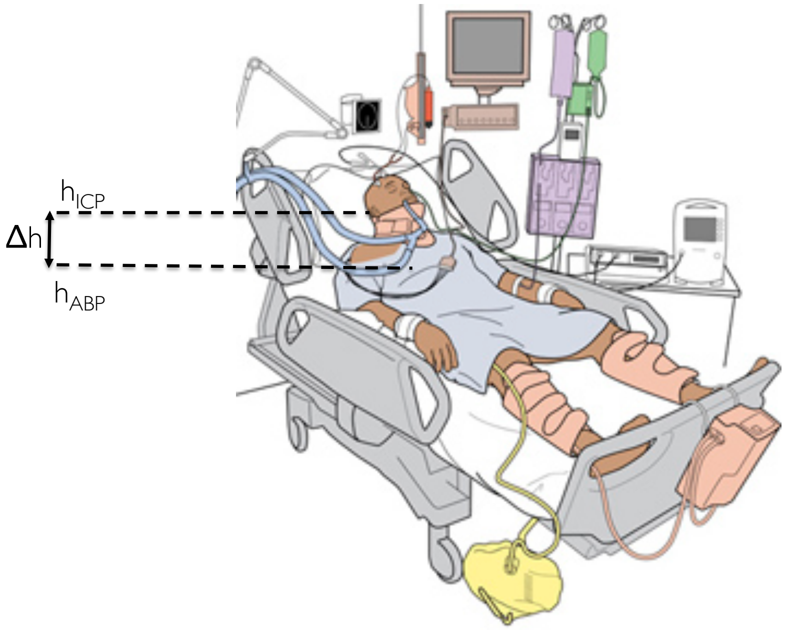

Figure 3-3: Schematic of a standard bedside setup with the vertical reference levels of the pressure transducers marked. Image adapted from [8].

here. Another important takeaway is that the hydrostatic correction factor solely affects the mean ABP. Hence, the effect of this correction is limited to the final estimation step of the algorithm, which directly depends on the window-averaged mean ABP, and this compensation does not affect the estimated circuit parameters $\widehat{R}$, $\widehat{L}$, and $\widehat{C}$.

Chapter 4

Clinical Data Acquisition and Validation on Patient Cohort

The performance of the noninvasive spectral algorithm outlined in the previous chapter and detailed in [22], needs to be validated on a clinical dataset, to test its accuracy in a real ICU setting. However, meaningful contextualization of these performance metrics rely on the availability of high resolution ABP and CBFV waveforms along a common time axis, along with other important meta-data such as the vertical heights of the pressure transducers. The lack of high resolution waveform data, or carefully controlled and annotated datasets can contribute to a large error in the performance metrics, as mentioned in past publications [6,9,22,80]. To overcome this challenge, we designed and deployed a custom data acquisition system in the neuro-ICU of a local Boston hospital, and the details of this system are detailed in this chapter and by Fanelli *et.al.* [88]. We then describe the clinical data acquisition procedure at Boston Medical Center, and detail the clinical dataset used for validating our algorithm, obtained from two different patient cohorts. Finally, we carefully analyze the performance of our noninvasive estimation algorithm on these patient datasets, and discuss the clinical significance of these results, and their comparison to previously reported results in literature.

4.1 Motivation for custom data acquisition system

Patients in neurocritical care are usually heavily instrumented and connected to various bedside monitoring devices. These devices measure physiological waveform signals, including ECG, SpO_2, ABP, ICP, RESP, temperature, and associated trends and features computed from these waveforms. Additional instrumentation may be present depending on the necessity, such as transcranial Doppler (TCD) ultrasonography or near-infrared spectroscopy (NIRS) [89].

Most bedside ICU monitors display a number of high-resolution data streams simultaneously, but do not archive these high-resolution waveforms for future use. Additionally, the transmission of multiple data streams out of these monitors are prone to errors in subsequent waveform alignment due to inaccurate time stamps. These limitations pose a challenge in accurately archiving waveforms at a high temporal resolution along a common time axis, as detailed by Fanelli [88].

In order to validate our spectral noninvasive ICP estimation algorithm, detailed in the previous chapter, we faced the need to archive high-resolution physiological waveforms recorded from multiple bedside devices. Additionally, the algorithm requires the recording of important meta-data from the bedside such as the vertical heights of pressure transducers, hematocrit values and important demographic and clinical information. The accurate time-alignment of these waveforms is crucial for waveform-based noninvasive ICP estimation approaches, as outlined by Fanelli [9]. Low temporal resolution or non-uniform time stamping of the recorded physiological waveforms can contribute to significant errors in estimation performance [6,80].These requirements motivated the development and deployment of a custom data acquisition system to record multiple physiological data streams and important ancillary data from the bedside, along a common time axis, in order to record a clinical validation dataset in a controlled manner.

4.2 Data acquisition system at Boston Medical Center

A typical neuro-ICU setup at Boston Medical Center has the patient instrumented with multiple sensors for measuring ECG, ABP, SpO_2, RESP, central venous pressure (CVP), temperature and ICP. All these sensors are connected to the GE Patient Data Module (PDM), which collects data streams from multiple bedside monitoring devices, processes them, and transmits the data to a compatible ICU monitor. The PDM can also store trend information at a very low resolution (1 sample per minute) for up to 24 hours [90]. All the ICUs at Boston Medical Center are equipped with GE Solar 8000i bedside patient monitors, each of which is connected to a PDM and display all the waveforms recorded from the patient described above. However, the patient monitors do not have an analog data interface for real-time waveform streaming and the temporal resolution of data stored in the PDM is too low for noninvasive ICP estimation purposes. Hence, we designed a data acquisition system to interface with the existing neuro-ICU setup at Boston Medical Center, as well as ensure accurate, time-aligned, high-resolution waveform data archiving.

Since the GE Solar 8000i bedside patient monitors do not have an analog data interface, our data acquisition system consisted of a GE TramRac 4A unit [91], to interface with the bedside patient monitor, and a Microsoft Windows-based computer for controlling the data archiving process and for storage of the time-aligned waveform data. The TramRac effectively served as a port replicator for the Solar 8000i's PDM, providing access to waveforms from up to thirteen attached sensors through an analog data interface. Typically, the waveform signals streamed through the monitor to our system included multi-lead ECG, SpO_2, ABP, CVP, and ICP. Additional data streams specifically recorded for our study purpose included a noninvasive ABP signal recorded from the BMEYE Nexfin monitor, and the CBFV waveform recorded from either the DWL Doppler BoxX (Compumedics, Singen, Germany) or the Philips CX-50 (Philips Healthcare, Andover, MA) TCD ultrasound device, . The Nexfin noninvasive ABP monitor and the DWL ultrasound device both have a dedicated analog output, through which the waveform data can be streamed directly to our system. The Philips CX-50 does not allow for real-time streaming of the analog waveform data, and hence the CBFV data collected on this device were aligned with all the other data streams in post-processing, by correlating the instantaneous heart rates. All the data streams (from the GE Monitor and external devices), except the CX-50 CBFV data, are fed to an analog-to-digital converter (National Instruments DAQ 6218), and sampled at 250 samples/second at 16-bit amplitude resolution.

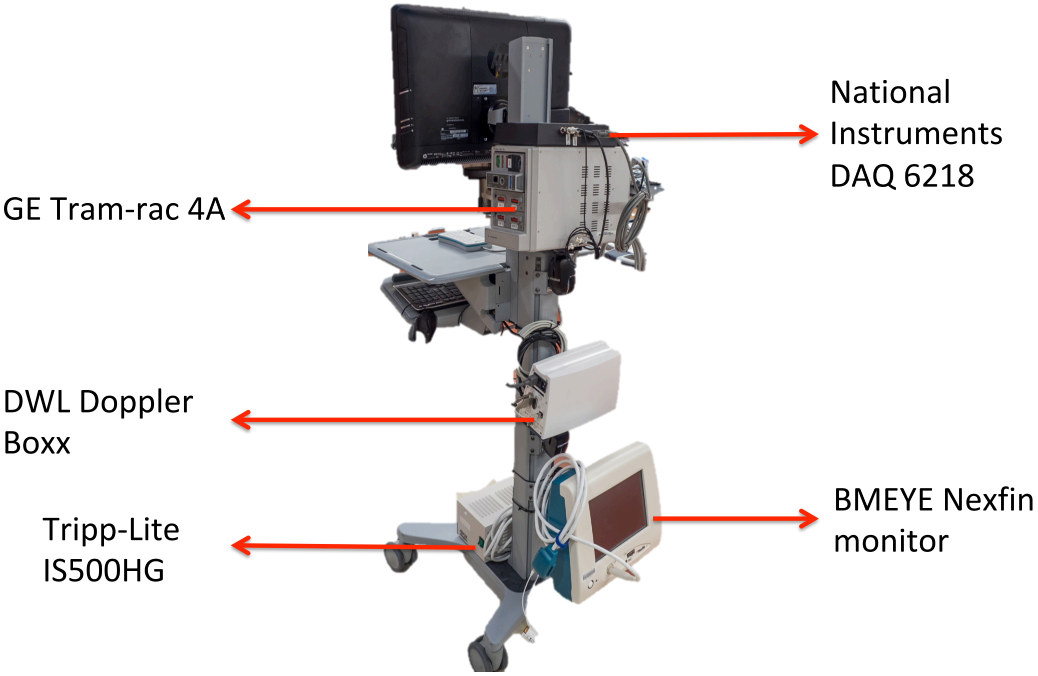

Figure 4-1: Data acquisition system deployed at Boston Medical Center.

Data acquisition, visualization and annotation are controlled on a computer by a custom designed LabView Virtual Instrument (VI), allowing for time-stamped annotations of important clinical, patient and study notes. The VI is configured to automatically duplicate the recorded data and create both an identifiable and de-identified version of the recorded data. Both these copies of the patient data are automatically organized into separate directory trees to reduce the risk of accidentally accessing protected health information (PHI), and to eliminate the need for tedious post hoc de-identification. All the data are archived on an encrypted hard drive at the end of each recording session. In addition to the waveform data recorded, the VI allows for recording of ancillary data to better contextualize and interpret the validation results post-hoc. These ancillary data include the following

- **Patient demographic information:** Age, gender, race, ethnicity
- **Clinical information:** Diagnosis, site of neurological injury, Glasgow Coma Scale (GCS) score, hematocrit, medications administered
- **Study information:** Date and time of recordings, medical record number (MRN), study ID
- **Important meta-data:** Vertical heights of ABP and ICP transducers (essential for hydrostatic correction in the estimation algorithm), type and placement of ICP probes (EVD or parenchymal), state of EVD drainage
- **Recording observations:** A textbox is also provided for recording of any potentially significant observations made during the recording session

The entire data acquisition system was designed on a small footprint movable Ergotron medical cart to enable agile movement inside a crowded ICU. The patient is electrically isolated and protected from macroshock hazards by powering all devices through a cart-based Tripp-Lite IS500HG isolation transformer. The design and details of the data acquisition system were originally published by Fanelli [88].

4.3 Protocol for clinical recording of data

Clinical data collection at Boston Medical Center was approved by the Institutional Review Boards at Boston Medical Center and MIT. Patients in the neurocritical care are regularly screened to check for compliance with all the inclusion criteria for our study, before they are enrolled in the study. For enrollment, informed consent is obtained from the patients or their legally authorized representative. Once consent is obtained, the data acquisition cart is wheeled into the ICU and turned on, after consulting with doctors and nurses to ensure no disruption to standard medical care to be provided to the patient. The sensor cables for ECG, SpO_2, ABP, CVP and ICP are disconnected from the PDM in the GE Solar 8000i bedside monitor, and connected to the TramRac 4A instead. During the process, there is a short interruption of patient data recording for around 30 seconds, which is communicated to the clinical staff beforehand. Once the re-cabling process is completed, the clinical staff zeroes all pressure sensors to ensure accurate pressure recordings. Simultaneously, the custom-designed LabView VI is opened and all ancillary patient information are recorded on the VI, including demographic, clinical and study information. Accurate measurements of the heights of the various pressure transducers are made and logged in the VI as well. At this point all waveforms from the patient monitor are visualized on a common time axis on the VI. These include the multi-lead ECG, SpO_2 recorded using an optical sensor on the finger, invasive ABP measurement recorded using a radial arterial line, and invasive ICP recorded from either an EVD or parenchymal probe. A trained ultrasonographer then attempts to locate and insonate the MCA through the temporal acoustic window on one side, using either the DWL Doppler BoxX or the Philips CX-50 ultrasound system. Once the MCA has been visualized and while the vessel is being insonated, a stable CBFV envelope is streamed and recorded on the same time axis. All data streams are recorded continuously for around 20 to 30 minutes before the MCA on the contralateral side of the patient is located and the procedure is repeated. Throughout the recording session, notes and observation pertaining to the recording session are logged in the VI. At the end of each session, the sensor cables are reconnected to the PDM in the patient monitor and the pressure signals are zeroed again.

Ideally, each recording session yields around 40 to 60 minutes of high-resolution, time aligned waveform data. However, in practice, the duration of useful clinical data obtained is far less due to a variety of issues. The CBFV waveform requires the manual location and insonation of the patient's MCA by an ultrasonographer, and the stability of the signal depends on the operator's ability to keep the transducer locked on to the vessel. However, due to potential movement of the patient and/or the ultrasonographer, he ultrasound probe often slips off the MCA, resulting in a loss of signal and requiring the re-positioning of the probe to locate the MCA again. As a result, the duration of good quality CBFV signal is usually less than the expected 20 to 30 minutes. Other sources of error with respect to the CBFV are associated with the inability to locate the MCA accurately, possibly due to the lack of an acoustic window in the patient, irregular anatomy of the Circle of Willis, or

Table 4.1: Table describing the demographics of the adult patients included in the clinical dataset for validation of the algorithm.

Patient	Gender	Age (Years)	Duration	Diagnosis
1	Male	52	8 minutes	TBI
2	Male	20	12 minutes	TBI
3	Male	47	10 minutes	Brain tumor
4	Male	40	55 minutes	TBI
5	Female	74	23 minutes	Hydrocephalus

a potential injury in the region of insonation. While less prevalent than CBFV artifacts, artifacts can be present in the ABP waveform also, due to movement of the patient or placement of the radial line too close to the vessel wall or flushing of the catheter.

4.4 Patient cohorts for algorithm validation

4.4.1 Adult population

The adult dataset was recorded on the custom data-acquisition system described in Section 4.2, fromt he neuro-ICU at Boston Medical Center. The signal preprocessing pipeline described in the previous chapter selected a total of one hour and 48 minutes of high quality data for validaiton of the noninvasive ICP estimation algorithm. The validation data were recorded from sixteen studies recorded on five patients (4 male, 1 female). These studies were recorded between February and September 2016. The patients ranged in age from 20 to 74 years (median of 47 years) and were hospitalized for severe TBI (3 patients), brain tumor (1 patient), and acute hydrocephalus (1 patient) (Table 4.1).

4.4.2 Pediatric population

A custom data acquisition very similar to the previously described one was also deployed at Boston Children's Hospital to record pediatric data [9] to go along with the adult patient population recorded at Boston Medical Center. The pediatric patient dataset has been previously reported and was collected at Boston Children's Hospital [9]. Briefly, a custom data-acquisition system, similar to the previously described one, was deployed in the hospital's Medical and Surgical Intensive Care Unit for collection of high fidelity waveform recordings and ancillary demographic and clinical information and meta data related to the data-acquisition process. Data collection was approved by the Institutional Review Boards at Boston Children's Hospital and MIT, and informed consent or – when appropriate – assent were obtained from the patient or their legally authorized representative. Pediatric patients in whom invasive ICP monitoring was indicated as part of routine clinical care were eligible for enrollment [9].

A total of 41 studies from thirteen patients (nine males, four females), recorded between February 2015 and June 2017, were used for validation of the spectral noninvasive ICP estimation algorithm outlined in the previous chapter. The dataset consists of a diverse population of patients, with ages ranging from 2 to 25 years (median of 11 years) and presenting with various conditions requiring invasive ICP as part of standard practice of care, including TBI, hemorrhagic strokes, hydrocephalus, and metabolic abnormalities. From the pediatric dataset, the preprocessing pipeline identified a total of around six hours and 40 minutes of good quality data segments across the thirteen patients for validation of our algorithm (Table 4.2).

Table 4.2: Patient demographic, clinical and study information of the pediatric patients included in the clinical dataset for validation of the algorithm.

Patient	**Gender**	**Age (Years)**	**Duration**	**Diagnosis**
1	Male	12	2 hours 3 minutes	Stroke
2	Female	16	45 minutes	TBI
3	Male	14	18 minutes	Stroke
4	Female	2	24 minutes	Hemorrhage
5	Female	11	10 minutes	Brain tumor
6	Male	18	30 minutes	Intraventricular hemorrhage
7	Male	20	27 minutes	Hydrocephalus
8	Male	11	9 minutes	TBI
9	Male	7	45 minutes	TBI
10	Female	6	2 minutes	Hydrocephalus
11	Male	4	36 minutes	Cerebrohepatopathy
12	Male	6	30 minutes	Cavernous malformation
13	Male	25	11 minutes	Chiari malformation

4.5 Estimation results on pediatric and adult data

4.5.1 Algorithmic specifications

The spectral algorithm for noninvasive estimation of ICP outlined in the previous chapter was implemented on a non-overlapping window-by-window basis. Similar to Kashif *et al.*, within each window, the values of the circuit parameters (R, L and C) are assumed to be constant and the ICP is assumed to be constant at its mean level. The duration of the data window was chosen to be long enough for availability of sufficient spectral richness in the waveform data, but also short enough for the algorithmic approximations of constant circuit parameter values to be valid. For implementation purposes, a data window duration of 60 beats was chosen, similar to past implementations [6, 7, 9], resulting in a single mean ICP estimate every 60 beats. Within each data window, the dominant peaks in the power spectra of the CBFV and reconstructed CPP spectra are identified, for solving the constrained least-squares optimization problem described in Eqn. 3.12. Since the spectral data in these physiological waveforms is sparse, each estimation window was further divided into two non-overlapping subwindows, each 30 beats in duration, for the power spectral density computations. The power spectral densities $|\mathcal{X}^r(j\omega)|^2$ and $|Q(j\omega)|^2$ are then computed over each sub-window, using a Hamming-window based averaged periodogram method with 50% overlap, and the four dominant peaks in each subwindow are picked in a fully automated manner (Figure 4-2). This process results in a total of eight spectral peaks over each estimation window ($n = 7$ in Eqn. 3.12).

The training of the fitting parameters, α^u and β^u for the upstroke, and α_1^d, α_2^d, α_3^d and β^d, for the downstroke, was performed on a very small subset of the pediatruic patient cohort. Only three of the pediatric data segments (less than 2% of the pediatric dataset) were chosen to serve as the training set, and the ICP was not blinded only in these data segments. The fitting parameters obtained from this training step were used for validation of the algorithm on the rest of the pediatric dataset and the entire adult dataset, without any modifications to the estimation algorithm.

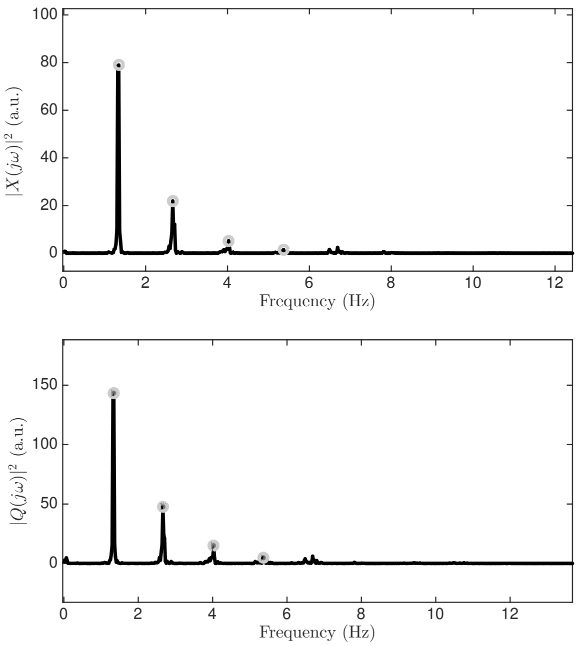

Figure 4-2: Example of power spectra of mean-subtracted CPP and CBFV waveforms as computed by the average periodogram method. The first four harmonic peaks are identified in each spectrum.

4.5.2 Error metrics

The estimation results presented in the thesis henceforth are quantified in terms of the mean estimation error (bias or accuracy), the standard deviation of the error (SDE or precision), and the root mean squared error (RMSE) of the ICP estimates with respect to the mean of the invasively measured ICP.

$$\text{bias} = \frac{1}{n}\sum_{i=1}^{n}(nICP_i - \overline{ICP_i}) \tag{4.1}$$

$$\text{SDE} = \sqrt{\frac{\sum_{i=1}^{n}(nICP_i - \overline{ICP_i} - bias)^2}{n-1}} \tag{4.2}$$

$$\text{RMSE} = \sqrt{\frac{\sum_{i=1}^{n}(nICP_i - \overline{ICP_i})^2}{n}} \tag{4.3}$$

where $\overline{ICP_i}$ is the mean measured ICP, and $nICP_i$ is the mean ICP estimate, both for the i^{th} 60-beat estimation window. Additionally, we compute the accuracy and precision errors for the estimated beat-by-beat ICP pulse pressure.

4.5.3 Mean ICP estimation

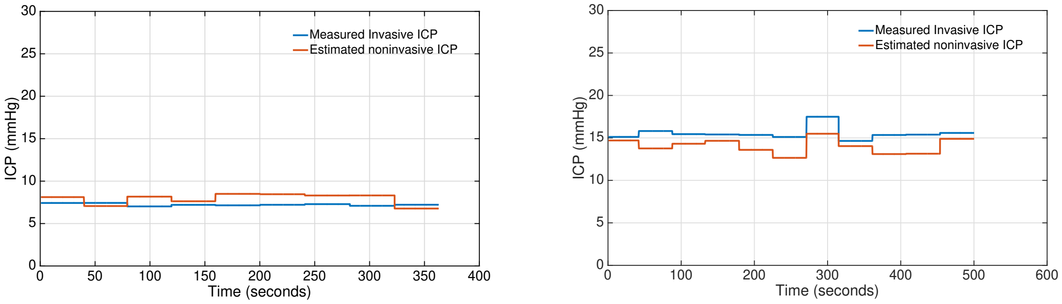

(a) Data segment 1 (b) Data segment 2

Figure 4-3: Representative examples of noninvasive ICP estimation performance on two segments from different patients.

The spectral estimation algorithm described in the previous chapter was validated on the two clinical datasets detailed above, and these results are also detailed in [22]. The pediatric dataset yielded 514 60-beat estimation windows of sufficiently high data quality from thirteen patients. Overall, the mean measured ICP ranged from 1.3 to 24.8 mmHg, with a mean and median of 11.2 mmHg and 10.3 mmHg, respectively [22].

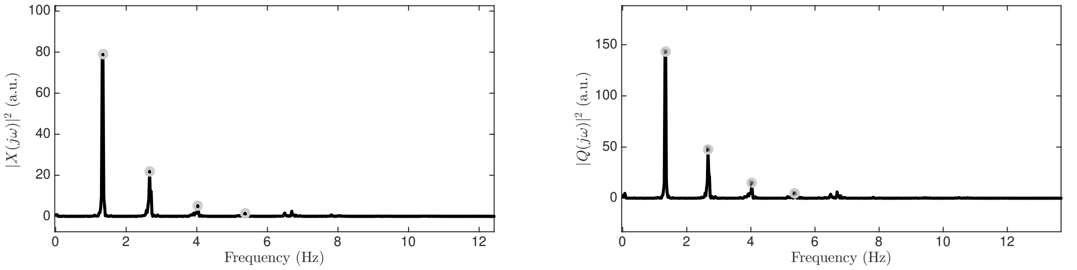

(a) Pediatric population (b) Adult population

Figure 4-4: Bland-Altman plot comparing estimated and mean measured ICP on a window-by-window basis across all patients in the pediatric and adult datasets.

On the pediatric dataset, the algorithm achieved an overall estimation accuracy of 0.4 mmHg, a SDE of 5.1 mmHg, and a RMSE of 5.1 mmHg in estimating mean ICP. Figure 4-3 shows the performance of the estimation algorithm on two different patients, with different levels of mean ICP. The overall performance of the algorithm on a window-by-window basis are summarized in the Bland-Altman plot [92] shown in Figure 4-4a. These summary results are essentially in agreement with those obtained on the same datasets using the Kashif algorithm, as implemented by Fanelli [9], requiring careful time alignment between the ABP and CBFV waveform recordings [9]. In contrast, the Noraky algorithm [80] achieved a bias of 5.4 mmHg, an SDE of 11.2 mmHg, and a RMSE of 12.5 mmHg on the same dataset, which are clinically unacceptable.

The adult dataset yielded one hour and 48 minutes of high fidelity data from five patients, resulting in 138 60-beat estimation windows. This population served as a completely independent validation dataset, as no previous training was performed on the adult data, and the equipment and study staff was completely different from those of the pediatric study. Our algorithm achieved an accuracy of −1.5 mmHg, a SDE of 4.3 mmHg and a RMSE of 4.5 mmHg in estimating mean ICP on this adult dataset, as summarized in the Bland-Altman plot in Figure 4-4b. To put these validation results into context, when we separately derived the fitting parameters of our spectral estimation approach from all available adult data and then performed the nICP estimation on the adult data we obtained a bias of −0.9 mmHg, a SDE of 3.6 mmHg, and a RMSE of 3.7 mmHg. This approach essentially amounts to a training performance as we derive the fitting parameters and the estimation performance on the same set of (adult) data. It is therefore an upper limit on the quality of results that can be expected. This exercise demonstrates that the estimation performance obtained on the adult data when the fitting parameters are trained on a small subset of the pediatric data is very close to and – for all clinical purposes – essentially the same as when the method is trained on all adult data.

When pooling both the pediatric and adult data and evaluating the performance of the spectral estimation approach on the combined dataset, we obtain an overall accuracy of 0.1 mmHg, a SDE of 5.1 mmHg, and an RMSE of 5.1 mmHg. To further summarize the overall performance of mean ICP, we analyzed the estimation performance on a window-by-window, study-by-study and patient-by-patient basis. We generated the cumulative distribution functions of the RMSE for these analyses across both datasets (Fig. 4-5). Around 80% of our window-by-window mean ICP estimates fall within a RMSE of 6 mmHg.

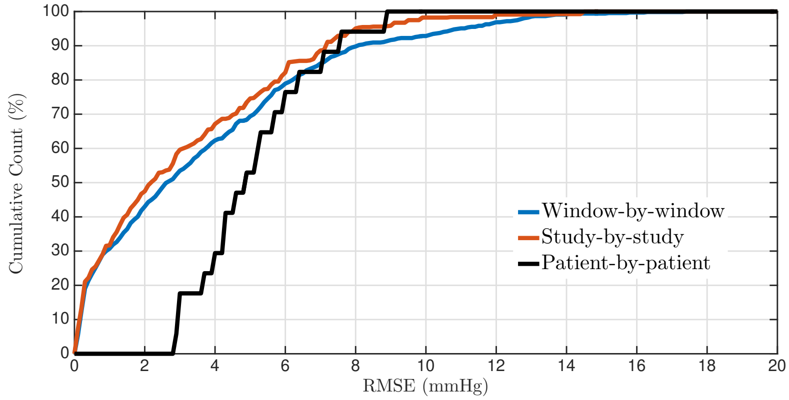

Figure 4-5: Cumulative distribution functions for the nICP RMSE on both datasets together. The analysis is carried out on a window-by-window, study-by-study, and patient-by-patient basis.

4.5.4 Robustness of the mean ICP estimates

The time offset between a CBFV wavelet recorded at the middle cerebral artery and the corresponding ABP wavelet recorded peripherally depends on physiological factors and internal processing delays of the recording devices [9]. Estimation algorithms that process these signals in the time domain therefore need to estimate a physiologically plausible time offset and adjust the relative timing of these waveforms for each recording [6, 7, 9]. To evaluate the sensitivity of the ICP estimates to temporal misalignment of the CBFV and ABP waveforms, we shifted these waveforms out of phase, one sampling interval at a time, and computed the RMSE between the nICP estimate and mean measured ICP for the spectral estimation approach and the time-domain estimation approach on the pediatric dataset.

The RMSE of the spectral approach remains entirely unaffected by the waveform misalignment, while the time-domain approach only produces credible estimation results for a narrow range of offsets of only about 8 sampling intervals, or 64 ms (Fig. 4-6). Applying the Kashif algorithm to the pediatric dataset without conducting the beat-onset adjustment outlined by Fanelli [9] resulted in a bias of −4.2 mmHg, a SDE or 70.2 mmHg and a RMSE or 70.4 mmHg, demonstrating the sensitivity of the time-domain approach to estimating a physiologically plausible offset between the two waveforms, while the spectral approach is insensitive waveform misalignment as long as the two waveforms are not shifted by more than an entire beat.

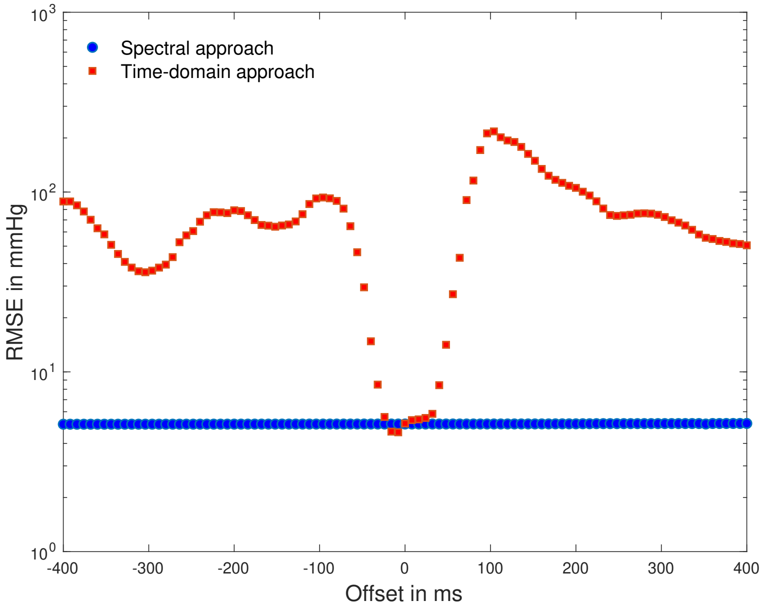

Figure 4-6: RMSE between nICP estimates and mean measured ICP as a function of timing offset between ABP and CBFV waveforms. The zero offset relates to the beat-onset alignment described by Fanelli and co-workers [9].

To evaluate the sensitivity of our nICP estimates to the identification of the peaks in the CPP and CBFV spectra we computed the nICP estimates on the basis of the spectral amplitudes associated with the frequency bins to the right or left (selected at random) of the frequencies corresponding to each of the spectral peaks. This analysis resulted in a bias of 1.2 mmHg and RMSE of 6.7 mmHg, indicating that slight errors in identifying the dominant spectral peaks can decrease the performance appreciably.

4.5.5 ICP pulse pressure estimation

Our spectral algorithm was also used to reconstruct the ICP waveform from the ABP waveform, based on the fitting parameters obtained from the training data. For every cardiac cycle, a mean-subtracted ICP waveform was reconstructed. An example of the reconstructed ICP waveform and the corresponding reference clinical ICP is shown in Figure 4-7. The pulse pressures, $PP^r_{ic}[n]$ and $PP_{ic}[n]$ of the reconstructed and measured ICP waveforms, respectively, were calculated for every beat and compared. This analysis was performed on a total of 12984 beats from eight patients from both datasets, with a range of pulse pressures

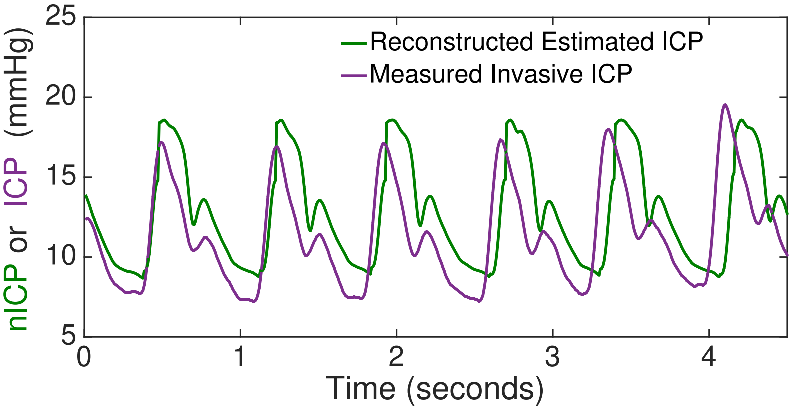

Figure 4-7: Comparison between the algorithmic reconstruction of the ICP waveform from ABP and the clinically obtained gold-standard ICP measurements.

from 3 mmHg to 18 mmHg. Some of the data windows from both datasets were rejected because the ICP exhibited non-physiological pulsatility, as could arise due to opening of the EVD to drain CSF. Our reconstructed ICP pulse pressure estimates had a bias of 1.3 mmHg, SDE of 2.9 mmHg and a RMSE of 3.2 mmHg. Sixty six pecent of all ICP pulse pressure estimates fall within ±3 mmHg, and 87% of estimates fall within ±5 mmHg of the measured ICP pulse pressure. The full distribution of errors in estimating pulse pressure on a beat-by-beat basis is shown in Figure 4-8.

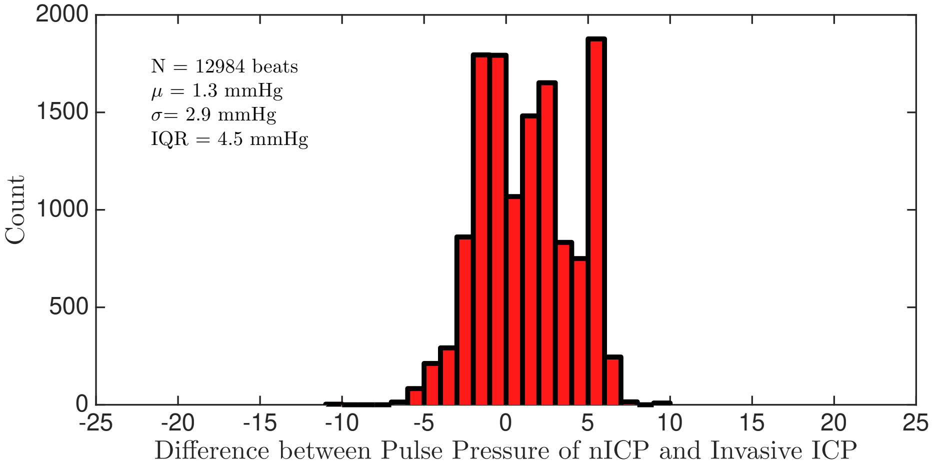

Figure 4-8: Distribution of ICP pulse pressure estimation errors.

4.6 Discussion of validation results and limitations

Noninvasive assessment of brain health remains one of the pressing open challenges in clinical neuroscience. To address this need, a series of model-based approaches to noninvasive and continuous ICP estimation have recently been proposed based on the analysis of time-locked measurements of CBFV and (peripheral) ABP waveform measurements [6,7,9,66,76–78,80]. Some of these approaches rely on reduced-order models of the cerebrospinal physiology [6,7,9,76–78,80] while others represent the relevant anatomy and physiological relationships in more detail [66]. The majority of prior work has approached the estimation problem in the time domain, which requires consideration of how to align the waveform measurements and thereby overcome temporal offsets inherent in measuring physiological waveforms with different medical devices and at different anatomical locations. In pre-processing steps Kashif [6] and Fanelli [9] aligned the waveforms to approximate the phase relationship that can plausibly be expected to exist between CBFV and the ABP waveforms measured simultaneously at the MCA. Imaduddin [78] made the offset an explicit modeling parameter and later marginalized a likelihood function over all plausible offsets. Our work here was directly motivated by the recognition that solving the estimation in the frequency domain should be immune to misalignment of the ABP and CBFV waveform recordings. While we demonstrated that this is indeed the case using clinical datasets for validation, the approach required estimation of the CPP power spectrum and hence necessitated a heuristic estimation of the ICP pulsatility. We based our estimation on the fact that the initial upstroke of the ICP wavelet (the percussion wave) is driven primarily by the systolic upstroke of the ABP waveform [85, 86]. While the ICP waveform morphology also depends on the biophysical properties of the cerebrospinal fluid space and surrounding brain tissue, the assumption that the ICP pulsations are largely driven by the ABP pulsation allowed us to make the spectral estimation problem tractable.

The resulting estimation accuracy and precision of our spectral estimation algorithm are highly encouraging, as an overall accuracy of 0.1 mmHg, a SDE of 5.1 mmHg, and a RMSE of 5.1 mmHg in estimating the mean ICP are well within the errors reported when comparing the currently used invasive ICP measurement modalities [35,36,49]. Lescot *et al.* [49], for instance, compared the Pressio and Codman intraparenchymal sensors to ventricular ICP measurements in thirty patients. They reported measurement accuracies of −0.6 and 0.3 mmHg between intraparenchymal and ventricular measurements with the Pressio and Codman devices, respectively, with 95% limits of agreement (bias ± 1.96 SD) of (−8.1 mmHg, 6.9 mmHg), and (−6.7 mmHg, 7.1 mmHg), respectively. Brean *et al.* [50] compared simultaneous ventricular and intraparenchymal (Codman) ICP measurements in one patient undergoing treatment for subarachnoid hemorrhage. They reported a measurement bias of 0.7 mmHg with a standard deviation of 6.8 mmHg across 218,589 comparisons. In a recent meta-analysis of invasive ICP measurement approaches, Zacchetti *et al.* [36] reported a mean error between invasive measurements of 1.5 mmHg with an associated 95% confidence limit of 0.7 to 2.3 mmHg. Some of these discrepancies between different modalities might be due to possible natural or pathology-dependent pressure gradients within the CSF space (as demonstrated by Eide [51]), to hydrostatic differences between the location of the EVD and parenchymal transducers or due to sensor inaccuracies. These reasons for different readings notwithstanding, the parenchymal and EVD measurements are both standards-of-care in many neurosurgical and neurocritical settings [93]. Hence, it is highly encouraging that our results are comparable to the currently accepted invasive clinical standards of ICP monitoring.

The accuracy and precision achieved by our spectral estimation approach are also in line with those reported by Fanelli *et al.* [9] and Imaduddin *et al.* [78] on the same pediatric dataset. Hence, despite our having based our estimation of the ICP pulsatility on the ABP pulsatility, our algorithm performed in a manner entirely comparable to some of the previous estimation strategies, using similar model-based approaches.

The implementation of our approach requires one training step to obtain the fitting parameters in order to reconstruct the estimated ICP waveform. Here, this training was performed on a small fraction (less than 2%) of the pediatric dataset. The remaining pediatric population was diverse, representing a wide range of age, body size, and neurological and neurosurgical conditions. Moreover, we did not retrain the model on the adult data, which was collected in a different hospital, involving different bedside monitoring devices, and different study staff. Our algorithm still achieved very encouraging results on this (albeit small) hold-out validation dataset, thus suggesting that the relationship between mean-subtracted ICP and mean-subtracted ABP has a sufficient degree of robustness to be valid.

Our algorithm also has the advantage over other model-based noninvasive ICP estimation methods [6, 7, 9], of estimating the pulse pressure by reconstructing the ICP wavelet from each beat of the ABP signal. While the estimate of mean ICP obtained is clinically acceptable and sufficient for clinical monitoring, an estimate of the ICP pulse pressure is thought to provide valuable additional information. The pulsatility of the ICP waveform could be a useful indicator of intracranial compliance [27], and variations in pulsatility have been linked to intracranial hypertension, or hydrocephalus [28, 51, 94]. Compared to other noninvasive ICP estimation techniques that result only in an estimate of the mean ICP, our frequency-domain algorithm has the added benefit of estimating the pulsatility as well.

Our estimation approach and associated validation strategy have some limitations that have to be further explored. First, while we were able to collect sufficient patient data to validate our estimation approach in the clinically important ICP transition range between 15 to 25 mmHg, we were not able to evaluate the approach in the pathological ICP range of 25 to 40 mmHg. This is due to the fact that patients in neuro-ICUs are constantly monitored by the clinical staff and their health is the utmost priority. As a result, care is taken to ensure that their ICP is kept within acceptable limits, and adverse events result in immediate interventions. As a result, we were unable to validate our algorithm on ICP measurements above 25 mmHg or record any significant trends in ICP. The data also exhibited low variability in the ICP pulse pressures, making it difficult to definitively evaluate the accuracy of our pulsatility estimation. On the technical side, one of the major practical limitations is the use of radial ABP as a surrogate for the MCA ABP. While we do apply a hydrostatic correction to account for differences in mean pressure, it is expected that the two waveforms are morphologically different, which is not accounted for int he spectrum computation. Any potential morphological variations would affect the spectral estimation which relies on the frequency characteristics of the ABP and CBFV waveform recordings. Finally, our spectral estimation approach relies on the estimation of the ICP pulsatility from the ABP pulsatility. A mechanistic understanding of how the ICP waveform relates to the

ABP waveform and the biophysical properties of the intracranial compartments would allow us to improve upon our method, though development of such a detailed understanding currently remains an open challenge in clinical neuroscience.

Chapter 5

Porcine Model for Probing Intracranial Dynamics

As detailed in the previous chapter, the performance of the spectral noninvasive ICP estimation algorithm on two different patient cohorts was highly encouraging, and was found to be comparable to the currently used invasive ICP measurement modalities and past attempts at noninvasive ICP estimation. However, the range of measured ICP in the the patient cohorts was limited and hence the robustness of the algorithm could not be quantified in the pathological ICP ranges of 25 mmHg and above. In this chapter, we begin by detailing the fundamental limitations of using human neurological data for clinical validation, and motivate the use of a newly developed porcine model for probing intracranial dynamics. We then describe the extensive preparatory work performed to understand the anatomical challenges of a swine model. Finally, we detail the experimental protocol for manipulating the ICP in the porcine model and for monitoring the physiological response of the animal, primarily to validate the noninvasive ICP estimation algorithm over a wide range of ICP.

5.1 Porcine large animal model

The importance of developing an accurate and robust noninvasive ICP measurement modality has been detailed in the previous chapters, and most of the approaches described in the literature, including our spectral approach, have been validated on human waveform data collected from patients in neurocritical care [6,9,22,35,78]. However, using human neurological data for clinical validation poses an inherent difficulty due to the need to intervene aggressively in response to ICP elevations. As a result, the patients' neurological health and physiological stability must always remain the foremost priority. Hence, if the patient's neurological health is potentially compromised at any time the clinical staff intervene immediately and titrate therapy so that the ICP returns back down to normotensive levels. Since some of the patients' health is severely compromised, data collection can also be frequently interrupted for clinical interventions to prevent sustained periods of intracranial hypertension. Thus, a large fraction of the data collected from patients in neurocritical care usually has either a limited range of ICP, or has several discontinuities. This poses a challenge in quantifying the robustness of a noninvasive ICP estimation technique over the clinically relevant range of elevated ICP, or over long periods of time to assess temporal stability of the noninvasive ICP estimates.

Another limitation of the clinical validation of our noninvasive ICP estimation algorithm is the use of radial ABP as an input to our model. The lumped-parameter model described earlier aims to capture the dynamics of a major cerebrovascular territory, and hence requires the measurement of ABP and CBFV from a site close to the cerebral vasculature. While CBFV is routinely and noninvasively measured ultrasonically from the MCA of patients, ABP is clinically measured only at a peripheral arterial site. As a result, none of the clinically recorded data included ABP measured centrally or from a site near the Circle of Willis. This discrepancy in the site of measuring ABP is partially compensated by means of the hydrostatic correction factor between the vertical heights of the two pressure transducer locations. However, this hydrostatic correction factor only alters the DC component of the ABP and does not account for any potential morphological variations between the ABP waveforms at the radial artery and at the MCA. Thus a more robust assessment of our algorithm's performance ideally requires the measurement of ABP from a central site or a site closer to the cerebral vasculature, which can be performed easily in an appropriately chosen animal experimental model.

These are fundamental limitations of human neurological data and made it difficult for us to assess the performance of our spectral noninvasive ICP estimation approach above an ICP of 20 mmHg. This motivated the use of an animal model, where the ICP can be "dialed in" to a desired level and the physiological response can then be studied. There are multiple methods to achieve this goal including direct alteration of the ICP, altering the hemodynamic state or altering the respiratory state of the animal. A swine model was chosen due to the similar cardiovascular and cerebrovascular anatomies in pigs and humans. Pigs also have comparable vital signs and range of normal physiological and cerebrospinal parameters to humans, while also being sufficiently large to allow for easier surgical access and hemodynamic manipulations. Porcine models have also routinely been used in past studies for ischemic stroke models [95–99], monitoring of ICP and monitoring of cerebrovascular autoregulation [100–108].

Thus, we aimed to develop a stable, reproducible experimental protocol to alter the cerebrovascular and hemodynamic states in a Yorkshire swine model, and study the physiological response of the animal, primarily through the recording of high resolution CBFV and central and peripheral ABP signals. The rich waveform data recorded during these experiments can then be analyzed to validate the robustness of our noninvasive ICP estimation method over a wide range of cerebrospinal pressure conditions, and to potentially quantify and understand the dynamics involved in cerebrovascular autoregulation.

5.2 Preparatory work

5.2.1 Anatomical challenges in porcine model

While similar to human cerebrovascular anatomy in many aspects, pigs also pose challenges in neurosurgery, specifically because of their extremely thick cranium and comparatively small brain and ventricular space [107]. Swine skulls are four to six times thicker than a human skull making it difficult to place a ventricular catheter using standard human neurosurgical approaches. The standard procedure for measuring ICP in humans involves drilling a burr hole in the skull and blindly advancing a catheter into the lateral ventricles of the brain or placing a pressure transducer in the intraparenchymal space, through the burr hole [12, 36, 109]. However, both these approaches are difficult to perform in pigs due to their thick skull. Moreover, the anatomical landmarks on the skull for drilling the burr hole is well known in humans but not well defined in a pig.

Another challenge posed by the thick calvarium is the difficulty in obtaining a strong ultrasound signal from one of the major cerebral arteries. Most humans have good temporal acoustic windows that can be used to ultrasonically insonate the MCA. However, the lack of these windows in pigs and the attenuation of ultrasound due to bone make it difficult to reliably insonate the MCA on a consistent basis through the skull [110]. Hence it is difficult to transcranially obtain a strong CBFV signal, which is one of the primary inputs for the spectral noninvasive ICP estimation algorithm described in Chapter 3.

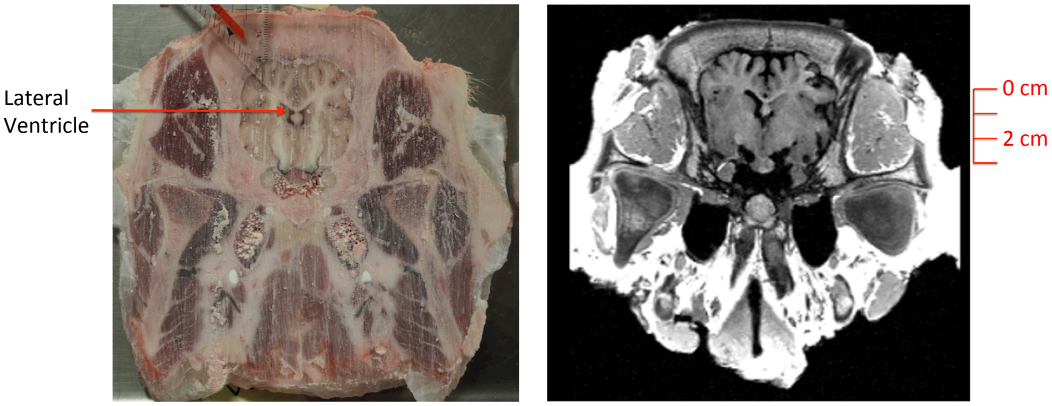

(a) Coronal Slice

(b) MRI Slice

Figure 5-1: Location of the lateral ventricles in two harvested pig heads, one sliced using a bandsaw, and the other digitally reconstructed using MRI.

5.2.2 Pre-experimental explorations

In order to quantify the scale of the previously outlined challenges and refine details of the final experimental protocol, extensive preparatory work was carried out on pig heads harvested from freshly euthanized pigs, approved under a Tissue Harvest Protocol by the MIT Committee on Animal Care. One of the harvested heads was frozen at −70 degrees for two weeks, and then sliced coronally with support from staff at Cummings School of Veterinary Medicine, Tufts University, Grafton, MA. Upon inspection of the coronal slices, a better understanding of the intracranial anatomy, thickness of the skull and location of the ventricles with respect to anatomical landmarks was obtained. Figure 5-1a shows one such coronal slice with the caudal aspects of the lateral ventricles clearly visible, along with the thick cranium and tough temporalis muscle. The thickness of the swine skull was found to be around 20 mm, which agreed with past estimates [107], while a human skull is typically no more than 6 mm thick. An MRI reconstruction of another harvested head was generated to confirm the approximate anatomical location of the ventricular space, as shown in Figure 5-1b. A key observation from the MRI was that the external auditory canal is below the level of the lateral ventricles, and hence would not serve as a good external anatomical landmark for the approximate height of the ventricular space. Hence, these explorations confirmed the need for a craniectomy to access the ventricles and record CBFV transdurally in an accurate and reproducible manner.

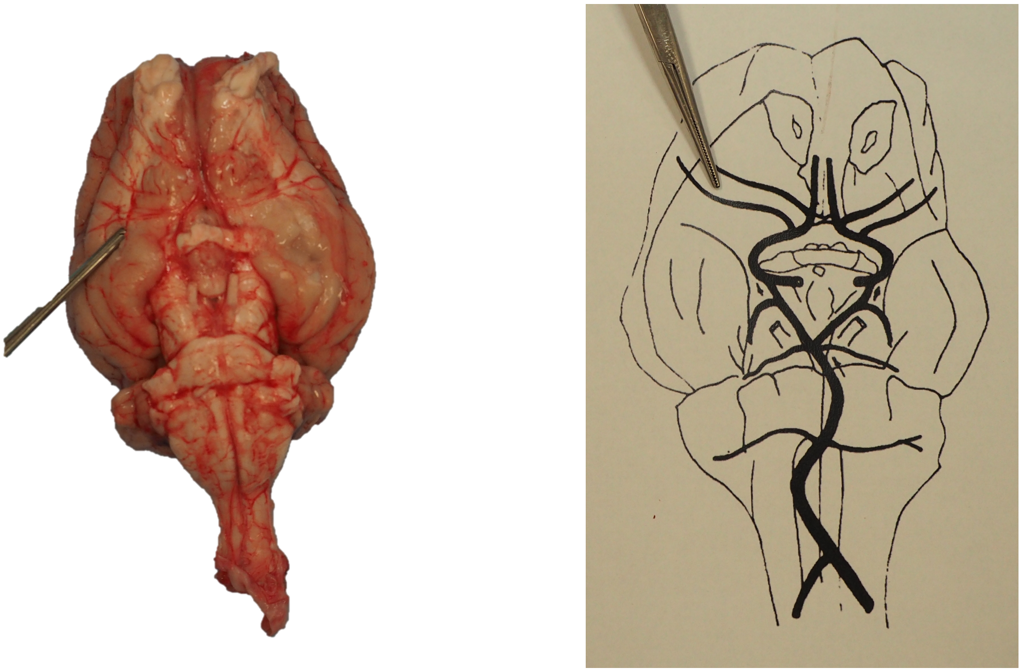

Figure 5-2: Comparison of swine cerebrovascular anatomy observed experimentally (*left*) to the anatomy reported in literature (*right*) [10]. The hemostats in each figure point to one of the right MCAs.

Once a better understanding of the swine ventricular anatomy was obtained by carefully inspecting the coronal slices, several mock craniectomies were performed on additional freshly harvested heads to study the cerebrovascular anatomy, both with the brain in the intracranial space and with the brain extracted. A study of the base of the extracted brain indicated that the anatomy of the cerebral vasculature was very similar to that of humans, with a prominent Circle of Willis and major cerebral vessels arising from it. This was in agreement with past studies of the porcine cerebrovascular anatomy as seen in Figure 5-2. The major difference between a porcine model and the human anatomy was the presence of paired MCAs on either side in a pig, rather than a single MCA on either side for humans [10].

5.3 Experimental protocol

The extensive preparatory work described earlier gave us an understanding of the anatomical challenges posed by a swine model and the location of the pig's cerebrospinal ventricular system relative to surface landmarks. Building on this work and knowledge, an experimental protocol was submitted and approved by MIT's Committee on Animal Care.

5.3.1 Specific aims

The experimental protocol approved by the Committee on Animal Care, allowed for surgical procedures and interventions to be performed on anesthetized female Yorkshire pigs, to achieve the following specific aims:

- To collect invasively measured ICP, ABP and noninvasive CBFV waveform data under a wide range of hemodynamic and cerebrospinal pressure conditions, in a predetermined manner, to validate our spectral noninvasive ICP estimation approach.
- To collect peripheral and central ABP waveforms, to better understand the sensitivity of our algorithm's performance to the site of ABP measurement.

5.3.2 Anesthesia protocol

Prior to each experiment, the animals were fasted overnight. On the day of the experiment, they were sedated with an intramuscular injection of 5 mg/kg telazol (tiletamine and zolazepam), 2 mg/kg xylazine and 0.04 mg/kg atropine. Once intravenous (IV) access was obtained percutaneously through an ear vein, endotracheal intubation was performed using a 7-0 endotracheal tube. Anesthesia was maintained using isoflurane (2-3% in oxygen maintenance concentration). The animals were placed on continuous IV fluid support (physiological saline), at a rate of 5 ml/kg/hr, adjusted for any blood loss, for the duration of the experiment. The animals were mechanically ventilated (DRE Veterinary AV-800 or Hallowell EMC Model 2000) in the controlled-volume setting with a tidal volume of 10 to 15 ml/kg and a respiratory rate set to around 20 breaths per minute. Heated surgical tables and blankets were used to maintain a stable core body temperature. At the end of the experiment, the animals were euthanized with an IV injection of 390 mg/ml sodium pentobarbital.

5.3.3 Instrumentation

The animals were initially placed supine and instrumented for vital sign measurement and hemodynamic monitoring. Surface ECG leads were placed on the limbs in the standard three-lead configuration (left arm, right arm and left leg) to monitor cardiac electrical activity. The tip of the ear or the inside of the lower jaw was used to monitor blood oxygenation levels using a standard optical photoplethysmograph (PPG) sensor. Core body temperature was measured by inserting a temperature probe into the esophagus. Sidestream capnography was used to measure $EtCO_2$ and respiratory rate. The femoral arteries were cannulated bilaterally under ultrasound guidance, and ABP was typically measured continuously from both sides, using standard fluid-filled catheters. One of the femoral veins was also cannulated under ultrasound guidance for direct large-vessel IV access. The carotid artery was cannulated via surgical cut down to expose the carotid sheath. A 2F Mikro-Tip catheter (Millar Instruments) was threaded approximately 5 cm into the carotid artery towards the heart to continuously record a high-fidelity carotid ABP signal. Urine output was monitored by placement of a 12 F urinary catheter via a cystotomy. The ECG, PPG, temperature, capnogram, and one femoral ABP signal were displayed on a Cardell VetTrends V monitor for continuous surveillance of the animal's vital signs.

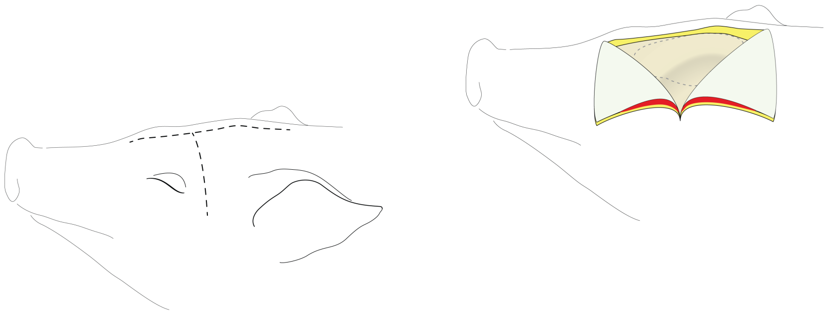

(a) Shaved head of the prone animal with midline and planning line perpendicular to the midline marked for incisions.

(b) The temporalis muscle is removed and the temporal zygoma is exposed. The shaded region represents the original location of the excavated temporalis muscle.

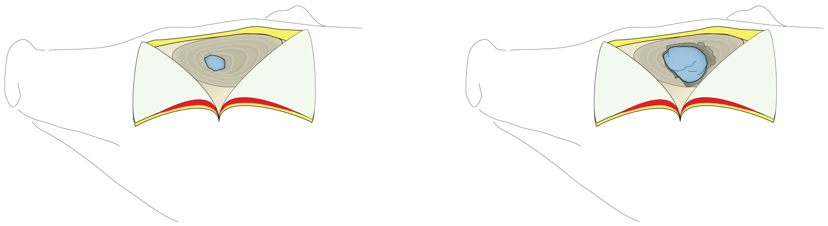

(c) After burring down on the calvarium, a small window of the brain covered by the intact dura (marked in blue) is exposed.

(d) A larger portion of the dura-covered brain, until the Sylvian fissure, is exposed by removing the lateral sphenoid and pterion using a Kerrison punch and rongeurs.

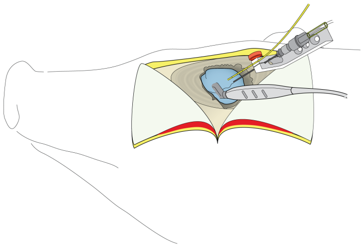

(e) A 4 MHz ultrasound probe is used to insonate the MCA trans-durally, and two ICP transducers - an intraventricular (black needle) and intra parenchymal one (yellow wire) - are inserted in the intracranial space.

Figure 5-3: Steps involved in craniectomy procedure to expose the dura-covered brain, and instrument the intracranial space. Note that the procedure is performed with the animal's head held in place by a custom designed stereotaxic frame. Image courtesy of Ken Pierce, MIT.

5.3.4 Craniectomy

Following induction of general anesthesia, intubation, and instrumentation, the animal was placed into the prone position on a warming pad. With the forelimbs flexed at the elbows, shoulders adducted, the head was positioned in a custom designed stereotaxic frame with the neck slightly extended and the orbitomeatal line positioned horizontally. The head was secured in place with snout and ear bars placed in the mouth and external auditory canals, respectively. Adjustments were made to maintain the head in the horizontal position and centered in the head frame. The stereotaxic frame was crucial to stabilize the head of the animal for the craniectomy, to hold the ICP and TCD probes in place, and to measure approximate cranial landmarks.

The frontal, parietal, and temporal scalp were then shaved, and the midline marked in ink. An additional planning line was drawn perpendicular to the midline and extended approximately 8 cm just posterior to the lateral canthus on the operative side (Figure 5-3a). A 10-blade was then used to incise the scalp along the midline and laterally to expose the temporalis fascia. Raney clips were placed along the incision edges as needed to maintain hemostasis. Small perforating towel clamps were placed at the vertices of the scalp flaps, which were reflected antero-inferiorly and postero-inferiorly and held in place with large rubber bands clamped to the nearby head appliance posts in the frame. Using monopolar cautery, the pericranium was dissected and removed from the superior surface of the exposed calvarium and the attachment of the temporalis muscle along the temporal line was incised. The temporalis muscle was then undercut with monopolar cautery and removed in its entirety from the temporal fossa using rongeurs. In this fashion the temporal zygoma is exposed which establishes the approximate superior-inferior level of the floor of the middle intracranial fossa (Figure 5-3b).

A handheld powered drill with a 9 mm steel acorn cutting burr was used at high speed to thin (< 1mm) the frontal, parietal and temporal calvarium. Using Kerrison rongeurs the inner cortex of calvarium was then removed slowly and carefully to expose the underlying and intact dura mater (Figure 5-3c). A double action, thin-point rongeur was then used to remove the lateral sphenoid and pterion and expose the dural fold overlying the Sylvian fissure (Figure 5-3d). Small cotton rolls were placed along the edges of the craniectomy in the epidural space to control epidural venous bleeding. The operative field was periodically irrigated with room temperature saline to remove any residual bone dust and blood.

5.3.5 Physiological measurements from the intracranial space

Figure 5-4: Ultrasound image showing the target lateral ventricle in a swine brain for placing an EVD. Note this image was taken transdurally after a craniectomy to expose the dura-covered brain.

Ultrasound imaging (CX-50, Philips Healthcare) was then used to visualize the interhemispheric fissure and the lateral ventricle on the operative side (Figure 5-4). An 18G spinal needle with stylet in place was affixed to an articulated positioning arm, attached to the head frame, and positioned over the parietal dura. The needle angle was adjusted in parallel with the long axis of the ultrasound probe. With the lateral ventricle actively in view, the needle was advanced to make contact with the dura. The dura of the planned puncture site was then coagulated using monopolar cautery, and the needle was slowly advanced under ultrasound guidance into the lateral ventricle. The stylet was removed, and the needle attached to IV extension tubing and a 5 ml syringe filled with saline. A small amount of saline (0.2 cc) was injected, and the lateral ventricle was visualized via ultrasound to confirm needle tip placement in the lateral ventricle and to demonstrate that the ventricular volume expanded upon saline injection. Saline-filled extension tubing was then connected to a saline-primed three-way Luerlock stopcock, a pressure transducer, and a saline bag maintained at body temperature. Using a second spinal needle, a point on the dura 0.5 cm anterior to the ventricular catheter puncture site was perforated. A calibrated 3.5F Millar Mikro-Tip catheter was then placed through this dural puncture site into the parietal brain parenchyma to a depth of 1-1.5 cm and secured in place by attaching it to an arm of the frame. Thus, ICP recordings from both the intraventricular catheter and parenchymal probe were obtained.

A 4 MHz TCD ultrasound probe, connected to the DWL Doppler BoxX (Compumedics, USA), was then positioned over the dural fold overlying the most anterior part of the Sylvian fissure, with generous amounts of ultrasound gel, to insonate the MCA. The probe was adjusted to obtain stable and strong CBFV signals from the MCA and held securely in place by a second articulated fixture from the frame (Figure 5-3e). The operative field was gently irrigated with room temperature saline and inspected for epidural bleeding which, if present, was controlled with cotton rolls, thrombin-soaked gelfoam, and mild pressure. Additional ultrasound gel was gently added in small amounts to obtain a water seal at the parietal dural puncture sites, to ensure an accurate physiological ICP measurement was obtained at all times.

5.3.6 Vertical height measurement of pressure transducers

An important pre-processing step in the noninvasive ICP estimation algorithm is the hydrostatic correction of the ABP waveform, to approximate the ABP at the level of the cerebral vasculature. This requires the accurate measurement of vertical heights of the ABP and ICP transducers, as outlined in Chapter 3. The heights of the femoral ABP transducers could be fixed manually, and these were denoted as h_{fABP} for each animal. The central ABP, on the other hand, was measured by a solid-state Millar catheter, where the pressure transducer was at the tip of the catheter in the blood vessel. Hence, this height could not be adjusted and was approximated based on the height of the insertion point int he neck and the depth of the inserted catheter, measured by clear markings. This height was denoted as h_{cABP}.

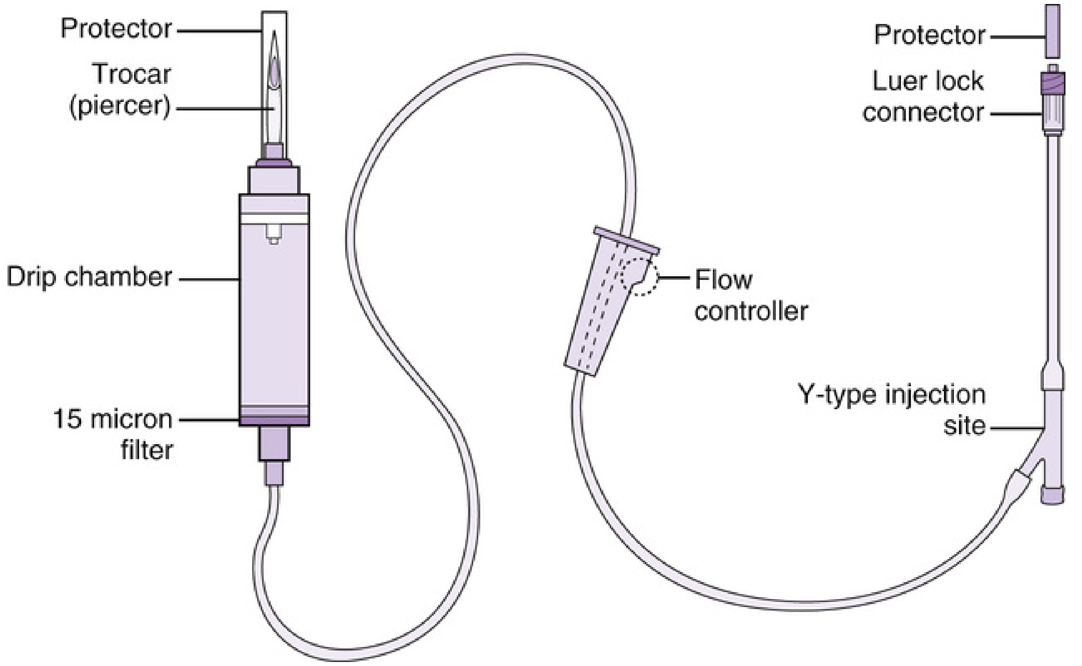

Figure 5-5: Schematic of a typical IV infusion set. The trocar end is used to pierce the bag of fluid to be injected into the patient, while the Luer Lock end is connected to the blood vessel which is to receive the fluid. Image adapted from [11].

The height of the ventricular needle, denoted as h_{EVD}, was estimated in two different ways:

- A simple approach to approximating the vertical height of the ICP ventricular needle was by measuring the depth to which the needle was inserted, via the CX-50 ultrasound device, and accounting for an acute angle of insertion.
- Another approach at estimating the exact height of the ventricular needle relied on the basic principle that flow through a system ceases when the pressure difference across the system is zero. The ventricular needle was connected to a saline bag, through a typical IV infusion setup, a schematic of which is shown in Figure 5-5. Due to pressurization of the drip chamber shown in Figure 5-5, the height at which

flow through the tubing stops is higher than the level of fluid in the chamber itself. This height difference between the level of fluid in the drip chamber, and height of the connector end where flow stops was estimated in tabletop experiments, and denoted as Δh_{flow}. During the experiment, this IV infusion setup was connected to the ventricular needle, with the drip chamber at a height much greater than Δh_{flow} below the ventricles, thus leading to zero flow of saline. The drip chamber was slowly elevated until intraventricular saline flow just started, and the height of the drip chamber at this level was noted a s h_{drip}. Finally, the height of the ventricular needle could be estimated as $h_{EVD} = h_{drip} + \Delta h_{flow}$.

Once the height of the ventricular needle, h_{EVD}, was estimated, the hydrostatic correction factor could be computed in the pre-processing step of the estimation algorithm as outlined in Chapter 3.

5.3.7 ICP manipulations

Elevation of ICP was achieved by direct intraventricular infusion of saline, warmed to body temperature by a SurgiVet Hotline IV fluid warmer, through the intraventricular port described previously. A 1-liter saline bag was mounted on a height-adjustable IV stand and connected to the Luer lock of the intraventricular catheter through a standard IV tubing set (Figure 5-5). Once the hieght of the ventricular needle was estimated, as outlined above, ICP could be manipulated by elevating the drip chamber was elevated above h_{drip}. When this occurs, saline is infused into the ventricles until the inflow into the ventricles matches the outflow through the cerebrospinal fluid pathways, thus establishing a new cerebrospinal fluid pressure.

To control the vertical height of the saline bag, the inner, movable shaft of the IV stand was mechanically coupled to a linear actuator (JoyNano Nema 17) and controlled by a programmable microprocessor (Arduino Uno R3). The actuator consisted of a stepper motor (1.8°/step; 8 mm/360° revolution) connected to the outer shaft and the lead screw connected to the inner, movable shaft of the IV stand. With the stepper motor engaged, the inner shaft of the IV stand, and hence the saline bag, were raised and lowered in a controllable manner.

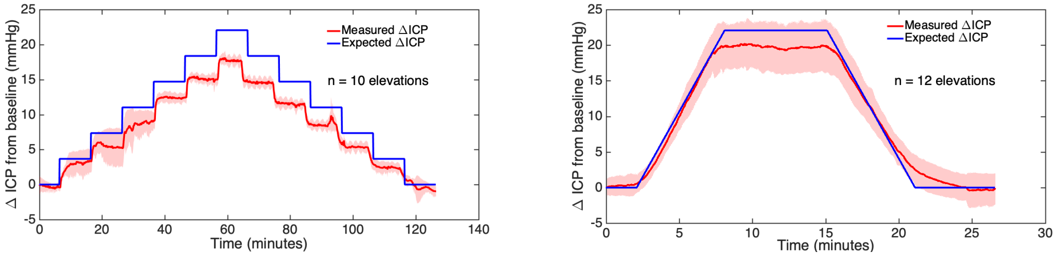

(a) Stepwise elevation of ICP

(b) Plateau wave simulation

Figure 5-6: Two different experimental elevation profiles of mean ICP in porcine model. The red lines and shaded regions represent the mean and standard deviation of the experimentally observed ICP elevations, respectively. The blue line indicates the expected ICP change for the programmed saline bag elevation, computed using the equation $\Delta P = \rho g \Delta h$.

Two elevation/lowering profiles were programmed. The first profile simulated a stepwise increase and decrease of ICP. The saline bag was elevated in steps of 5 cm at a time up to a maximum of 30 cm above baseline ICP; the ICP was allowed to stabilize at each new level for 10 minutes. At the conclusion of the stepwise increase, the saline bag was lowered to baseline again in steps of 5 cm (Figure 5-6a). Each 5 cm change in the vertical height of the saline bag theoretically should have resulted in a change in ICP of approximately 3.7 mmHg. This profile was chosen to probe the important transition zone in ICP from a normal ICP of about 5 to 10 mmHg to a neurosurgical emergency of about 30 to 35 mmHg. The second profile sought to mimic a plateau wave commonly seen in neurotrauma patients [111, 112]. The stepper motor was programmed to elevate the saline bag at a constant speed of 5 cm/min to 30 cm above baseline ICP. The ICP was allowed to equilibrate at the maximum level for 10 minutes before the saline bag was returned to its baseline position, again at constant speed of 5 cm/min (Figure 5-6b).

Figure 5-6 reveals discrepancies between the observed ICP elevations, and the theoretically predicted ones. These can be attributed to the cerebrovascular control system, which is not modeled in our simplified computation of the expected ICP elevation. $\Delta P = \rho g \Delta h$. In reality, every elevation of the saline bag results in an immediate flow of fluid into the ventricular space, which quickly redistributes, and along with the cerebrovascular autoregulatory processes, results in ICP not increasing by the theoretically predicted magnitude.

Finally, to simulate excessively high ICP values, in a subset of the animals the IV stand was disconnected from the stepper motor, and the inner shaft was manually elevated to extreme heights, to achieve a maximum ICP of about 70 mmHg, depending on the prevailing ABP and hemodynamic stability of the animal (Figure 5-7).

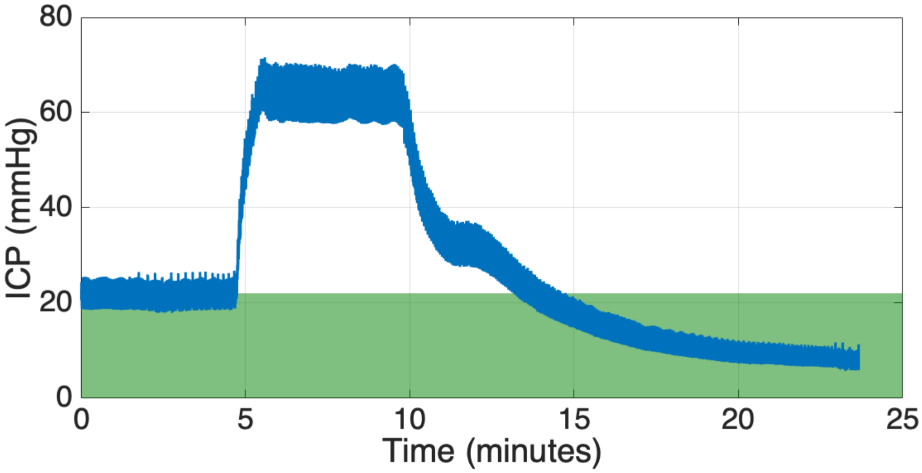

Figure 5-7: Example of manual ICP elevation to extreme levels of intracranial hypertension (ICP=70 mmHg). The shaded region shows the normal range of ICP in humans [12].

5.3.8 Data acquisition

Two ADInstruments eight-channel PowerLab 8/35 data acquisition systems were daisy-chained and used to record data streams from the multiple devices used throughout the experiment. The ECG, PPG, SpO_2, $EtCO_2$, respiratory rate, and one of the femoral ABP measurements were routed through the analog output of the veterinary monitor to the PowerLab for archiving. The other femoral ABP, the ventricular ICP (when transducing), the parenchymal ICP, and the carotid ABP waveforms were directly fed into the PowerLab. The MCA CBFV waveform was measured with the DWL Doppler BoxX, and the analog output was also streamed to the PowerLab for real-time CBFV archiving. All physiological waveforms were calibrated before the experiment and recorded on a common time axis, at a sampling rate of 1,000 samples/s and at an amplitude resolution of 16 bits. The heights of the femoral ABP transducers were adjusted to the same vertical level as the ICP transducer to eliminate any hydrostatic offsets. Once all the instrumentation was complete, stable baseline data were collected for an hour.

Chapter 6

Estimation Results on Porcine Model Cohort

The experimental porcine model described in the previous chapter enabled the titration of ICP in a predetermined manner over a wide range of cerebrospinal states, and resulted in the recording of a rich dataset of high resolution waveform data to validate the accuracy and robustness of our noninvasive ICP estimation algorithm. In this chapter, we begin by summarizing the experimental results of our porcine model and presenting a census of the porcine model validation data, with a much wider range than the previously described patient cohorts. We then present the validation results of our spectral noninvasive ICP estimates on this porcine model dataset, by comprehensively quantifying the estimation performance at varying degrees of clinical accuracy. We detail three main degrees of error quantification – classification of elevated ICP, capturing trends in ICP, absolute accuracy of mean ICP – and demonstrate the accuracy and robustness of our estimates across a wide range of ICP and across all these three metrics. Finally, we detail the significance of our estimation results, by comparing to errors reported in literature for the invasive ICP probes and for past attempts at noninvasive ICP estimation.

6.1 Experimental porcine model summary

6.1.1 Experimental statistics

The experimental protocol detailed in Chapter 5 resulted in a rich collection of high-resolution physiological waveform data, over a wide range of ICP and hemodynamic states. A total of 12 female Yorkshire pigs were studied over a two-year period, with the animals weighing between 41 and 52 kg. In each experiment, the surgical procedures for hemodynamic instrumentation and the craniectomy lasted for an average of six hours and 39 minutes, with the duration significantly reduced after the first few animals. All experiments were successful from a surgical standpoint, with no adverse outcomes or premature deaths. However, there were still some experimental challenges faced over the course of the twelve experiments. One of these was the shivering of some animals when the ICP was elevated and/or returned back to baseline levels. This was observed in four of the animals and spontaneously resolved in all cases. Additionally, in one of the animals, a femoral artery catheter became partially dislodged during the surgery, leading to bleeding and hypovolemic shock for a short while. The animal was stabilized by closing the site of the bleed and restoring intravascular volume. All the other animals had no surgical issues.

6.1.2 Porcine model data census

The porcine model described in the previous chapter was implemented on twelve pigs, with eleven of the pigs have two invasive ICP probes. For all validation purposes, only the parenchymal ICP was used as the gold-standard to compare our estimates against, since the intraventricular ICP was not transducing during ICP manipulations by intraventricular saline infusion. Nine of the pigs had reliable central ABP measurements since in the first three pigs, the Millar Mikro-tip catheter was placed with the tip facing the rostral end of the animal, resulting in a damped cABP signal. In the remaining pigs, the transducer tip was placed facing the blood flow (i.e. threaded towards the heart), which resulted in accurate cABP waveform measurements. Eleven of the pigs had a reliable fABP waveform, as in the first pig the fABP was streamed out of the Cardell veterinary monitor, which heavily quantizes the waveforms.

The basic criteria for inclusion of the recorded data form an experiment in our validation dataset, was the presence of high-resolution ABP (fABP and cABP whenever possible), CBFV and parenchymal ICP waveform data for long stretches of time. Out of all twelve animals studied, the data collected from four pigs were excluded due to the following reasons:

> **Pig 1:** The parenchymal ICP was not measured in this pig, and as a result during intraventricular saline infusion, there was no gold-standard invasive ICP reference recording. Additionally, the femoral ABP was quantized by the veterinary monitor.
>
> **Pig 3:** The animal was not stable for the majority of the experiment and no continuous stretch of stable CBFV recordings were obtained.
>
> **Pig 5:** The intraventricular needle was not in the ventricular space. This resulted in erroneous ICP readings, and potential parenchymal damage.
>
> **Pig 8:** The animal had a bleed due to a dislodged femoral arterial catheter, as described earlier. As a result, the animal was unstable and had to be sustained on vasopressors, which made it difficult to isolate the effects of intraventricular infusion on ICP.

All the data from the eight remaining pigs were screened by the automated pre-processing pipeline used for the patient cohorts [9], and additionally manually reviewed to ensure only contiguous stretches of stable recordings were used for validation of our noninvasive ICP estimation algorithm. This resulted in around 35 hours of data selected from the eight pigs, with a mean ICP of 17.6 mmHg and a range of mean ICP from 2.1 mmHg to 78.2 mmHg. This porcine validation dataset was much larger, in terms of duration, than the patient cohort (around eight and a half hours) and had a much wider range than the patient cohorts (1.3 mmHg to 24.8 mmHg). Moreover the distribution of ICP was more spread out in the porcine model dataset (Figure 6-1), with a significant fraction of data recorded in the clinically relevant elevated ICP range (ICP>22 mmHg [13]).

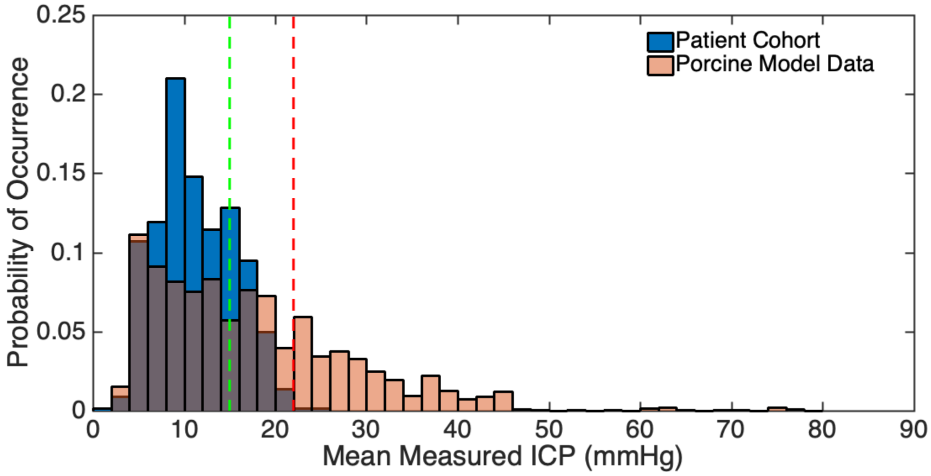

Figure 6-1: Comparison of distributions of mean ICP in human and porcine model validation dataset. The normotensive range of ICP is from 0 mmHg to 15 mmHg (*green*), and the region of intracranial hypertension which necessitates intervention is for mean ICP above 22 mmHg (*red*) [13]. The larger fraction of data available in the pathological higher ICP ranges in the porcine model data, when compared tot he narrow distribution of ICP in the human data, enables a more robust quantification of the algorithm's performance.

6.2 Spectral algorithm implementation in porcine model

The spectral noninvasive ICP estimation algorithm described in Chapter 3 was applied without any major changes to the porcine model dataset. The estimation was performed on a windowed basis using non-overlapping windows of duration 60 beats. A single linear fit was used to reconstruct the mean-subtracted CPP instead of the combination of a linear and cubic fit. This was done because the combination of two different fits has the potential for introducing high-frequency artifacts at the point of concatenation of the reconstructed CPP upstroke and diastolic decays. Hence, a more reduced implementation using a single linear fit was adopted, with no re-training of the parameters on the porcine data. Thus, the linear fitting parameter was still obtained on the same training set as the patient cohorts, and the porcine model data served as a blinded hold-out validation dataset. Finally, as in the patient cohorts, four harmonics in the power spectra over two sub-windows were calculated for the least squares estimation.

An important pre-processing step is the hydrostatic correction of the mean peripheral or central ABP, to approximate the mean cerebral ABP. The height of the intraventricular trasnducer (h_{EVD}), fABP transducer (h_{fABP}) and cABP transducer (h_{cABP}) were determined as described in Chapter 5. However, to ensure physiological accuracy of this hydrostatic correction factor, the compensation was calculated based on the cutoff of cerebral blood flow. As shown in the model in Chapter 3, the cerebral blood flow is driven by CPP, and hence whenever ICP exceeds ABP, CPP goes to zero, the blood vessel completely collapses, and the blood flow (and hence CBFV) is zero. Each of the eight pigs included in the validation dataset had at least one continuous time period where the diastolic CBFV was zero during ICP manipulations. Hence, during this time the diastolic ICP must have exceeded the diastolic cerebral ABP, resulting in flow limitation. Thus, to compute the exact hydrostatic correction, the first time point where diastolic CBFV were zero during ICP elevation was computed, and the difference between the diastolic ICP and ABP were computed at this point, denoted by ΔP_{dias}. After confirming that this value of ΔP_{dias} was consistent across all such periods of diastolic CBFV cutoff within each animal, ΔP_{dias} can be assumed to be the physiologically correct pressure correction factor and applied to the fABP and cABP waveforms to obtain the approximate cerebral ABP.

6.3 Porcine model estimation performance

The spectral algorithm for noninvasive ICP estimation was implemented on around 35 hours of porcine model data, as detailed in the previous section. When compared to the patient validation cohort, the porcine data had more significant trends in ICP as a result of the manipulations described in the previous chapter, and a wider distribution of mean ICP, specifically resulting in a larger fraction of data in the clinically relevant intracranial hypertension region (Figure 6-1). Hence, the porcine model data served as a richer validation dataset for a more comprehensive quantification of the accuracy and robustness of the noninvasive ICP estimation algorithm than the patient cohorts.

While 35 hours of validation data from eight pigs were available with high-quality fABP waveform data, the cABP validation dataset consisted of 33 hours 30 minutes of data from seven pigs. This was due to the lack of a cABP recording in one of the eight included pigs. Henceforth, all estimation results shall be presented for estimates obtained from (fABP, CBFV) as input waveforms and (cABP, CBFV) as input waveforms independently. Since the porcine model validation dataset was very rich and diverse, a comprehensive quantification of the algorithm's performance could be performed at multiple levels of granularity

1. **Intracranial hypertension classification:** Accurate classification of the cerebrospinal state of the patient as normotension or intracranial hypertension is crucial for clinical decision-making and guiding treatment.
2. **ICP trend analysis:** Capturing trends of increasing or decreasing ICP in an accurate and timely manner is essential in detecting episodes of elevated ICP early and to assess response to treatment.
3. **Overall absolute accuracy:** Clinically, accurate estimation of absolute mean ICP is important so clinicians can assess the CSF space in real-time and titrate therapy accordingly to specific target values. Additionally, for each individual animal, a comparison of the mean ICP and noninvasive ICP estimates over time quantifies the tracking of our estimates over a wide range of hemodynamic states and simulated ICP profiles.

6.3.1 Performance in classification of intracranial hypertension

Classification setup

One of the most important applications of accurate noninvasive ICP estimates is early triage for assessment of elevated ICP in potentially neurologically compromised patients. In the current clinical setup, mildly symptomatic patients with potentially elevated ICP are assessed based on their mental state, as measuring ICP invasively is not recommended unless the symptoms are severe. However, the lack of an altered mental state does not necessarily imply that the ICP is normal, and hence there is the potential for missed cases of elevated ICP due to the invasiveness of the measurement modality. A noninvasive ICP modality would allow for this detection of elevated ICP or intracranial hypertension to be performed easily at home or in an ambulance, without the need for neurosurgical expertise, thus enabling better treatment decisions and enabling more favorable outcomes in the case of aggressive intracranial hypertension. Hence, quantifying the performance of our ICP estimation algorithm in accurately classifying intracranial hypertension is clinically vital. This assessment was not possible on the clinical patient cohorts, due to limited range of ICP with almost no data in the intracranial hypertension range. However, due to the richness and wide range of the porcine model dataset, the classification performance of the spectral noninvasive ICP estimation algorithm could be quantified using Receiver Operating Characteristic (ROC) curves.

For assessing the classification performance of our noninvasive ICP estimates on the porcine model data, we defined the two classes as

- **Intracranial Hypertension:** Measured ICP > ICP_{th} (positive class)
- **Normotension:** Measured ICP < ICP_{th} (negative class)

where ICP_{th} is a threshold chosen as the upper limit of normal measured ICP. We then computed the performance of our estimates in correctly classifying the invasive parenchymal ICP into these two classes by picking a threshold for nICP (nICP_{th}) and computing the sensitivity and specificity at this threshold. Varying nICP_{th} over the range of values resulted in a ROC curve. This was done separately for the estimates obtained from the femoral and central ABP as inputs. Furthermore, we computed the sensitivity and specificity of our estimates' classification performance at two operating points:

- **Operating point 1** (nICP_{th} = ICP_{th})**:** Clinically, computing the sensitivity and specificity at ICP_{th} is important as it is the threshold between normal ICP and potentially needing treatment or continuous monitoring. Hence, ICP_{th} was chosen as one of the operating points.
- **Operating point 2** (nICP_{th} = point of equal sensitivity and specificity) **:** Choosing the point of equal sensitivity and specificity as an operating point enables us to calculate the exact probability of correct classification, independent of the prevalence of the positive or negative classes in a cohort. At all the other points on the ROC, the probability of correctly classifying intracranial hypertension is biased by

the relative prevalence of the positive and negative classes in the validation data. The independence of the performance estimate at this operating point on the data makes it useful for practical implementation of the classifier. The computations underlying the choice of this operating point are shown below:

At any point on the ROC,

$$\mathcal{P}(CC) = \mathcal{P}(ICH) \cdot \mathcal{P}(CC|ICH) + \mathcal{P}(Normal) \cdot \mathcal{P}(CC|Normal) \tag{6.1}$$

where $\mathcal{P}(CC)$ is the probability of correct classification by the nICP estimates, $\mathcal{P}(ICH)$ is the probability of occurrence of the positive class, or intracranial hypertension, in the dataset, and $\mathcal{P}(Normal)$ is the probability of occurrence of the negative class, or normotension, in the dataset.

Since $\mathcal{P}(CC|ICH)$ = Sensitivity and $\mathcal{P}(CC|Normal)$ = Specificity,

$$\mathcal{P}(CC) = \mathcal{P}(ICH) \cdot \text{Sensitivity} + \mathcal{P}(Normal) \cdot \text{Specificity} \tag{6.2}$$

At the point where both sensitivity and specificity are equal, and the value is denoted as $\mathcal{S}$,

$$\mathcal{P}(CC) = (\mathcal{P}(ICH) + \mathcal{P}(Normal) \cdot \mathcal{S} = \mathcal{S} = \text{Sensitivity} = \text{Specificity} \tag{6.3}$$

since by fundamental laws of probability, all the data must be either in the positive or negative class, and hence $\mathcal{P}(ICH) + \mathcal{P}(Normal) = 1$. Thus, by inspecting the point of equal sensitivity and specificity, we get an estimate of the probability of correct classification ($\mathcal{P}(CC)$), independent of the distribution of the validation data.

Noninvasive ICP estimates' classification performance

Based on the classification problem described previously, ROC curves were constructed for three different choices of the threshold, ICP_{th} = The thresholds of 20 mmHg, 22 mmHg, and 25 mmHg. 20 mmHg and 22 mmHg were chosen as recommended by the

Brain Trauma Foundation guidelines in their 3rd [12] and 4th editions [13], respectively. The threshold of 25 mmHg was chosen as as ICP measurement above 25 mmHg usually necessitates aggressive treatments in neurocritical care [31].

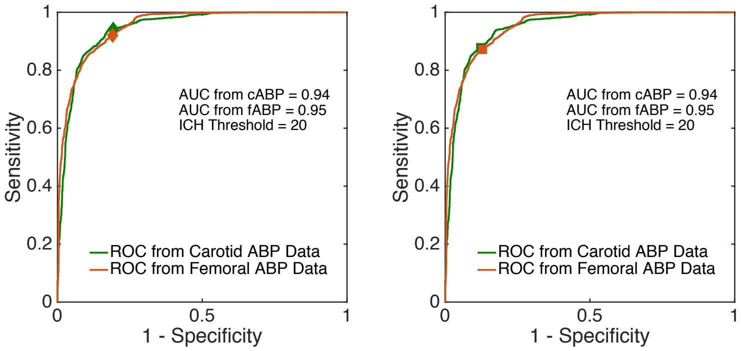

(a) ROC curves for ICP_{th} = 20 mmHg

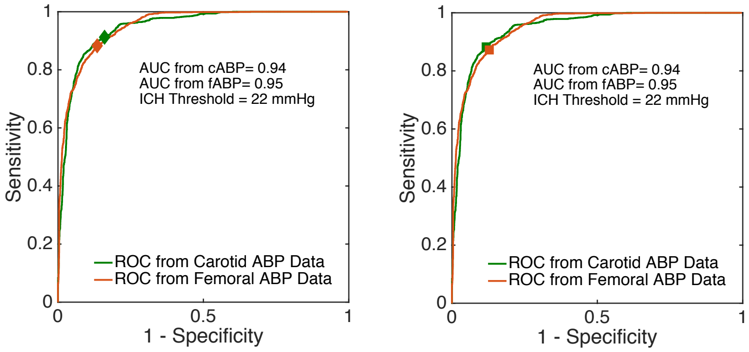

(b) ROC curves for ICP_{th} = 22 mmHg

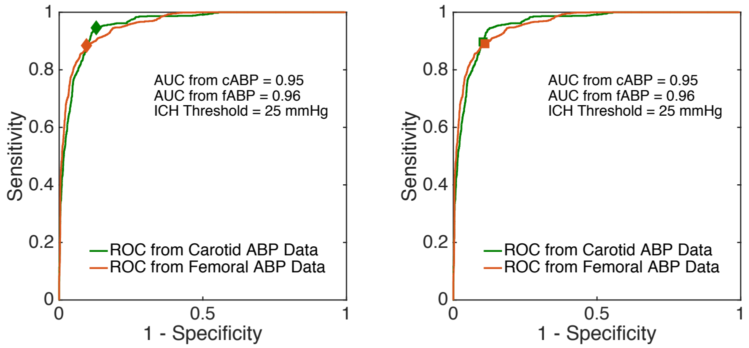

(c) ROC curves for ICP_{th} = 25 mmHg

Figure 6-2: ROC curves along with associated AUC for assessing classification performance for three different thresholds of intracranial hypertension. The left column shows the operating point at ICP_{th}, and the right column shows the operating point at the point of equal sensitivity and specificity. Note that ROC curves were independently generated for estimates obtained from femoral ABP (fABP) and central ABP (cABP).

The ROC curves generated from the noninvasive ICP estimates are shown in Figure 6-2. For each value of ICP$_{th}$, two ROC curves are obtained, one for ICP estimated from fABP, and one for ICP estimated from cABP. For each ROC curve, the area under the curve (AUC) and the sensitivity and specificity at each of the two choices of operating points, described earlier, were computed.

If a peripheral ABP waveform was chosen as the input to our spectral algorithm, the resulting noninvasive ICP estimates had AUCs of 0.95, 0.95 and 0.96 for ICH thresholds of 20, 22 and 25 mmHg, respectively. Similarly, using cABP as an input instead resulted in AUCs of 0.94, 0.94, and 0.95 for ICH thresholds of 20, 22, and 25 mmHg, respectively. The sensitivities and specificities at the two operating points are shown in Table 6.1 for fABP, and in Table 6.2 for cABP.

Table 6.1: Classification performance of estimates obtained from fABP as an input, at both operating points for all three thresholds.

	Operating Point 1			**Operating Point 2**		
ICP$_{\text{th}}$	20 mmHg	22 mmHg	25 mmHg	20 mmHg	22 mmHg	25 mmHg
Sensitivity	0.92	0.88	0.88	0.87	0.87	0.88
Specificity	0.81	0.87	0.91	0.87	0.87	0.88

Table 6.2: Classification performance of estimates obtained from cABP as an input, at both operating points for all three thresholds.

	Operating Point 1			**Operating Point 2**		
ICP$_{\text{th}}$	20 mmHg	22 mmHg	25 mmHg	20 mmHg	22 mmHg	25 mmHg
Sensitivity	0.94	0.91	0.95	0.88	0.88	0.88
Specificity	0.81	0.84	0.87	0.88	0.88	0.88

The ROC curves assess the algorithm's performance in the binary classification problem of intracranial hypertension. However, the transition between a normotensive state and intracranial hypertension does not occur sharply at a fixed threshold value, and hence clinicians look at a transition range between normal ICP and elevated ICP, where the patient is closely monitored. This manifests as different thresholds for normal ICP and elevated ICP. Let us define X as the upper limit of normal ICP (ICP $< X$ indicates normal ICP), and Y as the lower limit of abnormal ICP (ICP $> Y$ indicates elevated ICP). Note that X and Y need not be the same, as defined in the binary ROC classification setup, where $X = Y = \text{ICP}_{th}$. Denoting invasive ICP as ICP, and the noninvasive ICP as nICP, we now define four types of classification errors from these thresholds:

1. $\mathcal{P}_1 = \mathcal{P}(\text{nICP}> Y|\text{ICP}< X)$ = Probability of false alarm or false positive.
2. $\mathcal{P}_2 = \mathcal{P}(\text{nICP}< X|\text{ICP}> Y)$ = Probability of missed clinical event or false negative.
3. $\mathcal{P}_3 = \mathcal{P}(\text{ICP}> Y|\text{nICP}< X)$ = Probability of not giving required treatment.
4. $\mathcal{P}_4 = \mathcal{P}(\text{ICP}< X|\text{nICP}> Y)$ = Probability of over-treatment.

$\mathcal{P}_3$ and $\mathcal{P}_4$ serve as confidence metrics of our estimates, as the clinical goal would be to rely on the noninvasive estimates for accurate information about the patient's ICP, that is not known.

To evaluate the probabilities of mis-classification, X and Y were initially both chosen to be the same (= 20 mmHg) as a stringent threshold between normal and elevated ICP. X and Y were then separated in steps of 2 mmHg symmetrically from 20 mmHg, to compute the errors in a more realistic clinical situation, with a transition range between the normal and elevated ICP zones. The resulting errors are shown in Table 6.3 for estimates obtained from the fABP, and from the cABP.

Table 6.3: Probabilities of errors in classifying normal or elevated ICP

	fABP				cABP			
(X, Y)	$\mathcal{P}_1$	$\mathcal{P}_2$	$\mathcal{P}_3$	$\mathcal{P}_4$	$\mathcal{P}_1$	$\mathcal{P}_2$	$\mathcal{P}_3$	$\mathcal{P}_4$
(20,20)	0.19	0.08	0.05	0.29	0.19	0.06	0.04	0.27
(19,21)	0.11	0.04	0.02	0.17	0.12	0.04	0.03	0.18
(18,22)	0.07	0.01	0.01	0.11	0.09	0.03	0.02	0.13
(17,23)	0.04	0.01	0.01	0.07	0.05	0.02	0.01	0.08
(16,24)	0.02	<0.005	<0.005	0.04	0.02	0.02	0.01	0.04
(15,25)	0.01	<0.005	<0.005	0.01	0.01	0.01	<0.005	0.01

6.3.2 Comparison of trends in ICP and noninvasive ICP

Capturing increasing and decreasing trends in ICP in a timely manner is crucial to prevent adverse outcomes and to evaluate the efficacy of treatment choices. Increasing trends in ICP are usually indicative of worsening neurological health and, coupled with close observation of the patient, might necessitate pharmacological or surgical interventions. Capturing these trends accurately and early on is essential to start any therapeutic intervention immediately to alleviate the patient's health by titrating the ICP back to normotensive levels, and thus prevent any potential neurological damage. Similarly, decreasing trends in ICP are indicative of the patient's health improving, which could be a useful indicator for treatment administered. Monitoring these trends after the start of an intervention could guide further treatment decisions by the neurologist or neurosurgeon, and potentially avoid overtreatment. Hence, while classification of elevated ICP, as described previously, is important for triage purposes, accurately tracking trends in ICP is also important for monitoring the patient's neurological health and treatment efficacy.

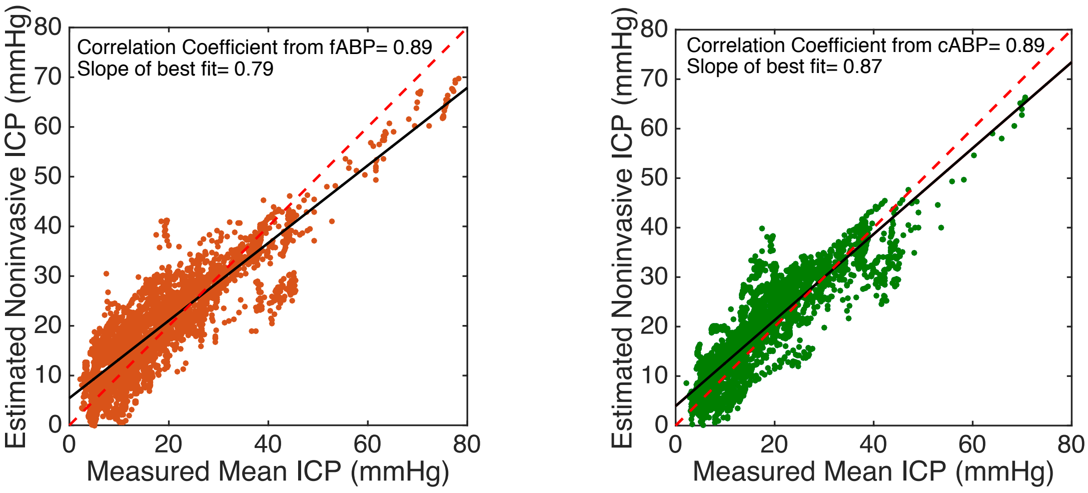

(a) Correlation plot from fABP (b) Correlation plot from cABP

Figure 6-3: Correlation plots between estimated nICP and mean measured ICP. The solid black line indicates the best linear fit for all the data points, while the red dashed line indicates the ideal linear fit, nICP = ICP with slope = 1.

Due to the inherently limited ICP range in the human data, there were no significant observable trends in the ICP, and hence a meaningful trend analysis could not be performed in the clinical patient cohorts. In the porcine model dataset, the correlation plot of the noninvasive ICP estimates and the mean measured ICP is shown in Figure 6-3. The slopes of the best linear fits for correlations between the measured ICP and the estimates obtained from the fABP and the cABP, were 0.79 and 0.87, respectively. For both the correlation plots, the data points seemed to be well represented by this linear fit for the whole range of measured ICP, from 2 mmHg to 78 mmHg, with no significant cloud of outliers.

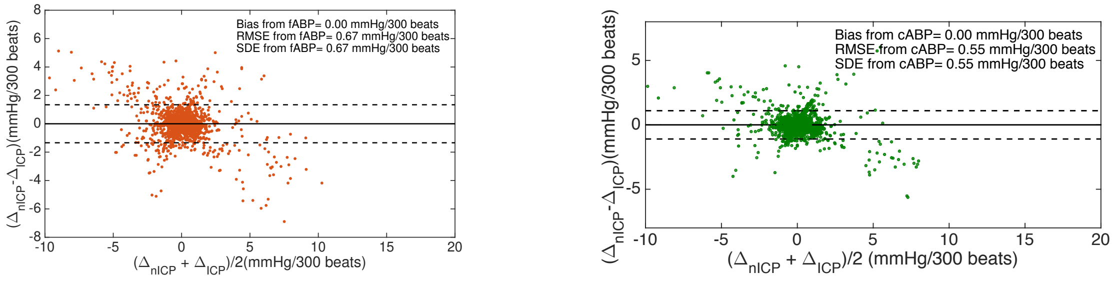

(a) Bland-Altman plot of slopes from fABP

(b) Bland-Altman plot of slopes from cABP

Figure 6-4: Bland -Altman plots comparing the instantaneous slopes of mean measured and estimated ICP over 300 beats. The solid line indicates the bias, while the dotted lines indicate the limits of agreement (bias ± 1.96 · SDE.)

The correlation plot gives information on the degree of co-variation between the measured and estimated ICP, and the degree to which a linear transformation of the estimates captures the variations in measured ICP. While this represents the degree of the estimates tracking the measured ICP to an extent, it does not give information on the absolute errors in comparing the slopes of the measured and estimated ICP values. For this, we computed the instantaneous slope of the estimated and mean measured ICP over non-overlapping windows of 300 beats each, and compared them. The resulting Bland-Altman plot is shown in Figure 6-4.

6.3.3 Evaluation of mean ICP accuracy

The ultimate goal in evaluating the estimation performance is to accurately estimate the mean measured ICP value, in very estimation window. This was quantified using the same error metrics as in the patient validation cohorts, described in Chapter 4. On the porcine model dataset, if fABP was used as the input waveform, the algorithm achieved a bias of 1.6 mmHg, a SDE of 5.2 mmHg, and a RMSE of 5.5 mmHg, on around 35 hours of

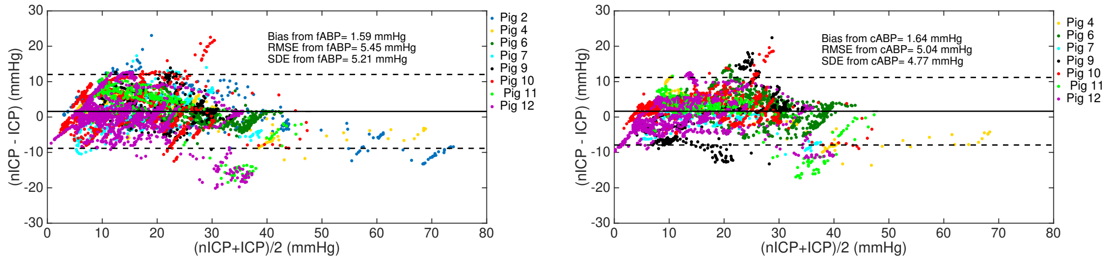

(a) Bland-Altman plot of ICP estimates from fABP (b) Bland-Altman plot of ICP estimates from cABP

Figure 6-5: Bland-Altman plots comparing the mean measured and estimated ICP on a window-by-window basis on all the porcine model data. The solid line indicates the bias, while the dotted lines indicate the limits of agreement (bias ± 1.96 · SDE.)

data from eight pigs (Figure 6-5a). If the cABP waveform was used as the input ABP, the algorithm's bias was 1.6 mmHg, with a SDE of 4.8 mmHg and a RMSE of 5.0 mmHg, on around 33 hours and 30 minutes of data from seven pigs (Figure 6-5b). These results are essentially the same as the estimation results obtained on the overall patient cohorts, where the bias, SDE and RMSE were 0.1 mmHg, 5.1 mmHg and 5.1 mmHg, respectively. To further quantify the performance, the estimation errors were computed for different ranges of measured ICP. For all data points with measured ICP $<$ 15 mmHg, corresponding to a normal range of ICP, the (bias, SDE, RMSE) were (3.1 mmHg, 4.7 mmHg, 5.6 mmHg) for estimates obtained from femoral ABP and (1.9 mmHg, 4.2 mmHg, 4.6 mmHg) for estimates obtained from central ABP. Similarly, if we only consider the data where the ICP ranges from 22 mmHg to 45 mmHg, corresponding to clinically relevant elevated ICP, the (bias, SDE, RMSE) were (-1.2 mmHg, 4.8 mmHg, 4.9 mmHg) for estimates from femoral ABP and (−0.1 mmHg, 4.7 mmHg, 4.7 mmHg for estimates from central ABP. Thus, the performance metrics are consistent across all ranges of the measured ICP.

6.3.4 Temporal ICP tracking in individual animals

All the previous results described the aggregate performance of the estimation algorithm, on the overall dataset. We also investigated the individual estimation performance one each animal, to evaluate the temporal tracking ability of the estimates over various ICP manipulations, and to identify systematic sources of error. These are shown in Figure 6-6.

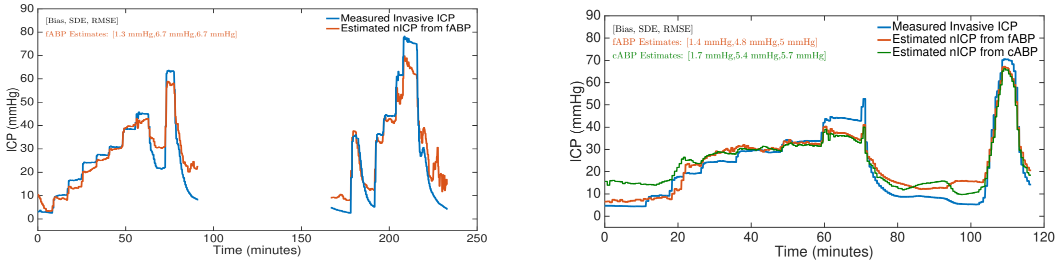

(a) Estimation performance in pig 2 (b) Estimation performance in pig 4

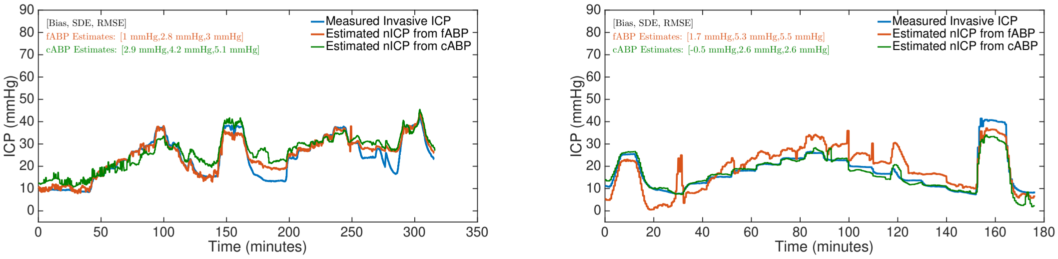

(c) Estimation performance in pig 6 (d) Estimation performance in pig 7

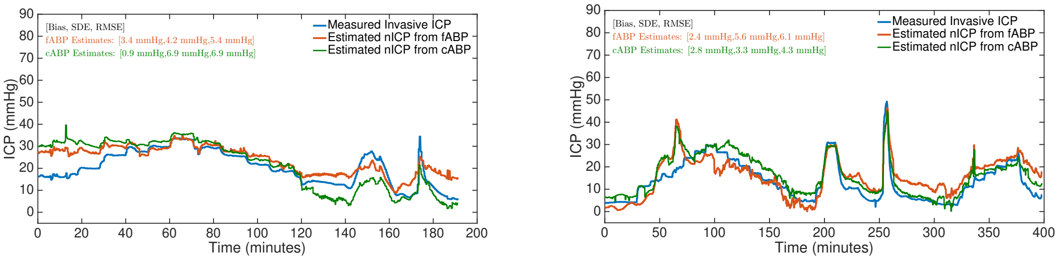

(e) Estimation performance in pig 9 (f) Estimation performance in pig 10

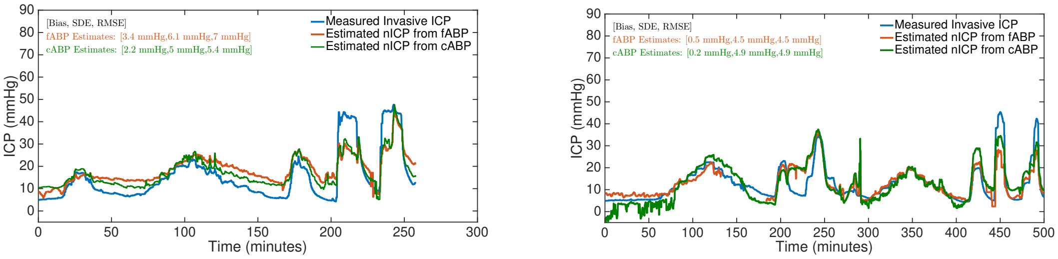

(g) Estimation performance in pig 11 (h) Estimation performance in pig 12

Figure 6-6: Individual estimation performance on each of the animals studied. The bias, SDE and RMSE for each animal are shown in the figures.

6.3.5 Robustness of Noninvasive ICP Estimates

The error metrics on the porcine model dataset, reported in this chapter, are comparable to the error metrics obtained on the pooled patient cohorts, which were reported in Chapter 4 as (0.1 mmHg, 5.1 mmHg, 5.1 mmHg). This validates the robustness of our algorithmic approach since there was no re-training of the algorithm on the porcine model data, and the data acquisition system for all the three cohorts (pediatric, adult and porcine) were all very different and yet the results were consistent across all the data. Moreover, the range of measured ICP in the porcine model data was much wider than the patient cohort with a significant portion of data in the clinically important ICP range of ICP>20 mmHg (Figure 6-1), further validating the algorithm's robustness, by proving the independence of the algorithm's accuracy on the dataset or range of ICP.

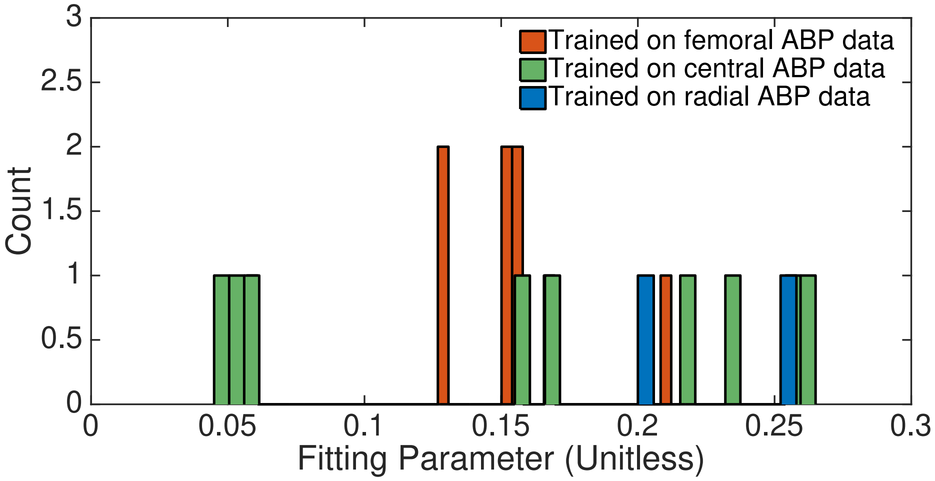

Figure 6-7: Distribution of the linear fitting parameter when trained on individual and overall porcine data, obtained from the femoral and central ABP, and when trained on human data, obtained from the radial ABP.

To further analyze the robustness of the estimates, we derived the fitting parameter for the ABP-ICP linear fit on the whole porcine model data in another training step, and analyzed the training performance on the porcine data. This resulted in an accuracy (bias) of 1.2 mmHg and 0.4 mmHg, a precision (SDE) of 5.2 mmHg and 4.8 mmHg, and a RMSE of 5.4 mmHg and 4.8 mmHg, respectively for nICP estimated from fABP and cABP. These performance metrics are very similar to the ones obtained without recalibrating on the porcine data, and effectively defines a training performance.

Similarly, if the fitting parameter is optimized for each individual pig and tested on each pig, the overall error metrics improve to a (bias, SDE, RMSE) of (0.9 mmHg, 5.1 mmHg, 5.2 mmHg) from the femoral ABP and (0.1 mmHg, 4.5 mmHg, 4.6 mmHg) from the central ABP measurement. These metrics essentially amount to the performance attained by individual calibration of the model to each pig, thus providing a lower bound on the error metrics that can be expected within the current model and algorithmic framework.

The resultant distribution of fitting parameters obtained by training on different datasets is shown in Figure 6-7. Importantly, this exercise demonstrates that the overall results do not improve significantly (<10% improvement) by calibrating individually or training on the overall porcine data. The robustness of our estimation performance to the fitting parameter choice, on the overall porcine data, is summarized in Table 6.4. A similar study of the effect of calibrating the fitting parameter on each pig's individual estimation performance is described in Appendix A.

Table 6.4: Estimation performance on the porcine data with respect to the fitting parameter training scheme.

	fABP errors (mmHg)			**cABP errors (mmHg)**		
Fitting Procedure	**Bias** mmHg	**SDE** mmHg	**RMSE** mmHg	**Bias** mmHg	**SDE** mmHg	**RMSE** mmHg
Single parameter from the clinical training set (*testing performance*)	1.6	5.2	5.5	1.6	4.8	5.0
Single parameter trained on whole porcine data (*training performance*)	1.2	5.2	5.4	0.4	4.8	4.8
Optimal parameter for each animal (*calibrated performance*)	0.9	5.1	5.2	0.1	4.5	4.6

The sensitivity of the error to perturbations of the fitting parameter were also analyzed. A perturbation in the fitting parameter of less than 10% resulted in a RMSE degradation of less than 5%, and a 20% perturbation of the fitting parameter resulted in the RMSE degrading by less than 10%, irrespective of the choice of fitting parameter. Hence, the estimation results do not seem to be critically dependent on the fitting parameter.

6.4 Discussion

The estimation performance of our spectral algorithm for classification of intracranial hypertension, tracking of trends in ICP and for absolute mean ICP estimation, were assessed in terms of errors reported in past noninvasive ICP estimation methods. Past attempts at noninvasive ICP estimation by Fanelli *et al.* [9] and Kashif *et al.* [6] leveraged similar models of cerebrovascular physiology, and obtained AUCs of 0.79 and 0.83 respectively in classifying intracranial hypertension. It is encouraging that our approach resulted in an AUC of 0.94 to 0.96 for different definitions of elevated ICP, and over a wider range of ICP variability in the validation dataset. Expanding the scope of approaches to estimating ICP noninvasively, Robba *et al.* [113] evaluated the classification performance of four different types of algorithms on 100 patients, where they defined elevated ICP as ICP >20 mmHg. They reported an AUC of 0.78 for an approach predicated on estimating the optic nerve sheath diameter (ONSD), an AUC of 0.85 for an algorithm estimating ICP from the pulsatility index (PI) of CBFV, an AUC of 0.86 for ICP estimated purely by a TCD-based approach, and an AUC of 0.71 for estimates based on the neurological pupil index (NPI) measured by pupillometry. Additionally, when utilizing a combination of these techniques, the best AUC they reported was 0.91. For the same classification task and definition of elevated ICP (ICP>20 mmHg), our algorithm resulted in an AUC of 0.94 and 0.95, for different ABP inputs, which are better or comparable to these reported metrics. Andersen *et al.* [114] proposed a method to assess ICP from the optical arteriole-venule diameters, measured using fundus photography, and reported an AUC of 0.74 for classifying elevations in ICP above 20 mmHg, when compared to our AUC of 0.94 and 0.95. Moreover, at their choice of operating point, they reported a sensitivity of 94% and specificity of 50%, which implies a large probability of identifying a healthy individual as sick. The trade-off between sensitivity and specificity also provides a useful qualitative assessment of our classification performance. While an ideal clinical scenario would be perfect prediction of both normotensive and intracranial hypertension cases, such perfect classification does not exist in realistic clinical applications of screening tests. Additionally, it might be more important to accurately classify the sick patients to guide treatment decisions and reduce the chance of adverse outcomes. Table 6.3 shows the four types of probability errors obtained from our algorithm's classification performance. $\mathcal{P}_2$ and $\mathcal{P}_3$ indicate the probability of missed events of intracranial hypertension and the probability of under-treatment, respectively. Clinically, it is vital to minimize these two errors, rather than $\mathcal{P}_1$ and $\mathcal{P}_4$, to potentially save lives. Table 6.3 shows that $\mathcal{P}_2$ and $\mathcal{P}_3$ are less than 8% for all combinations of thresholds. Also, for a clinically acceptable definition of normal ICP as ICP<16 mmHg and elevated ICP as ICP>24 mmHg, these two errors are <0.005%, implying that all episodes of intracranial hypertension are correctly identified.

Correlation analyses have been performed in various past noninvasive ICP estimation approaches, with comparable results to our correlation coefficient of 0.89 [6,35,36,78,113]. The best linear fit for these plots in our porcine model data was shown in Figure 6-3. Imaduddin [78] and Kashif [6] reported correlation coefficients of 0.64 and 0.90, using similar model-based approaches to noninvasive ICP estimation. While the range of measured ICP int he Kashif data was similar to the range in our porcine data, Imaduddin used the pediatric patient data described in Chapter 4 of this thesis, which has an inherently more limited range and hence may have affected the correlation analysis negatively. Robba [113] reported correlation coefficients of 0.54, 0.50, 0.61 and −0.41 for approaches based on ONSD, PI, TCD and NPI, respectively. Park [76] reported a correlation coefficient of 0.75 in assessing ICP from ABP and CBFV, using a state space model-based approach. The correlation plot gives a metric of how well an affine function of the noninvasive ICP estimate approximates the mean invasive ICP, and hence it is highly encouraging that our approach results in better or comparable correlation coefficients to a number of recently reported estimation approaches. However, it is important to note that the correlation coefficient is also a function of the range of measured ICP and is expected to be lower for limited ICP ranges [22, 78]. Additionally, as seen in Figure 6-3, there were no signiifcant outliers in the correlation plots, indicating that the correlation performance of our estimates was good across the whole range of measured ICP.

Our estimation algorithm resulted in a (bias, SDE, RMSE) combination of (1.59 mmHg, 5.21 mmHg, 5.45 mmHg) and (1.64 mmHg, 4.77 mmHg, 5.04 mmHg) for estimates obtained from fABP and cABP, respectively, on the rich porcine model dataset. As described in Chapter 4, it is encouraging that these error metrics are also comparable to the errors reported between the currently accepted gold-standards for invasive ICP monitoring, namely the intraventricular and intraparenchymal modalities [36, 49]. Furthermore, these error metrics are also similar to or better than some of the past noninvasive ICP estimation approaches [6, 9, 66, 76, 78]. Additionally, the estimation performance was analyzed over different ranges of measured ICP and the error metrics were found to be comparable for ICP < 15 mmHg and for ICP in the range of 22 mmHg to 45 mmHg. These comparable metrics indicate the robustness of our estimates and their independence of the range of the underlying ICP.

A systematic source of error observed in all the porcine model data is the underestimation of nICP during regions of intracranial hypertension. These regions correspond to a period of diastolic cutoff, where CBFV goes to zero due to ICP exceeding the ABP. If these regions of diastolic cutoff are excluded, the RMSE improves to 5.0 mmHg for estimates from femoral ABP and 4.3 mmHg for estimates obtained from central ABP. Thus the regions of intracranial hypertension contribute to a consistent source of error, which is explained in the next chapter.

Another advantage of quantifying the estimation performance on the porcine model data, was the ability to independently assess the effect of peripheral or central ABP as an input to the algorithm. While ideally we aimed to measure the cerebral ABP and compute estimates of ICP, the extensive branching of the carotid arteries seen in pigs, and the narrowing of the cerebral vessels, rendered the measuring of cerebral ABP very difficult. Hence the measurement of central ABP served as a better approximation of the cerebral ABP that could be conveniently measured. The consistent AUC, correlation coefficient, and bias, SDE, and RMSE across the estimates obtained from the two ABP waveforms as input, validated the relative independence of the algorithm's performance on the exact choice of measured ABP. This is clinically important, as this analysis proved the sufficiency of a peripheral ABP for optimal estimation performance, as long as the hydrostatic compensation is accurately performed, and since only radial (peripheral) ABP is routinely measured at the bedside.

Chapter 7

Contributions and Future Work

The previous chapters detail our proposed model-based noninvasive ICP estimation framework, particularly as exemplified by our spectral estimation algorithm. The accuracy and robustness of our algorithm's performance were quantified on three diverse validation datasets, in a calibration-free manner. The results were found to be highly encouraging as the error metrics were comparable across all the datasets, as well as comparable to the errors reported for the invasive ICP measurement modalities. In this chapter, we briefly summarize all our contributions, previously detailed in this thesis, and explore some of the residual sensitivities and limitations of our current estimation framework. We then describe the avenues for future work to further refine our estimation performance, as well as detailing the various technological advancements and research directions necessary on a longer time scale, to implement a real-time, fully noninvasive ICP measurement modality at the bedside. Finally, we present our concluding remarks on the clinical problem of noninvasive ICP estimation.

7.1 Summary of Contributions

The previous chapters detail our noninvasive ICP estimation framework and its comprehensive validation. Our overall contributions are briefly summarized as follows:

1. Building upon past attempts, we developed a model-based, calibration-free, patient-specific, spectral approach to noninvasive ICP estimation. Our approach was based

on a simple, computationally and physiologically tractable lumped-parameter circuit model of cerebrovascular physiology, modeling the interplay between ABP, CBFV, and ICP at a major cerebrovascular territory. We implemented a frequency-domain algorithm to estimate mean ICP noninvasively from the ABP and CBFV waveforms in a windowed manner.

2. We designed and deployed a custom data acquisition system at the neuro and trauma ICUs of Boston Medical Center, with the aim of archiving high resolution physiological waveforms from multiple devices, and important ancillary data, at the bedside, on a common time axis. In conjunction with a similar data acquisition system at Boston Children's Hospital, we obtained two clinical datasets from different patient cohorts – pediatric and adult – over a wide range of age and pathologies.

3. Motivated by the inherent limitations of clinical data for neurological validation, primarily the limited range of ICP, we developed a novel experimental porcine model for altering the cerebrospinal pressure state of a pig in a predetermined manner, and observing the physiological and hemodynamic response of the animal by recording high resolution ABP and CBFV waveforms. We demonstrated the ability to reliably and reproducibly manipulate ICP in a pre-programmed elevation profile and recorded a rich porcine validation dataset from twelve pigs. This porcine dataset had a wide range of ICP values, ranging from the normal mean values to those of extreme intracranial hypertension. We were also able to demonstrate significant trends in ICP in this dataset.

4. We validated the estimation performance of our model-based spectral algorithm on the two patient cohorts (pediatric and adult) and on the rich porcine dataset and compared the estimates to the gold-standard invasive ICP recorded simultaneously. Our estimates across all the three datasets were found to be accurate and comparable to the errors reported in literature for the currently accepted clinical invasive ICP measurement. The noninvasive estimation approach's performance was also found to be robust as it was comparable across all three validation cohorts, despite the vast difference in the data collection hardware, the age range of the patients and their clinical

conditions, and the fact that the animal model was designed to challenge the algorithm to estimate ICP at the very extremes of physiology. Owing to the wide range of ICP values in the porcine data, we were able to comprehensively quantify the estimation performance at varying levels of clinical accuracy, and proved the accuracy and robustness of our algorithm when compared to previous attempts at noninvasive ICP estimation reported in literature.

7.2 Future Work

While our noninvasive ICP estimation approach was found to be accurate and robust over a diverse range of patients and animal data, and over a wide range of ICP values, the residual errors and sensitivities in our algorithm's performance can be attributed to limitations that can be further improved upon. These sensitivities can be broadly classified into data-based, model-based, and algorithm-based and are outlined in this section. Even when the noninvasive ICP estimation performance is further refined and validated on a larger patient cohort, realizing the aspiration of implementing a fully noninvasive real-time ICP estimation device at the bedside still faces some challenges. In this section, we also outline the various challenges and suggest research directions necessary to take these noninvasive ICP modalities to the bedside.

7.2.1 Avenues for Improving Estimation Performance

Among all the individual nICP-ICP comparisons with errors greater than 5 mmHg, a significant fraction (around 21%) can be attributed to data-related errors. These are errors primarily comprised of artifacts in the input ABP and CBFV signals due to motion, damping of the ABP signal due to clogging of the catheter, loss of CBFV signal and repositioning of the TCD transducer to relocate the MCA. While the majority of these artifacts are rejected by the signal processing pipeline, some of these are intermittent and account for a noisy or physiologically incorrect signal, resulting in large errors in both the patient and porcine cohorts. Additionally, in the porcine model dataset, there were individual cases where the animal became hemodynamically unstable due to ICP manipulations and had to be stabilized by bolus or continuous infusions of vasopressors and fluids. These pharmacological interventions pose a challenge to our current ICP estimation approach, given that bolus injections tend to be short-lived and hence may induce transient changes in cardiovascular variables that are short compared to the estimation windows assumed here. Future experimentation with shorter window-lengths and constant-rate infusions of a variety of drugs commonly used in neurocritical care will be an important area of exploration. Finally, another potential source of errors arises from the need for accurate estimation of the hydrostatic correction factor. Data-related errors can significantly degrade the estimation performance [9,80] and hence motivated our design of a custom data acquisition system, to carefully control the data recording and isolate the "true" estimation performance of the algorithm. However, some of these data-related errors are physiological responses and hence cannot be accounted for *a priori*. The exact computation of the hydrostatic correction factor needs to be further investigated to design and validate an accurate empirical method of noninvasively calculating the appropriate vertical heights. This is crucial as the nICP estimates are directly affected by this hydrostatic correction factor, as explained in Chapter 3.

Model-based errors primarily arise due to the inability of our simple, lumped-parameter model to capture some of the more intricate intracranial dynamics. While a simpler model like ours has a number of advantages (including computational tractability, physiologically grounded parameters, and not requiring *a priori* knowledge of parameter values), our modeling framework also assumes constant ICP and circuit parameters over each estimation window, thus failing to account for cerebrospinal dynamics occurring on a shorter time scale. This manifests as a consistent negative bias in our estimation performance at high ICP values, where the ICP exceeds the ABP. In this regime, ICP exceeds ABP for a fraction of the beat duration, and results in CBFV getting "cutoff" at zero for a short duration within each beat. However, our model framework would require a negative CBFV or alternatively a negative resistance, R, during these periods to be consistent with the data. If this were true, the mean CBFV required by the model to be consistent with the data during these phases of diastolic cutoff would be lower than the actual measured mean CBFV. Thus, the noninvasive ICP estimates from the measured CBFV are lower than the nICP estimates would be if the non-negativity constraint were met, thus resulting in underestimation of the noninvasive ICP estimates when compared to the invasive measured ICP. Hence, this underestimation can be attributed to a breakdown of the modeling assumptions.

Solving this issue would require modification of the model by potentially introducing a diode or a voltage-gated switch, and re-implementing the algorithmic framework to account for the discontinuities introduced by these non-linear or quasi-linear circuit elements. While past attempts at noninvasive ICP estimation have implemented higher-order models, these models have the disadvantage of requiring *a priori* knowledge of certain parameters, which renders it impossible to estimate ICP in a patient-specific manner. Thus, while modifying the model might solve some of these model-related errors, it is important to be mindful of the trade-off in implementing higher-order models.

Another direction to be undertaken in the future to refine the estimation performance is the incorporation of cerebrovascular autoregulatory dynamics into the estimation framework. The current framework does not account for the complex interplay of the various control mechanisms responsible for maintaining constant perfusion to the brain. Explicit modeling of these control mechanisms might improve the estimation performance, particularly if the assumption of constant cerebrovascular resistance, compliance, and ICP over the duration of an estimation window is violated.

Various approaches at modeling and quantifying the autoregulation have been proposed in the literature, and further explorations of these mechanisms can potentially improve our estimation results and explain some of the errors seen in the validation data, such as the overestimation when ICP returns to a normotensive value from a region of intracranial hypertension.

From an algorithmic perspective, further sensitivity analyses of the sensitivity of the estimation error to the exact power spectral density computation can be performed by perturbing the peak locations and comparing the spectrum to that of the original invasive CPP waveform. Additionally, sensitivities of the error to the last-squares convergence optimization scheme can be studied and a theoretical investigation into the optimization scheme can be undertaken. Finally, a physiological and clinical study can be undertaken to investigate the origin of the empirical ABP-ICP relationship, and its variability with ICP.

7.2.2 Taking these Models to Point of Care

All the previously detailed limitations outline the future steps required to refine the algorithm's performance further and improve upon the already encouraging estimation performance. Once the noninvasive ICP estimation performance is refined, the validation accuracy and robustness needs to be verified on a larger and more diverse patient cohort. In order to achieve this, data collection is ongoing at the two Boston-area hospitals previously described, to further enrich the validation dataset. However, a few technological advancements, listed below, are essential to fully realize the dream of taking these noninvasive ICP measurement modalities to the point of care, each of which spawns an independent research direction.

1. **Operator-independent CBFV Waveforms:** As discussed previously [9,22,78], the nICP estimation results are very sensitive to commonly observed artifacts in the CBFV waveform. Some of these artifacts arise due to the need for a manual operator to locate the vessel, insonate it, and obtain a stable waveform. However, such a setup is prone to motion artifacts and frequent loss of signal, and hence not suitable for long-term CBFV recordings, which is essential for the realization of a real-time noninvasive ICP measurement modality. Hence, there is a need to develop a wearable, self-steering, automated TCD ultrasound device that can lock on to a chosen intracranial blood vessel and insonate it to obtain stable CBFV waveforms over a long duration. There have been attempts reported in the literature of such a device, but their accuracy and clinical translation have not been completely verified [115–117].

2. **Accurate Noninvasive ABP Waveforms:**While our spectral approach to nICP estimation is a significant improvement over the currently accepted invasive approaches in minimizing the risk to the patient, it is not fully noninvasive as the ABP waveform is still obtained invasively from a peripheral arterial site (radial or femoral). The development of an accurate, continuous noninvasive ABP measurement device to record high resolution peripheral ABP waveforms has been an unsolved clinical problem and an active area of research for a long time. The commercially available continuous noninvasive ABP monitors suffer from temporal drift, the need to period-

ically recalibrate or a large bias [118]. Motivated by this unsolved clinical problem, several attempts have been made in the past to achieve a fully noninvasive and accurate measurement of the ABP waveform [119–124]. To date, none of these methods have been found to be sufficiently accurate to replace or complement the existing radial arterial catheters.

3. **Volumetric Cerebral Blood Flow Estimation:**The modeling framework detailed in this thesis utilizes CBFV waveform as an input in lieu of the volumetric CBF, by exploiting the invariance of the model to linear transformations. This was done since CBFV is conveniently measurable by noninvasive ultrasonic means, while there is no clinically accepted method of monitoring volumetric CBF. However, an accurate estimate of volumetric CBF over time would provide additional information on the neurological health of the patient, in addition to the ICP [4,48]. Moreover, the CBF estimate would allow for estimation of the exact resistance and intracranial compliance, which might have clinical significance for predicting episodes of intracranial hypertension [48,51,125,126]. In conjunction with ICP, CBF could also lead to a better understanding and model of the cerebrovascular autoregulation and its dynamics in maintaining constant cerebral perfusion. However, so far, these CBF measurements have been primarily limited to extracranial vessels with intracranial estimation of CBF proving to be inaccurate, due to limited spatial resolution [127–129].

7.3 Conclusion

ICP is an important clinical indicator of neurological injury and is routinely measured in neurocritical care units worldwide. Clinicians rely on ICP for diagnosing, monitoring and guiding treatment decisions in patients presenting with several neurological disorders, each of which imposes a significant clinical burden annually. The currently accepted measurement modalities for ICP are highly invasive and carry several risks to the patient's neurological health, thus limiting ICP measurement to critically ill patients. Hence, there is a pressing need for the development of an accurate noninvasive ICP measurement modality to expand the fraction of patients who could benefit from this cranial vital sign.

Motivated by past attempts at solving this crucial clinical problem, we proposed a model-based spectral approach to estimate ICP noninvasively from ultrasonically recorded CBFV and peripherally measured ABP waveforms in this thesis. In order to clinically validate our algorithmic implementation, we designed and deployed a data acquisition system at the bedside of two Boston area hospitals and recorded two distinct and diverse patient cohorts. Recognizing the inherent limitations of human neurological data, we designed a novel experimental porcine model to record high resolution waveform data over a wide range of ICP states. We then tested our algorithm's performance on these rich and diverse validation datasets, and obtained an accuracy and precision of 0.1 mmHg and 5.1 mmHg on the pooled patient data, and 1.6 mmHg and 5.2 mmHg on the porcine model data, respectively. These error metrics are highly encouraging and were found to be comparable to those reported in literature for past noninvasive ICP estimation attempts and, importantly, for the currently accepted invasive modalities. Finally, we discussed the sources of error in the current framework and the future advancements in research and technology required to clinically implement a noninvasive ICP measurement modality.

Continuous noninvasive monitoring of ICP and neurological health can benefit many people and potentially save a large number of lives. Our contributions, detailed in this thesis, hopefully takes one step (or a giant leap) forward towards realizing the clinical dream of implementing a real-time, calibration-free, patient-specific, accurate, robust, and fully noninvasive ICP measurement modality at the bedside to replace the current invasive modalities, and to better the state of neurological health monitoring and neurocritical care worldwide.

Appendix A

Individual Calibration of Fitting Parameters on Porcine Data

Table A.1: Comparison of estimation performance if fitting parameter (m_{fit}) is calibrated to each pig or chosen in a blinded manner from the pediatric dataset.

	RMSE from fABP (mmHg)		***RMSE from cABP (mmHg)***	
Pig	**Individually Calibrated m_{fit}**	**m_{fit} from Pediatric Data**	**Individually Calibrated m_{fit}**	**m_{fit} from Pediatric Data**
2	6.5 mmHg	6.7 mmHg	N/A	N/A
4	4.7 mmHg	5.0 mmHg	4.7 mmHg	5.7 mmHg
6	2.8 mmHg	3.0 mmHg	4.3 mmHg	5.1 mmHg
7	5.5 mmHg	5.5 mmHg	2.6 mmHg	2.6 mmHg
9	4.4 mmHg	5.4 mmHg	6.9 mmHg	6.9 mmHg
10	5.7 mmHg	6.1 mmHg	3.5 mmHg	4.3 mmHg
11	6.3 mmHg	7.0 mmHg	4.8 mmHg	5.4 mmHg
12	4.5 mmHg	4.5 mmHg	4.9 mmHg	4.9 mmHg
Overall Porcine Data	5.2 mmHg	5.5 mmHg	4.6 mmHg	5.0 mmHg

The estimation results presented in Chapter 6 are highly encouraging as they demonstrate the accuracy of our approach on a wide range of measured ICP. Additionally, as described in Chapter 6, the estimation performance was found to be insensitive to the exact choice of fitting parameter, with no appreciable degradation in performance when the fitting parameter was perturbed by 5% or 10%. To further test the independence of the estimation results to the fitting parameter, m_{fit}, we obtained the optimal fitting parameter for each individual animal in the porcine model by allowing ourselves access to the invasive ICP data. We then used this calibrated fitting parameter to obtain the optimal estimation performance for each individual pig. The resulting RMSE are summarized for each individual pig in Table A.1. As seen in the table, the RMSE are comparable for the individually calibrated m_{fit} and for the choice of m_{fit} from the pediatric data. This a strong indicator of the robustness of our algorithm as the individually calibrated estimation performance requires access to the invasive ICP, while the performance metrics using the m_{fit} chosen from the training subset of the pediatric data were obtained in a blinded manner. Hence, our calibration-free approach is insensitive to the choice of fitting parameter. Moreover, the comparable performances were found to be true for each individual pig, for the overall porcine data, and for estimates obtained from fABP and cABP, further proving the robustness of our approach.

Bibliography

[1] A. Ropper, M. Samuels, J. Klein, and S. Prasad, *Adams and Victor's Principles of Neurology*, 11th ed. Mcgraw Hill, 2019.

[2] K. Flemming and L. Jones, *Mayo Clinic Neurology Board Review*. Mayo Clinic Scientific Press, 2015.

[3] T. Langfitt, J. Weinstein, and N. Kassell, "Cerebral vasomotor paralysis produced by intracranial hypertension." *Neurology*, vol. 15, pp. 622–641, 1965.

[4] T. Heldt, T. Zoerle, D. Teichmann, and N. Stocchetti, "Intracranial pressure and intracranial elastance monitoring in neurocritical care." *Annual Reviews in Biomedical Engineering*, vol. 21, pp. 1–27, 2019.

[5] M. Lyons and F. Meyer, "Cerebrospinal fluid physiology and management of increased intracranial pressure." *Mayo Clinic Proceedings*, vol. 65, pp. 684–707, 1990.

[6] F. Kashif, G. Verghese, V. Novak, M. Czosnyka, and T. Heldt, "Model-based noninvasive estimation of intracranial pressure from cerebral blood flow velocity and arterial pressure." *Science Translational Medicine*, vol. 4, pp. 129–144, 2012.

[7] J. Noraky, G. Verghese, D. Searls, V. Lioutas, S. Sonni, A. Thomas, and T. Heldt, "Noninvasive intracranial pressure determination in patients with subarachnoid hemorrhage." *Acta Neurochirurgica Supplement*, vol. 122, pp. 65–68, 2016.

[8] (2018) Mayfield Brain and Spine: Traumatic Brain Injury (TBI). Accessed May 2021. [Online]. Available: http://mayfieldclinic.com/pe-tbi.htm

[9] A. Fanelli, F. Vonberg, K. LaRovere, B. Walsh, E. Smith, S. Robinson, R. Tasker, and T. Heldt, "Fully automated, real-time, calibration-free, noninvasive intracranial pressure estimation." *Journal of Neurosurgery Pediatrics*, vol. 24, pp. 509–519, 2019.

[10] R. Fankhauser, H. Luginbühl, and J. Mcgrath, "Cerebrovascular disease in various animal species." *Annals New York Academy of Sciences*, vol. 127, pp. 817–860, 1965.

[11] E. Jamieson, J. McCall, and L. Whyte, *Clinical Nursing Practices*, 4th ed. Edinburgh: Churchill Livingstone, 2002.

[12] P. Kochanek, R. Tasker, N. Carney, A. Totten, P. Adelson, N. Selden, C. Davis-O'Reilly, E. Hart, M. Bell, S. Bratton, G. Grant, N. Kissoon, K. Reuter-Rice, M. Vavilala, and M. Wainwright, "Guidelines for the management of pediatric severe Traumatic Brain Injury, third edition: Update of the Brain Trauma Foundation guidelines," *Pediatric Critical Care Medicine*, vol. 20 (3S Suppl 1), pp. S1–S82, 2019.

[13] N. Carney, A. Totten, C. O'Reilly, J. Ullman, G. Hawryluk, M. Bell, S. Bratton, R. Chestnut, O. Harris, N.Kissoon, A. Rubiano, L. Shutter, R. Tasker, M. Vavilala, J.Wilberger, D. Wright, and J. Ghajar, "Guidelines for the management of severe Traumatic Brain Injury, fourth edition." *Neurosurgery*, vol. 80, pp. 6–15, 2017.

[14] C. Gooch, E. Pracht, and A. Borenstein, "The burden of neurological disease in the United States: A summary report and call to action." *Annals of Neurology*, vol. 81, pp. 479–484, 2017.

[15] Global Burden of Disease (GBD) 2016 Neurology Collaborators, "Global, regional, and national burden of neurological disorders, 1990-2016: A systematic analysis for the Global Burden of Disease study 2016." *Lancet Neurology*, vol. 18, pp. 459–480, 2019.

[16] C. Taylor, J. Bell, M. Breiding, and L. Xu, "Traumatic brain injury-related emergency department visits, hospitalizations, and deaths — United States, 2007 and 2013." *Morbidity and Mortality Weekly Reports (MMWR) Surveillance Summary*, vol. 66, pp. 1–16, 2017.

[17] M. Faul, L. Xu, M. Wald, and V. Coronado, "Traumatic brain injury in the United States: Emergency department visits, hospitalizations and deaths 2002-2006." *Atlanta (GA): Centers for Disease Control and Prevention, National Center for Injury Prevention and Control*, 2010.

[18] E. Benjamin *et al.*, "Heart disease and stroke statistics - 2018 update: A report from the American Heart Association." *Circulation*, vol. 137, pp. 67–492, 2018.

[19] S. Virani *et al.*, "Heart disease and stroke statistics 2020 update: A report from the american heart association." *Circulation*, vol. 141, pp. 139–596, 2020.

[20] R. Snow, C. Guerra, A. Noor, H. Myint, and S. Hay, "The global distribution of clinical episodes of plasmodium falciparum malaria." *Nature*, vol. 434, pp. 214–217, 2005.

[21] J. Chin, "Tuberculous meningitis." *Neurology Clinical Practice*, vol. 4, pp. 199–205, 2014.

[22] R. Jaishankar, A. Fanelli, A. Filippidis, T. Vu, J. Holsapple, and T. Heldt, "A spectral approach to noninvasive intracranial pressure estimation." *IEEE Journal of Biomedical and Health Informatics*, vol. 24, pp. 2398–2406, 2020.

[23] E. Kandel, J. Schwartz, and T. Jessell, *Principles of Neural Science*, 4th ed. New York: Mcgraw Hill, 2000.

[24] J. Hall, *Guyton and Hall textbook of medical physiology*. Saunders-Elsevier, 2011.

[25] D. Bruce, "Cerebrospinal fluid pressure and brain metabolism." in *Neurobiology of Cerebrospinal Fluid*, J. Wood, Ed., 1980, vol. 1, pp. 351–357.

[26] A. Khasawneh, R. Garling, and C. Harris, "Cerebrospinal fluid circulation: What do we know and how do we know it?." *Brain Circulation*, vol. 4, pp. 14–18, 2018.

[27] C. Hawthorne and I. Piper, "Monitoring of intracranial pressure in patients with traumatic brain injury." *Frontiers in Neurology*, vol. 5, p. 121, 2014.

[28] C. Avezaat, J. van Eijndhoven, and D. Wyper, "Cerebrospinal fluid pulse pressure and intracranial volume-pressure relationships." *Journal of Neurology, Neurosurgery and Psychiatry*, vol. 42, pp. 687–700, 1979.

[29] A.Monro, *Observations on the Structure and Functions of the Nervous System: Illustrated with Tables.* Edinburgh: Creech Johnson, 1783.

[30] B. Mokri, "The Monro-Kellie hypothesis: Applications in CSF volume depletion." *Neurology*, vol. 56, pp. 1746–1748, 2001.

[31] L. Steiner and P. Andrews, "Monitoring the injured brain: ICP and CBF," *British Journal of Anesthesia*, vol. 97, pp. 26–38, 2006.

[32] F. Walters, "Intracranial pressure and cerebral blood flow." *Update in Anesthesia, Physiology*, vol. 8, pp. 18–23, 1998.

[33] M. Treggiari, N. Schutz, N. Yanez, and J. Romand, "Role of intracranial pressure values and patterns in predicting outcome in traumatic brain injury: A systematic review." *Neurocritical Care*, vol. 6, pp. 104–112, 2007.

[34] J. Miller, D. Becker, J. Ward, H. Sullivan, W. Adams, and M. Rosner, "Significance of intracranial hypertension in severe head injury." *Journal of Neurosurgery*, vol. 47, pp. 503–516, 1977.

[35] X. Zhang, J. Medow, B. Iskandar, F. Wang, M. Shokoueinejad, J. Koueik, and J. Webster, "Invasive and noninvasive means of measuring intracranial pressure: A review." *Physiological Measurement*, vol. 38, pp. 143–182, 2017.

[36] L. Zacchetti, S. Magnoni, F. Corte, E. Zanier, and N. Stocchetti, "Accuracy of intracranial pressure monitoring: A systematic review and meta-analysis." *Critical Care*, vol. 19, p. 420, 2015.

[37] M. Morgalla, L. Krasznai, K. Dietz, H. Mettenleiter, M. Deininger, and E. Grote, "Methods of experimental and clinical assessment of the relative measurement accuracy of an intracranial pressure transducer." *Journal of Neurosurgery*, vol. 95, pp. 529–532, 2001.

[38] J. Miller, "Inaccurate pressure readings for subarachnoid bolts." *Neurosurgery*, vol. 19, pp. 253–255, 1986.

[39] P. Barlow, A. Mendelow, A. Lawrence, M. Barlow, and J. Rowan, "Clinical evaluation of two methods of subdural pressure monitoring." *Journal of Neurosurgery*, vol. 63, pp. 578–582, 1985.

[40] U. Kakarla, L. Kim, S. Chang, N. Theodore, and R. Spetzler, "Safety and accuracy of bedside external ventricular drain placement." *Operative Neurosurgery*, vol. 63, pp. 162–166, 2008.

[41] H. Fried, B. Nathan, A. Rowe, J. Zabramski, N. Andaluz, A. Bhimraj, M. Guancu, D. Seder, and J. Singh, "The insertion and management of external ventricular drains: An evidence-based consensus statement." *Neurocritical Care*, vol. 24, pp. 64–81, 2016.

[42] F. Ortolano, M. Carbonara, A. Stanco, V. Civelli, G. Carrabba, T. Zoerle, and N. Stocchetti, "External ventricular drain causes brain tissue damage: An imaging study." *Acta Neurochirurgica*, vol. 159, pp. 1981–1989, 2017.

[43] J. Champey, C. Mourey, G. Francony, P. Pavese, E. Gay, L. Gergele, R. Manet, L. Velly, N. Bruder, and J. Payen, "Strategies to reduce external ventricular drain-related infections: A multicenter retrospective study." *Journal of Neurosurgery*, vol. 130, pp. 2034–2039, 2018.

[44] A. Jamjoom, A. Joannides, M. Poon, A. Chari, M. Zaben, M. Abdulla, J. Roach, L. Glancz, A. Solth, J. Duddy, P. Brennan, R. Bayston, D. Bulters, C. Mallucci, M. Jenkinson, W. Gray, J. Kandasamy, P. Hutchinson, A. Kolias, and A. A. on behalf of the British Neurosurgical Trainee Research Collaborative, "Prospective, multicentre study of external ventricular drainage-related infections in the UK and Ireland." *Journal of Neurology, Neurosurgery and Psychiatry*, vol. 89, pp. 120–126, 2018.

[45] A. Saladino, J. White, E. Wijdicks, and G. Lanzino, "Malplacement of ventricular catheters by neurosurgeons: A single institution experience." *Neurocritical care*, vol. 10, p. 248, 2009.

[46] D. Bauer, S. Razdan, A. Bartolucci, and J. Markert, "Meta-analysis of hemorrhagic complications from ventriculostomy placement by neurosurgeons." *Neurosurgery*, vol. 69, pp. 255–260, 2011.

[47] S. Tavakoli, G. Peitz, W. Ares, S. Hafeez, and R. Gandhi, "Complications of invasive intracranial pressure monitoring devices in neurocritical care." *Neurosurgical Focus*, vol. 43, p. e6, 2017.

[48] K. Evensen and P. Eide, "Measuring intracranial pressure by invasive, less invasive or non-invasive means: Limitations and avenues for improvement." *Fluids and Barriers of the CNS*, vol. 17, p. 34, 2020.

[49] T. Lescot, V. Reina, Y. Manach, F. Boroli, D. Chauvet, A. Boch, and L. Puybasset, "In vivo accuracy of two intraparenchymal intracranial pressure monitors." *Intensive Care Medicine*, vol. 37, pp. 875–879, 2011.

[50] A. Brean, P. Eide, and A. Stubhaug, "Comparison of intracranial pressure measured simultaneously within the brain parenchyma and cerebral ventricles." *Journal of Clinical Monitoring and Computing*, vol. 20, pp. 411–414, 2006.

[51] P. Eide, "Demonstration of uneven distribution of intracranial pulsatility in hydrocephalus patients." *Journal of Neurosurgery*, vol. 109, pp. 912–917, 2008.

[52] F. Sina, S. Razmeh, N. Habibzadeh, A. Zavari, and M. Nabovvati, "Migraine headache in patients with idiopathic intracranial hypertension." *Neurology International*, vol. 9, p. 7280, 2017.

[53] R. Simone, A. Ranieri, S. Montella, P. Cappabianca, M. Quarantelli, F. Esposito, G. Cardillo, and V. Bonavita, "Intracranial pressure in unresponsive chronic migraine." *Journal of Neurology*, vol. 261, pp. 1365–1373, 2014.

[54] R. Hayward, J. Britto, D. Dunaway, and O. Jeelani, "Connecting raised intracranial pressure and cognitive delay in craniosynostosis: Many assumptions, little evidence," *Journal of Neurosurgery Pediatrics*, vol. 18, pp. 242–250, 2016.

[55] A. Ragauskas, G. Daubaris, A. Dziugys, V. Azelis, and V. Gedrimas, "Innovative noninvasive method for absolute intracranial pressure measurement without calibration." *Acta Neurochirurgica Supplement*, vol. 95, pp. 357–361, 2005.

[56] L. Padayachy, R. Brekken, G. Fieggen, and T. Selbekk, "Noninvasive transorbital assessment of the optic nerve sheath in children: Relationship between optic nerve sheath diameter, deformability index and intracranial pressure." *Operative Neurosurgery*, vol. 16, pp. 726–733, 2018.

[57] A. Koziarz, N. Sne, F. Kegel, S. Nath, J. Badhiwala, F. Nassiri, A. Mansouri, K. Yang, Q. Zhou, T. Rice, and S. Faidi, "Bedside optic nerve ultrasonography for diagnosing increased intracranial pressure." *Annals of Inetrnal Medicine*, vol. 171, pp. 896–905, 2019.

[58] V. Rajajee, M. Vanaman, J. Fletcher, and T. Jacobs, "Optic nerve ultrasound for the detection of raised intracranial pressure," *Neurocritical Care*, vol. 15, pp. 506–515, 2011.

[59] A. Levinsky, S. Papyan, G. Weinberg, T. Stadheim, and P. Eide, "Noninvasive estimation of static and pulsatile intracranial pressure from transcranial acoustic signals." *Medical Engineering and Physics*, vol. 38, pp. 477–484, 2016.

[60] V. Bollela, G. Frigieri, F. Vilar, D. S. Jr., F. Tallarico, G. Tallarico, R. Andrade, T. de Haes, O. Takayanagui, A. Catai, and S. Mascarenhas, "Noninvasive intracranial pressure monitoring for HIV-associated cryptococcal meningitis." *Brazilian Journal of Medical and Biological Research*, vol. 50, p. 6392, 2017.

[61] D. Popovic, M. Khoo, and S. Lee, "Noninvasive monitoring of intracranial pressure." *Recent Patents in Biomedical Engineering*, vol. 2, pp. 165–179, 2009.

[62] P. Raboel, J. Bartek, M. Andresen, B. Bellander, and B. Romner, “Intracranial pressure monitoring: Invasive versus noninvasive methods – a review.” *Critical Care Research and Practice*, p. 950393, 2012.

[63] B. Schmidt, J. Klingelhöfer, J. Schwarze, D. Sander, and I. Wittich, “Noninvasive prediction of intracranial pressure curves using transcranial Doppler ultrasonography and blood pressure curves.” *Stroke*, vol. 28, pp. 2465–2472, 1997.

[64] P. Xu, M. Kasprowicz, M. Bergsneider, and X. Hu, “Improved noninvasive intracranial pressure assessment with nonlinear kernel regression.” *IEEE Transactions on Information Technology in Biomedicine*, vol. 14, pp. 971–978, 2010.

[65] M. Chacon, C. Pardo, C. Puppo, M. Curilem, and J. Landerretche, “Noninvasive intracranial pressure estimation using support vector machine,” *Proceedings of the IEEE Engineering in Medicine and Biology Society*, vol. 2010, pp. 996–999, 2010.

[66] J. Wang, X. Hu, and S. Shadden, “Data-augmented modeling of intracranial pressure.” *Annals of Biomedical Engineering*, vol. 47, pp. 714–730, 2019.

[67] X. Hu, V. Nenov, M. Bergsneider, and N. Martin, “A data mining framework of noninvasive intracranial pressure assessment.” *Biomedical Signal Processing and Control*, vol. 1, pp. 64–77, 2006.

[68] F. Scalzo, S. Asgari, S. Kim, M. Bergsneider, and X. Hu, “Bayesian tracking of intracranial pressure signal morphology.” *Artificial Intelligence in Medicine*, vol. 54, pp. 115–123, 2012.

[69] F. Scalzo, R. Hamilton, S. Asgari, S. Kim, and X. Hu, “Intracranial hypertension prediction using extremely randomized decision trees.” *Medical Engineering and Physics*, vol. 34, pp. 1058–1065, 2012.

[70] X. Hu, V. Nenov, M. Bergsneider, T. Glenn, P. Vespa, and N. Martin, “Estimation of hidden state variables of the intracranial system using constrained nonlinear Kalman filters,” *IEEE Transactions on Biomedical Engineering*, vol. 54, pp. 597–610, 2007.

[71] J. Stroh, T. Bennett, V. Kheyfets, and D. Albers, “Clinical decision support for traumatic brain injury: Identifying a framework for practical model-based intracranial pressure estimation at multihour timescales.” *Journal of Medical Informatics*, vol. 9, p. 23215, 2021.

[72] M. Ursino and C. Lodi, “A simple mathematical model of the interaction between intracranial pressure and cerebral hemodynamics.” *Journal of Applied Physiology*, vol. 82, pp. 1256–1269, 1997.

[73] A. Linninger, M. Xenos, B. Sweetman, S. Ponkshe, X. Guo, and R. Penn, “A mathematical model of blood, cerebrospinal fluid and brain dynamics.” *Journal of Mathematical Biology*, vol. 59, pp. 729–759, 2009.

[74] P. Rashidinejad, X. Hu, and S. Russell, “Patient-adaptable intracranial pressure morphology analysis using a probabilistic model-based approach.” *Physiological Measurement*, vol. 41, p. 104003, 2020.

[75] Y. Erol, S. Russell, A. Sivaganesan, and G. Manley, “Combined state and parameter estimation of human intracranial hemodynamics.” *Proceedings of the 26th Annual Conference on Neural Information Processing Systems (NeurIPS) – Workshop on Machine Learning for Clinical Data Analysis and Healthcare*, 2013.

[76] C. Park, S. Ryu, B. Jeong, S. Lee, C. Hong, Y. Kim, and B. Lee, “Real-time noninvasive intracranial state estimation using unscented Kalman filter,” *IEEE Transactions on Neural Systems and Rehabilitation Engineering*, vol. 27, no. 9, pp. 1931–1938, 2019.

[77] F. Kashif, T. Heldt, and G. Verghese, “Model-based estimation of intracranial pressure and cerebrovascular autoregulation.” *Computing in Cardiology*, vol. 35, pp. 369–372, 2008.

[78] S. Imaduddin, A. Fanelli, F. Vonberg, R. Tasker, and T. Heldt, “Pseudo-bayesian approach to model-based noninvasive intracranial pressure estimation and tracking,” *IEEE Transactions on Biomedical Engineering*, vol. 67, no. 6, pp. 1604–1615, 2020.

[79] A. Fanelli and T. Heldt, “Signal quality quantification and waveform reconstruction of arterial blood pressure recordings.” *Proceedings of IEEE Engineering in Medicine and Biology Society*, vol. 2014, pp. 2233–2236, 2014.

[80] J. Noraky, “A spectral approach to noninvasive model-based estimation of intracranial pressure,” M. Eng. thesis, Massachusetts Institute of Technology, 2014.

[81] R. Jaishankar, “A spectral approach for noninvasive estimation of intracranial pressure,” S. M. thesis, Massachusetts Institute of Technology, 2017.

[82] F. Kashif, T. Heldt, and G. Verghese, “Systems, devices and methods for noninvasive or minimally-invasive estimation of intracranial pressure and cerebrovascular autoregulation,” U.S. Patent 8 366 627B2, February 05, 2013.

[83] J. P. Holt, “The collapse factor in the measurement of venous pressure: The flow of fluid through collapsible tubes.” *American Journal of Physiology*, vol. 134, pp. 292–299, 1941.

[84] A. Oppenheim, A. Willsky, and S. Nawab, *Signals and Systems*, 2nd ed. Upper Saddle River, New Jersey: Prentice Hall, 1997.

[85] E. Bering Jr., “Choroid plexus and arterial pulsation of cerebrospinal fluid,” *A.M.A Archives of Neurology and Psychiatry*, vol. 73, pp. 165–172, 1955.

[86] R. Adolph, H. Fukusumi, and N. Fowler, “Origin of cerebrospinal fluid pulsations,” *American Journal of Physiology*, vol. 212, pp. 840–846, 1967.

[87] H. Hinghofer-Szalkay, T. Kenner, H. Leopold, and H. Holzer, “Die Anwendung der Biegeschwingermethode zur Messung von Blutdichte und Hämatokrit.” *Klinische Wochenschrift*, vol. 57, pp. 1163–1167, 1979.

[88] A. Fanelli, R. Jaishankar, A. Filippidis, J. Holsapple, and T. Heldt, “A waveform archiving system for the GE Solar 8000i bedside monitor.” *Acta Neurochirurgica Supplement*, vol. 126, pp. 173–177, 2018.

[89] M. Yang, Z. Yang, T. Yuan, W. Feng, and P. Wang, “A systemic review of functional near-infrared spectroscopy for stroke: Current application and future directions.” *Frontiers in Neurology*, vol. 10, p. 58, 2019.

[90] “Patient Data Module (PDM): Service manual.” *GE Medical Systems Information Technologies*.

[91] “Tram–RAC 4A housing service manual,” *GE Medical Systems Information Technologies*, 2017.

[92] J. Bland and D. Altman, “Statistical methods for assessing agreement between two methods of clinical measurement.” *Lancet*, vol. 1, pp. 307–310, 1986.

[93] M. Cnossen, J. Huijben, M. van der Jagt, V. Volovici, T. van Essen, S. Polinder, D. Nelson, A. Ercole, N. Stocchetti, G. Citerio, W. Peul, A. Maas, D. Menon, E. Steyerberg, and H. Lingsma, “Variation in monitoring and treatment policies for intracranial hypertension in traumatic brain injury: A survey in 66 neurotrauma centers participating in the CENTER-TBI study.” *Critical Care Medicine*, vol. 21, p. 233, 2017.

[94] E. Cardoso, J. Rowan, and S. Galbraith, “Analysis of the cerebrospinal fluid pulse wave in intracranial pressure.” *Journal of Neurosurgery*, vol. 59, pp. 817–821, 1983.

[95] B. Allen, Y. Ko, G. Buckberg, S. Sakhai, and Z. Tan, “Studies of isolated global brain ischaemia: 1. A new large animal model of global brain ischaemia and its baseline perfusion studies.” *European Journal of Cardio-Thoracic Surgery*, vol. 41, pp. 1138–1146, 2012.

[96] B. Allen, Y. Ko, G. Buckberg, S. Sakhai, and Z. Tan, “Studies of isolated global brain ischaemia: 2. Controlled reperfusion provides complete neurologic recovery following 30 min of warm ischaemia – the importance of perfusion pressure.” *European Journal of Cardio-Thoracic Surgery*, vol. 41, pp. 1147–1154, 2012.

[97] B. Allen, Y. Ko, G. Buckberg, S. Sakhai, and Z. Tan, “Studies of isolated global brain ischaemia: 3. Influence of pulsatile flow during cerebral perfusion and its link to consistent full neurological recovery with controlled reperfusion flowing 30 min of global brain ischaemia.” *European Journal of Cardio-Thoracic Surgery*, vol. 41, pp. 1155–1163, 2012.

[98] F. Arikan, T. Martínez-Valverde, S. Guerrero, M. Campos, M. Esteves, D. Gandara, R. Torné, L. Castro, A. Dalmau, J. Tibau, and J. Sahuquillo, "Malignant infarction of the Middle Cerebral Artery in a porcine model. a pilot study." *PLOS ONE*, vol. 12, p. e0172637, 2017.

[99] S. Mangla, J. Choi, F. Barone, C. Novotney, J. Libien, E. Lin, and J. Pile-Spellman, "Endovascular external carotid artery occlusion for brain selective targeting: A cerebrovascular swine model." *BMC Research Notes*, vol. 8, p. 808, 2015.

[100] M. Janda, J. Bajorat, O. Simanski, G. Noldge-Schomburg, R. Hofmockel, and M. Schütze, "A surgical technique for a terminal intracranial hypertension model in pigs." *Laboratory Animals*, vol. 46, pp. 258–260, 2012.

[101] E. Muench, P. Horn, C. Bauhuf, H. Roth, M. Philipps, P. Hermann, M. Quintel, P. Schmiedek, and P. Vajkoczy, "Effects of hypervolemia and hypertension on regional cerebral blood flow, intracranial pressure, and brain tissue oxygenation after subarachnoid hemorrhage." *Critical Care Medicine*, vol. 35, no. 8, pp. 1844–1852, 2007.

[102] K. Brady, J. Lee, K. Kibler, R. Easley, R. Koehler, M. Czosnyka, P. Smielewski, and D. Shaffner, "The lower limit of cerebral blood flow autoregulation is increased with elevated intracranial pressure." *Anesthesia and Analgesia*, vol. 108, pp. 1278–1283, 2009.

[103] S. Klein, V. Sloovere, G. Meyfroidt, and B. Depreitere, "Autoregulation assessment by direct visualization of pial arterial blood flow in the piglet brain." *Scientific Reports*, vol. 9, no. 1, p. 13333, 2019.

[104] G. Kaiser and N. Frühauf, "Method of intracranial pressure monitoring and cerebrospinal fluid sampling in swine." *Laboratory Animals*, vol. 41, pp. 80–85, 2007.

[105] N. Lind, A. Moustgaard, J. Jelsing, G. Vajta, P. Cumming, and A. Hansen, "The use of pigs in neuroscience: Modeling brain disorders." *Neuroscience and Biobehavioral Reviews*, vol. 31, pp. 728–751, 2007.

[106] K. Aquilina, C. Hobbs, S. Cherian, A. Tucker, H. Porter, A. Whitelaw, and M. Thoresen, "A neonatal piglet model of intraventricular hemorrhage and posthemorrhagic ventricular dilation." *Journal of Neurosurgery: Pediatrics*, vol. 197, pp. 126–136, 2007.

[107] P. Sauleau, E. Lapouble, D. Val-Laillet, and C. Malbert, "The pig model in brain imaging and neurosurgery." *Animal*, vol. 3, no. 8, pp. 1138–1151, 2009.

[108] A. Ruesch, D. Acharya, S. Schmitt, J. Yang, M. Smith, and J. Kainerstorfer, "Comparison of static and dynamic cerebral autoregulation under anesthesia influence in a controlled animal model." *PLOS One*, vol. 16, p. e0245291, 2021.

[109] N. Lundberg, H. Troupp, and H. Lorin, "Continuous recording of the ventricular-fluid pressure in patients with severe acute traumatic brain injury: A preliminary report." *Journal of Neurosurgery*, vol. 22, pp. 581–590, 1965.

[110] G. Pinton, J. Aubry, E. Bossy, M. Muller, M. Pernot, and M. Tanter, "Attenuation, scattering, and absorption of ultrasound in the skull bone." *Medical Physics*, vol. 39, pp. 299–307, 2012.

[111] M. Hayashi, Y. Handa, H. Kobayashi, H. Kawano, H. Ishii, and S. Hirose, "Plateau-wave phenomenon 1: Correlation between the appearance of plateau waves and CSF circulation in patients with intracranial hypertension." *Brain*, vol. 114, pp. 2681–2691, 1991.

[112] C. Dias, I. Maia, A. Cerejo, G. Varsos, P. Smielewski, J. Paiva, and M. Czosnyka, "Pressures, flow and brain oxygenation during plateau waves of intracranial pressure." *Neurocritical Care*, vol. 21, no. 1, pp. 124–132, 2014.

[113] C. Robba, S. Pozzebon, B. Moro, J. Vincent, J. Creteur, and F. Taccone, "Multimodal non-invasive assessment of intracranial hypertension: An observational study." *Critical Care*, vol. 24, p. 379, 2020.

[114] M. Andersen, C. Pedersen, and F. Poulsen, "A new novel method for assessing intracranial pressure using noninvasive fundus images: A pilot study." *Scientific Reports*, vol. 10, p. 13062, 2020.

[115] S. Pietrangelo, H. Lee, and C. Sodini, "A wearable transcranial Doppler ultrasound phased array system." *Acta Neurochirurgica Supplement*, vol. 126, pp. 111–114, 2018.

[116] S. Li, W. Shi, S. Pinter, J. Rubin, O. Kripfgans, J. Fowlkes, R. Leichner, J. Jago, and S. Sethuraman, "Towards an operator indpendent blood flow volume quantification using 3D ultrasound." *IEEE International Ultrasonics Symposium*, pp. 1–4, 2020.

[117] M. Schafer, J. Alleman, A. Alexandrov, and K. Barlinn, "Development of an operator independent ultrasound therapeutic device for stroke treatment." *IEEE International Ultrasonics Symposium*, pp. 1978–1951, 2012.

[118] S. Imaduddin and T. Heldt, "Model-based estimation of radial artery blood pressure from recordings of the nexfin monitor." *Proceedings of the 39th Annual Conference of the IEEE Engineering in Medicine and Biology Society*, pp. 1692–1695, 2017.

[119] J. Fortin, D. Rogger, C. Fellner, D. Flotzinger, J. Grond, K. Lerche, and B. Saugel, "A novel art of continuous noninvasive blood pressure measurement." *Nature Communications*, vol. 12, p. 1387, 2021.

[120] A. Meidert and B. Saugel, "Techniques for noninvasive monitoring of arterial blood pressure." *Frontiers in Medicine (Lausanne)*, vol. 4, p. 231, 2017.

[121] J. Seo, S. Pietrangelo, H. Lee, and C. Sodini, “Noninvasive arterial blood pressure waveform monitoring using two-element ultrasound system.” *IEEE Transactions on Ultrasonics, Ferroelectrics, and Frequency Control*, vol. 62, pp. 776–784, 2015.

[122] A. Zakrzewski and B. Anthony, “Noninvasive blood pressure estimation using ultrasound and simple finite element models.” *IEEE Transactions on Biomedical Engineering*, vol. 65, pp. 2011–2022, 2018.

[123] B. Beulen, N. Bijnens, G. Koutsouridis, P. Brands, M. Rutten, and F. van de Vosse, “Towards noninvasive blood pressure assessment in arteries by using ultrasound.” *Ultrasound in medicine and Biology*, vol. 37, pp. 788–797, 2011.

[124] J. Seo, S. Pietrangelo, H. Lee, and C. Sodini, “Carotid arterial blood pressure waveform monitoring using a portable ultrasound system.” *Proceedings of the Annual Conference of the Engineering in Medicine and Biology Society*, vol. 2015, pp. 5692–5695, 2015.

[125] T. Howells, A. Lewén, M. Sköld, E. Ronner-Engström, and P. Enblad, “An evaluation of three measures of intracranial compliance in traumatic brain injury patients.” *Intensive Care Medicine*, vol. 38, pp. 1061–1068, 2012.

[126] E. Lang, K. Paulat, C. Witte, J. Zolondz, and H. Mehdorn, “Noninvasive intracranial compliance monitoring. Technical note and clinical results.” *Journal of Neurosurgery*, vol. 98, pp. 214–218, 2003.

[127] K. Thomas, N. Lewis, B. Hill, and P. Ainslie, “Technical recommendations for the use of carotid duplex ultrasound for the assessment of extracranial blood flow.” *American Journal of Physiology – Regulatory, Integrative and Comparative Physiology*, vol. 309, pp. 707–720, 2015.

[128] M. Wilson, M. Edsell, I. Davagnanam, S. Hirani, D. Martin, D. Levett, J. Thornton, X. Golay, L. Strycharczuk, S. Newman, H. Montgomery, M. Grocott, and C. Imray, “Cerebral artery dilatation maintains cerebral oxygenation at extreme altitude and in acute hypoxia – an ultrasound and MRI study.” *Journal of Cerebral Blood Flow and Metabolism*, vol. 31, pp. 2019–2029, 2011.

[129] J. Park and S. Lee, “Ultrasound deep learning for wall segmentation and near-wall blood flow measurement.” *IEEE Transactions on Ultrasonics, Ferroelectrics and Frequency Control*, vol. 10, pp. 2022–2032, 2020.